

**EFFICACY OF MACHINE LEARNING, EARTH OBSERVATION AND
GEOMORPHOMETRY FOR MAPPING SALT-AFFECTED SOILS IN
IRRIGATED FIELDS**

DIVAN VERMEULEN

Thesis presented in partial fulfilment of the requirements for the degree of Master of Science in the Faculty of Science at Stellenbosch University.



UNIVERSITEIT
iYUNIVESITHI
STELLENBOSCH
UNIVERSITY

100
1918 · 2018

Supervisor: Prof A Van Niekerk

December 2018

DECLARATION

By submitting this report electronically, I declare that the entirety of the work contained therein is my own, original work, that I am the sole author thereof (save to the extent explicitly otherwise stated), that reproduction and publication thereof by Stellenbosch University will not infringe any third party rights and that I have not previously in its entirety or in part submitted it for obtaining any qualification.

Date:

SUMMARY

There is a need to monitor salt accumulation throughout agricultural irrigation schemes as it can have a major negative impact on crop yields and subsequently result in a lower food production. Salt accumulation can result from natural processes, human interference or prolonged waterlogging. Most irrigation schemes are large and therefore difficult to monitor via conventional methods (e.g. regular field visits). More cost-effective, less time-consuming approaches in identifying salt-affected and salt-prone areas in large irrigation schemes are therefore needed. Remote sensing has been proposed as an alternative approach due to its ability to cover a large region on a timely basis. The approach is also more cost-effective because less field visits are required.

A literature review on salt accumulation and remote sensing identified several direct and indirect methods for identifying salt-affected or salt-prone areas. Direct methods focus on the delineation of salt crusts visible on the bare soil in multispectral satellite imagery, whereas indirect methods, which include vegetation stress monitoring and geomorphometry (terrain analysis), attempt to take subsurface conditions into account. A disadvantage of the direct approach is that it does not take subsurface conditions into account, while vegetation stress monitoring (an indirect method) can produce inaccurate results because the vegetation stress can be a result of other factors (e.g. poor farming practices). Geomorphometry offers an alternative (modelling) approach that can either replace or augment direct and other indirect methods.

Two experiments were carried out in this study, both of which focussed on machine learning (ML) algorithms (namely k -nearest neighbour (k NN), support vector machine (SVM), decision tree (DT) and random forest (RF)) and statistical analyses (regression or geostatistics) to identify salt-affected soils. The first experiment made use of very high resolution WorldView-2 (WV2) imagery. A number of texture measures and salinity indices were derived from the WV2 bands and considered as predictor variables. In addition to the ML and statistical analyses, a classification and regression tree (CART) model and Jeffries-Matusita (JM) distance thresholds were also produced from the predictors. The CART model was the most accurate in differentiating salt-affected and unaffected soils, but the accuracy of k NN and RF classifications were only marginally lower. The normalized difference salinity index showed the most promise among the predictors as it featured in the best JM, regression and CART models.

The second experiment applied geomorphometry approaches to two South African irrigation schemes. Elevation sources include the Shuttle Radar Topographic Mission (SRTM) digital elevation model (DEM) and a digital surface model (DSM) produced from stereoscopic aerial

photography. A number of morphological (e.g. slope gradient) and hydrological (e.g. flow direction) terrain parameters were derived from the SRTM DEM and the DSM and used as predictors. In addition to the algorithms used for the first experiment, the geostatistical method Kriging with external drift (KED) was also evaluated in this experiment. The source of elevation had an insignificant impact on the accuracies, although the DSM did show promise when combined with ML. KED outperformed regression modelling and ML in most cases, but ML produced similar results for one of the study areas.

The experiments showed that direct and geomorphometry approaches hold much potential for mapping salt-affected soil. ML also proved to be a viable option for identifying salt-affected or salt-prone soil. It is recommended that a combination of direct and indirect (e.g. vegetation stress monitoring) approaches are considered in future research. Making use of alternative data sources such as hyperspectral imagery or higher spatial resolution DEMs may also prove useful. Clearly, more research is needed before such approaches can be operationalized for detecting, monitoring and mapping salt accumulation in irrigated areas.

KEY WORDS

salinity, salt accumulation, remote sensing, earth observation, geomorphometry, terrain analysis, multispectral imagery, digital elevation model, machine learning, geostatistics

OPSOMMING

Daar is 'n behoefte om soutophoping deur middel van landboubesproeiingskemas te monitor aangesien dit 'n beduidende negatiewe uitwerking op oesopbrengste kan hê en gevolglik tot laer voedselproduksie kan lei. Soutophoping kan voortspruit uit natuurlike prosesse, menslike inmenging of langdurige deurdrenking. Die meeste besproeiingskemas is groot en daarom moeilik om te monitor via konvensionele metodes (bv. gereelde veldbesoeke). Meer koste-effektiewe, minder tydrawende benaderings is dus nodig om soutgeaffekteerde areas en areas wat geneig is tot soutophoping in groot besproeiingskemas te identifiseer. Afstandswaarneming is voorgestel as 'n alternatiewe benadering weens sy vermoë om 'n groot streek op 'n tydige basis te dek. Die benadering is ook meer koste-effektief omdat minder veldbesoeke vereis word.

'n Literatuuroorsig oor soutophoping en afstandswaarneming het verskeie direkte en indirekte metodes geïdentifiseer om soutgeaffekteerde areas of areas geneig tot soutophoping te identifiseer. Direkte metodes fokus op die afbakening van soutkorste wat in multispektrale satellietbeelde op die kaal grond sigbaar is. Indirekte metodes, insluitende plantstresmonitering en geomorfometrie (terreinanalise), aan die ander kant, poog om die ondergrondse toestande in ag te neem. 'n Nadeel van die direkte benadering is dat dit nie ondergrondse toestande in ag neem nie, terwyl plantstresmonitering ('n indirekte metode) onakkurate resultate kan veroorsaak, aangesien die plantstres die gevolg kan wees van ander faktore (bv. swak boerderypraktyke). Geomorfometrie bied 'n alternatiewe (modellering) benadering wat direkte of ander indirekte metodes kan vervang of uitbrei.

In hierdie studie is twee eksperimente uitgevoer. Albei het gefokus op masjienleer (ML) algoritmes, naamlik *k*-nearest neighbour (*k*NN), ondersteunende vektormasjien, besluitboom en ewekansige woud (EW), en statistiese ontledings (regressie of geostatistiek) om soutgeaffekteerde gronde te identifiseer. Die eerste eksperiment het gebruik gemaak van baie hoë resolusie WorldView-2 (WV2) beelde. 'n Aantal tekstuurmaatreëls en soutindekse is afgelei van die WV2-bande en is beskou as voorspeller-veranderlikes. Benewens die ML en statistiese ontledings, is 'n klassifikasie- en regressieboom (KARB) model en Jeffries-Matusita (JM) afstandsdrempels ook van die voorspellers vervaardig. Die KARB-model het die mees akkuraatste differensiasie tussen sout-geaffekteerde en ongeaffekteerde grond gemaak, maar die akkuraatheid van *k*NN- en EW-klassifikasies was slegs marginaal laer. Van al die voorspellers het die genormaliseerde-verskil-saliniteit-indeks die meeste belofte getoon aangesien dit in die beste JM-, regressie- en KARB-modelle presteer het.

Die tweede eksperiment het geomorfometriese benaderings toegepas op twee Suid-Afrikaanse besproeiingskemas. Elevasiebronne sluit in die Shuttle Radar Topographic Mission (SRTM) digitale elevasie-model (DEM) en 'n digitale oppervlakmodel (DOM) wat uit stereoskopiese lugfotografie vervaardig word. 'n Aantal morfologiese (bv. hellingsgradiënt) en hidrologiese (bv. vloeiërigting) terreinparameters is afgelei van die SRTM DEM en die DOM en is gebruik as voorspellers. Benewens die algoritmes wat vir die eerste eksperiment gebruik is, is die geostatistiese metode Kriging met eksterne dryf (KED) ook in hierdie eksperiment geëvalueer. Die bron van elevasie het 'n onbeduidende impak op die akkuraatheid gehad, hoewel die DOM belofte getoon het wanneer dit met ML gekombineer is. KED het in meeste gevalle beter presteer as regressie modellering en ML, maar ML het soortgelyke resultate vir een van die studiegebiede opgelewer.

Die eksperimente het getoon dat direkte en geomorfometriese benaderings baie potensiaal het vir die kartering van soutgeaffekteerde grond. ML het ook bewys dat dit 'n lewensvatbare opsie is om soutgeaffekteerde grond of grond wat geneig is tot soutophoping, te identifiseer. Daar word aanbeveel dat 'n kombinasie van direkte en indirekte (bv. plantegroei-stresmonitering) benaderings in toekomstige navorsing oorweeg word. Die gebruik van alternatiewe databronne soos hiperspektrale beelde of hoër ruimtelike resolusie-DOM's kan ook nuttig wees. Dit is duidelik dat meer navorsing nodig is voordat sulke benaderings geoperasionaliseer kan word vir die opsporing, monitering en kartering van soutophoping in besproeide gebiede.

SLEUTELWOORDE

soutinhoud, soutophoping, afstandwaarneming, aardwaarneming, geomorfometrie, terreinanalise, multispektrale beelde, digitale elevasiemodel, masjienleer, geostatistiek

ACKNOWLEDGEMENTS

I sincerely thank:

- Prof Adriaan van Niekerk for his guidance, excellent suggestions and helpful advice;
- The staff of the Department of Geography and Environmental Studies for helpful comments and constructive criticism during scheduled feedback sessions;
- Helene van Niekerk of Linguafix (www.linguafix.net) for editing my thesis.

This work forms part of a larger project titled “Methodology to monitor the status of waterlogging and salt-affected soils on selected irrigation schemes in South Africa”, which was initiated and funded by the Water Research Commission (WRC) of South Africa (contract number K5/1880//4). More information about this project is available in published report TT 648/15 (ISBN 978-1-4312-0739-8). I also acknowledge and thank the project leader, Dr Piet Nell of the Agricultural Research Council, for providing the soil data used in this study and for his invaluable guidance and insight, particularly during the field surveys.

CONTENTS

| | |
|---|-------------|
| DECLARATION | II |
| SUMMARY | III |
| OPSOMMING | V |
| ACKNOWLEDGEMENTS..... | VII |
| CONTENTS..... | VIII |
| TABLES | XI |
| FIGURES | XII |
| ACRONYMS AND ABBREVIATIONS..... | XIV |
| CHAPTER 1: INTRODUCTION | 1 |
| 1.1 SALINIZATION | 1 |
| 1.1.1 Saline soil..... | 2 |
| 1.1.2 Waterlogging..... | 2 |
| 1.1.3 Types of salinization..... | 3 |
| 1.1.4 Effects of salinization | 3 |
| 1.2 REMOTE SENSING AND SALINIZATION | 3 |
| 1.3 MACHINE LEARNING..... | 5 |
| 1.4 PROBLEM FORMULATION..... | 6 |
| 1.5 RESEARCH AIM AND OBJECTIVES | 6 |
| 1.6 RESEARCH METHODOLOGY AND AGENDA..... | 7 |
| CHAPTER 2: EARTH OBSERVATION..... | 10 |
| 2.1 REMOTE SENSING (RS)..... | 10 |
| 2.1.1 Surface reflectance properties..... | 12 |
| 2.1.2 Pre-processing of imagery | 13 |
| 2.1.3 Image classification | 15 |
| 2.2 GEOMORPHOMETRY..... | 20 |
| 2.2.1 Digital elevation models | 20 |
| 2.2.2 Digital terrain modelling | 21 |
| 2.2.3 Terrain derivatives..... | 22 |
| 2.3 GEOSPATIAL TECHNIQUES FOR DETECTING AND MODELLING SALT ACCUMULATION..... | 25 |
| 2.3.1 Spectral analysis (direct approach) | 25 |

| | | |
|--|---|-----------|
| 2.3.2 | Vegetation stress monitoring (indirect approach)..... | 28 |
| 2.3.3 | Spatial indices (texture measures) | 30 |
| 2.3.4 | Separability analysis | 30 |
| 2.3.5 | Regression analysis..... | 31 |
| 2.3.6 | Principal component analysis..... | 31 |
| 2.3.7 | Geostatistics | 32 |
| 2.4 | LITERATURE SUMMARY | 33 |
| CHAPTER 3: AN EVALUATION OF MULTISPECTRAL VHR | | |
| IMAGERY FOR SOIL SALINITY MONITORING* | | |
| | | 35 |
| 3.1 | ABSTRACT | 35 |
| 3.2 | INTRODUCTION..... | 35 |
| 3.3 | METHODS | 38 |
| 3.3.1 | Study area | 38 |
| 3.3.2 | Data collection and preparation..... | 40 |
| 3.4 | RESULTS..... | 45 |
| 3.4.1 | Spectral profiles and separability analysis results | 46 |
| 3.4.2 | Regression modelling and DT analysis..... | 47 |
| 3.4.3 | Classification accuracy results | 48 |
| 3.5 | DISCUSSION | 50 |
| 3.6 | CONCLUSIONS..... | 51 |
| CHAPTER 4: MACHINE LEARNING PERFORMANCE FOR | | |
| PREDICTING SOIL SALINITY USING DIFFERENT COMBINATIONS | | |
| OF GEOMORPHOMETRIC COVARIATES* | | |
| | | 53 |
| 4.1 | ABSTRACT | 53 |
| 4.2 | INTRODUCTION..... | 54 |
| 4.3 | MATERIALS AND METHODS..... | 57 |
| 4.3.1 | Study areas..... | 57 |
| 4.3.2 | Data collection and preparation..... | 60 |
| 4.3.3 | Analyses..... | 62 |
| 4.3.4 | Accuracy assessment..... | 64 |
| 4.4 | RESULTS..... | 65 |
| 4.4.1 | Regression modelling | 66 |
| 4.4.2 | Geostatistics | 67 |
| 4.4.3 | Machine learning..... | 68 |

| | | |
|---|---|-----------|
| 4.4.4 | Classified maps | 68 |
| 4.5 | DISCUSSION | 70 |
| 4.6 | CONCLUSION..... | 72 |
| CHAPTER 5: DISCUSSION AND CONCLUSIONS..... | | 74 |
| 5.1 | REFLECTION ON RESEARCH OBJECTIVES..... | 74 |
| 5.2 | FINDINGS OF DIRECT AND GEOMORPHOMETRY APPROACHES IN MAPPING SALINE SOILS | 76 |
| 5.2.1 | ML using VHR multispectral imagery..... | 76 |
| 5.2.2 | Geomorphometry | 77 |
| 5.3 | SUGGESTIONS FOR FUTURE RESEARCH..... | 78 |
| 5.4 | CONCLUSION..... | 79 |
| REFERENCES | | 80 |

TABLES

| | |
|---|----|
| Table 3.1: Summary on sample site EC measurements and field notes..... | 41 |
| Table 3.2: Considered features for analysis | 42 |
| Table 3.3: Results of regression analyses used to determine the relationship between EC and WorldView-2 features | 47 |
| Table 3.4: Summary of salt-affected and unaffected classification accuracies..... | 48 |
| Table 4.1: DEM derivatives included in each feature set | 61 |
| Table 4.2: Statistical profiles of the training and reference samples for each study area | 65 |
| Table 4.3: Three top-performing regression models, KED models and ML classifiers for the study areas | 66 |

FIGURES

| | |
|---|----|
| Figure 1.1: Research design for evaluating the potential of VHR WV2 imagery and elevation datasets for mapping salt accumulation within irrigation schemes | 8 |
| Figure 2.1: Section of the electromagnetic spectrum most commonly used for remote sensing purposes | 11 |
| Figure 2.2: Difference between digital terrain models (DTM) and digital surface models (DSM) | 21 |
| Figure 3.1: Location of the study area in South Africa (a) with the extent of the Vaalharts irrigation scheme (b) and the WorldView-2 image (c), as well as the distribution of sample points in the six collection sites (d1 to d6)..... | 39 |
| Figure 3.2: EC values of the collected soil samples, showing that there was a good balance between salt-affected and unaffected soil samples..... | 45 |
| Figure 3.3: Examples of salt-affected soils in the study area. Clear evidence of salt precipitation is visible in (a), with less precipitation visible in (b). In (c) no salt precipitation is visible, but indications of waterlogging are observed..... | 46 |
| Figure 3.4: Spectral profile of salt-affected and unaffected samples as extracted from the WorldView-2 image | 46 |
| Figure 3.5: Relationship between NDSI (red and NIR ₁) and measured soil EC. Two outliers (A and B) were identified and removed. | 48 |
| Figure 3.6: Produced maps from the ruleset-based and supervised classifications, namely (a) NDSI (red and NIR ₁) SEaTH threshold, (b) NDSI (yellow and NIR ₁) cubic regression model, (c) NDSI (yellow and NIR ₁) CART threshold, (d) kNN ($k = 3$), (e) DT, (f) RF, (g) SVM and (h) MaxL | 49 |
| Figure 4.1: Location of the Vaalharts study area. Also shown is the extent of the Vaalharts irrigation scheme and the distribution of the soil samples obtained during the field surveys..... | 58 |
| Figure 4.2: Location of the Breede River study area. Also shown is the extent of the Breede River irrigation scheme and the distribution of the soil samples obtained during the field surveys. | 59 |
| Figure 4.3: EC values of soil samples collected in the study areas..... | 65 |
| Figure 4.4: Scatterplot of Vaalharts SRTM DEM cubic regression model derived from slope height | 67 |

- Figure 4.5: Scatterplots of (a) Vaalharts KED model produced from cross-sectional curvature, aspect and standardized height and (b) Breede River SRTM DEM KED model derived from normalized height 68
- Figure 4.6: Maps produced from the (a) DSM KED model derived from CSC, aspect and standardized height, (b) SRTM DEM KED model derived from TST, (c) DSM KED model derived from CSC and aspect, and (d) quadratic regression model produced from SH for Vaalharts 69
- Figure 4.7: Maps produced from the (a) SRTM DEM KED model derived from normalized height, (b) SRTM DEM KED model derived from DDG, (c) DSM KED model derived from TRI and VD, and (d) DSM-based DT classifier for Breede River 70

ACRONYMS AND ABBREVIATIONS

| | |
|---------|--|
| ASTER | Advanced spaceborne thermal emission and reflection radiometer |
| AUROC | Area under receiver operating characteristic |
| CNBL | Channel network base level |
| CD: NGI | Chief Directorate: National Geospatial Information |
| CART | Classification and regression trees |
| CB | Coastal blue |
| CV | Coefficient of variance |
| CK | Co-kriging |
| COSRI | Combined spectral response index |
| CSC | Cross-sectional curvature |
| DT | Decision tree |
| D8 | Deterministic eight-node |
| DEM | Digital elevation model |
| DN | Digital number |
| DSM | Digital surface model |
| DTM | Digital terrain model |
| DDG | Downslope distance gradient |
| EO | Earth observation |
| EC | Electrical conductivity |
| EMR | Electromagnetic radiation |
| FLAASH | Fast line-of-sight atmospheric analysis of spectral hypercubes |
| GLAS | Geoscience laser altimeter system |
| GPS | Global positioning system |
| GLCM | Grey level co-occurrence matrices |
| GCP | Ground control point |
| HAND | Height above nearest drainage |
| IR | Infrared |
| IFOV | Instantaneous field of view |
| JM | Jeffries-Matusita |
| kNN | <i>k</i> -nearest neighbour |
| KED | Kriging with external drift |

| | |
|-----------|--|
| LiDAR | Light detection and ranging |
| LS-factor | Slope length and steepness factor |
| ML | Machine learning |
| MaxL | Maximum likelihood |
| MIR | Mid-infrared |
| MSP | Mid-slope position |
| NN | Nearest neighbour |
| NIR | Near-infrared |
| NDSI | Normalized difference salinity index |
| NDVI | Normalized difference vegetation index |
| NH | Normalized height |
| OK | Ordinary kriging |
| OA | Overall accuracy |
| PLS | Partial least square |
| PCA | Principal component analysis |
| PC1 | First principal component |
| PA | Producer accuracy |
| RBF | Radial basis function |
| RADAR | Radio detection and ranging |
| RF | Random forest |
| RE | Red edge |
| RK | Regression-kriging |
| RM | Regression modelling |
| RSP | Relative slope position |
| RS | Remote sensing |
| RMSE | Root mean square error |
| SWI | SAGA wetness index |
| SI | Salinity index |
| SEaTH | Separability and thresholds |
| SH | Slope height |
| SWIR | Short-wave infrared |
| SRTM | Shuttle radar topographic mission |
| SLAR | Side-looking airborne radar |
| SLR | Side-looking radar |
| SRI | Simple ratio index |

| | |
|-------|---|
| SLFA | Slope limited flow accumulation |
| STDH | Standardized height |
| SUDEM | Stellenbosch University digital elevation model |
| SAVI | Soil-adjusted vegetation index |
| SVM | Support vector machine |
| SAR | Synthetic aperture radar |
| InSAR | Synthetic aperture radar interferometry |
| SAGA | System for automated geoscientific analyses |
| TST | Terrain surface texture |
| TIR | Thermal infrared |
| TPI | Topographic position index |
| TWI | Topographic wetness index |
| TIN | Triangulated irregular network |
| UK | Universal kriging |
| UA | User accuracy |
| VI | Vegetation index |
| VDTCN | Vertical distance to channel network |
| VHR | Very high resolution |
| WV2 | WorldView-2 |

CHAPTER 1: INTRODUCTION

Salt accumulation or salinization, the process whereby soluble salts accumulate in soil (Al-Khaier 2003), is of major concern throughout the world due to its negative impact on agricultural areas and crop yields (Metternicht & Zinck 2003). It can result from natural processes or through human interference such as vegetation clearing, landscape reshaping, earth works and irrigation (Mcghie 2005) and can cause lower property values, engineering difficulties, increased soil erosion, damage to infrastructure and eutrophication of rivers (Metternicht & Zinck 2003). Salinization can also be a consequence of prolonged waterlogging (Dwivedi 1997). According to Dwivedi, Sreenivas and Ramana (1999), soils are said to be waterlogged when the water table rises to an extent that the pores in the root zone of a crop become saturated. The result is a reduction in normal air flow, lower levels of oxygen and increased levels of carbon dioxide in the soil. Poor drainage factors can produce waterlogged soil, such as the natural accumulation of water at footslopes and valley bottoms, regions close to or adjacent to large open water surfaces, poor surface water management, water leaking from dams, pipes, canals or irrigation mainlines close to man-made obstructions (e.g. bridges) and over-irrigation (Dwivedi 1997).

Ghassemi, Jakeman and Nix (1995) state that about 77 million hectares (ha) of the global land surface is affected by extremely saline soil caused by human activity, of which 58% occurs in irrigated areas. According to Metternicht and Zinck (2003), 20% of global irrigated land is affected by salt accumulation. It has been estimated that 18% of South Africa's irrigated soils are either affected by salt accumulation or waterlogging (Backeberg et al. 1996). Due to low rainfall, and therefore less leaching of salts from the soil, salt accumulation is more extensive in arid areas than humid areas (Metternicht & Zinck 2008). As a result of increased population pressure, more arid areas will be used for irrigated agricultural production in the future, increasing the severity of salinization. Given that only 13.7% of South African land is suitable for agricultural use (Department of Agriculture, Forestry and Fisheries 2013), measures are urgently needed to prevent the loss of fertile agricultural land.

1.1 SALINIZATION

Soil salinization is a well-known land degradation process that can have a negative impact on the size and productivity of agricultural land, especially in semi-arid and arid regions (Elnaggar & Noller 2010). Defined as the accumulation of soluble salts (e.g. chlorides, sulphates and carbonates of sodium, magnesium or calcium) in the ground water, subsoil or on the soil surface (Mashimbye 2005), salinization can result naturally (primary salinization) or from human activity (secondary salinization) (Al-Khaier 2003). Primary salinization, caused by the leaching of salts from the soil,

is controlled by geological, geomorphic, climatic and hydrological factors (Ghassemi, Jakeman & Nix 1995). When primary minerals in crystalline rocks are eroded, salts are redistributed to form part of sedimentary rocks and sedimentary deposits at the earth's surface. Weathering of the salt-rich sediments and hard rocks therefore allows salts to enter the soil system (Metternicht & Zinck 2008). Primary salinization is usually found at topographic depressions, footslopes, or where groundwater is naturally shallow (e.g. at or close to springs) (Ghassemi, Jakeman & Nix 1995). Secondary salinization, a result of human activity, affects the way in which salts move and accumulate in soils (Stals 2007). In irrigated areas, salinization can be a result of a rising groundwater table due to irrigation; saline water use for irrigation; saline seeps in close proximity to water reservoirs, ponds and canals; and the intrusion of saline water into depleted freshwater aquifers. Increased salinity in rainfed fields are mostly the result of increases or decreases in evapotranspiration, or result from saline seeps from below the surface, such as at shallow water bodies and dry lakes (Metternicht & Zinck 2003; Metternicht & Zinck 2008).

1.1.1 Saline soil

There is no universally accepted definition for saline soil because the definition depends on the discipline and the type of measurement (Fitzpatrick 2002). For example, hydrogeologists distinguish between primary and secondary salt accumulation, whereas a range of electrical conductivity (EC) levels (slightly, moderate and severely) is used by plant and soil scientists. According to Nell et al. (2015), soil scientists in South Africa distinguishes between salt-affected and unaffected soils by making use of a EC threshold of 400 mS/m. Soils consisting of EC measurements equal to or greater than 400 mS/m are regarded as being salt-affected. Other scientific fields may make use of a combination of a low pH (< 3.5), the presence of sulphur, and high EC values to distinguish acid sulphate salinity. Salinity can also simply be referred to as soils containing high amounts of soluble salts (Fitzpatrick 2002; Al-Khaier 2003; Nell et al. 2015).

1.1.2 Waterlogging

Salt accumulation can also be a consequence of prolonged waterlogging. Waterlogging is caused by poor drainage and occurs when a rise in the water table saturates the soil pores in the root zone of the crop, resulting in a restriction of air circulation, lower oxygen levels and higher levels of carbon dioxide (Dwivedi, Sreenivas & Ramana 1999; Mcghie 2005). Prolonged waterlogging results in secondary salinization, a process whereby the soil root zone is enriched by soluble salts (e.g. sodium chloride and sodium sulphate) (Dwivedi 1997). Ponding, a severe form of waterlogging, occurs when the water table rises above the soil surface (Nell et al. 2015). Well-known causes of waterlogging include over-irrigation (e.g. canal irrigation in agricultural areas),

large open water surfaces, natural accumulation of water (e.g. at foot slopes and valleys), leaking water and man-made objects' proximity (e.g. bridges, canals, dams and pipes) (Rao et al. 1998; Dwivedi 1997; Dwivedi, Sreenivas & Ramana 1999).

1.1.3 Types of salinization

Salt types found in soil include carbonates, sulphates and chlorides. The more saline a soil, the higher the occurrence of more soluble salts. Unaffected or slightly saline soils are usually dominated by Ca^{2+} , Mg^{2+} and HCO_3^- , whereas highly affected soils are often dominated by chemicals such as NaCl and Na_2SO_4 . Soils affected by alkaline soil-forming processes mostly consist of sodium salts (e.g. Na_2CO_3 and NaHCO_3) (Metternicht & Zinck 2008). According to Metternicht and Zinck (2008) sodium chloride (NaCl), which is also highly soluble and toxic, is the most common salt found in saline soil.

1.1.4 Effects of salinization

Even though salinization affects smaller areas compared to other land degradation processes, it is still a severe environmental hazard that is of great concern. High soil salinity conditions result in a reduction in the uptake of water by plants (due to reduced osmotic pressure), which in turn has a negative impact on plant growth and agricultural crop yield (Mashimbye 2005; Barnard et al. 2012; Nell et al. 2015). Droughts have a similar effect on plants (Metternicht & Zinck 2008).

High soil salinity also has several secondary negative impacts on regions. This includes lower property values (due to degraded land on farms), engineering problems, increased soil erosion, eutrophication of rivers and infrastructure damage (Metternicht & Zinck 2003).

1.2 REMOTE SENSING AND SALINIZATION

The spectral properties of salt-affected soils have been investigated by several authors (Rao et al. 1995; Abbas & Khan 2007; Metternicht & Zinck 2003; Elnaggar & Noller 2010; Farifteh, Farshad & George 2006; Khan et al. 2005; Iqbal 2011; Setia et al. 2013; Sidike, Zhao & Wen 2014). Rao et al. (1995) showed that salt-affected soils have a higher reflectance in the visible and near-infrared (NIR) regions of the electromagnetic spectrum. This was confirmed by Metternicht and Zinck (2003) and Abbas and Khan (2007). Salt-affected soils with salt encrustations visible on the topsoil have been shown by Elnaggar and Noller (2010) to be smoother than non-saline surfaces. Surface roughness and the colour of saline soils has been found to also have an impact on their spectral properties (Farifteh, Farshad & George 2006). Several salinity indices (SIs), calculated from multispectral image bands, were developed from these findings to effectively discriminate salt-affected soils from unaffected soils. These include the normalized difference salinity index

(NDSI) (Khan et al. 2005) and the combined spectral response index (COSRI) (Fernandez-Buces et al. 2006). Difficulties in discriminating saline soils from non-saline soils can arise from an increase in soil moisture, decreases in reflectance as a result of high clay content, an increase in ferric oxides, and the alteration of soil spectral properties due to irrigation and tillage, especially in highly dynamic irrigation schemes (Metternicht & Zinck 2003). Section 2.3.1 provides a more detailed discussion on SIs. More information can also be found in Fernandez-Buces et al. (2006), Abbas and Khan (2007) and Akhtar Abbas et al. (2013). Conventional methods of monitoring salt accumulation involve regular field visits to collect soil samples. This is followed by a laboratory analysis of the collected soil samples. Such an approach is not viable for large irrigation schemes due to the number of field visits required to effectively monitor the region. Remote sensing (RS) has been proposed as a less time-consuming, more cost-effective approach for monitoring salt accumulation in large areas (Abbas et al. 2013). RS approaches make use of electromagnetic radiation to derive information about the Earth's surface from an overhead perspective. The electromagnetic radiation can either be reflected or emitted from the Earth's surface (Campbell 2006).

Techniques to identify salt-affected soils using RS methods can be grouped into two categories, namely direct (soil-related indicators) and indirect (performance-related indicators and geomorphometry) approaches. Direct indicators include dark, greasy soil surfaces, puffy soil, white salt crusts, coarser topsoil and dehydrated cracks, whereas performance-related indicators include moisture stress, the presence of dead trees, spotty growth of crops and a blue-green tinge in vegetation (Farifteh, Farshad & George 2006). The main disadvantage associated with the direct approach is that the method is limited to the topsoil, and therefore does not take subsurface processes into account (Dwivedi 1997; Dwivedi, Sreenivas & Ramana 1999). Geomorphometry, the use of digital elevation data to perform terrain analysis (Pike 2000), is also considered an indirect approach, but is not strictly a RS approach (although elevation data is most commonly derived from RS data).

Performance-related indicators and geomorphometry has been proposed as possible methods to overcome some of the limitations of the direct approach. They take subsurface processes into account and can be categorised as indirect methods for identifying saline soils. Performance-related indicators focus on the identification of plant stress caused by salt accumulation (Muller & Van Niekerk 2016a). However, poor vegetation health, as detected by vegetation monitoring, can also be caused by poor farming practices and soil preparation (Furby et al. 1995). High bare ground reflectance can furthermore have a negative impact on the calculated vegetation indices and reduce their effectiveness (Douaoui, Nicolas & Walter 2006) and weak correlations between vegetation

indices and soil electrical conductivity (EC) have been found as a result of variations in different crop species' salt tolerances (Maas & Hoffman 1977; Aldakheel 2011). Identifying areas susceptible to salt accumulation using geomorphometry techniques has yielded encouraging results (Sulebak, Tallaksen & Erichsen 2000; Elnaggar & Noller 2010; Akramkhanov et al. 2011; Taghizadeh-Mehrjardi et al. 2016). Sulebak et al. (2000) observed a strong, significant correlation between soil moisture and terrain data, namely slope, aspect and profile curvature, while Akramkhanov et al. (2011) found significant correlations between soil EC and several terrain derivatives (distance to drainage, ground water table depth, slope, profile curvature). Both studies employed stepwise regression modelling. Significant correlations between soil EC and elevation, slope and wetness indices have also been observed by Elnaggar and Noller (2010). A more recent study by Taghizadeh-mehrjardi et al. (2016) identified elevation, wetness indices and the multi-resolution valley bottom flatness index to be the most important predictors of soil salinity. By employing a decision tree (DT) to terrain data, both Evans et al. (1996) and Elnaggar and Noller (2010) achieved high accuracies in identifying saline soil. Geostatistical methods applied on terrain derivatives have also shown promise in identifying soils affected by salt accumulation (Eldeiry & Garcia 2008; Eldeiry & Garcia 2009; Gallichand et al. 1992; Juan et al. 2011; Li et al. 2007; Taghizadeh-Mehrjardi et al. 2014; Utset et al. 1998).

1.3 MACHINE LEARNING

Machine learning (ML) algorithms use training samples consisting of a known category to classify cases with an unknown category (Rees 2001; Campbell 2006). Unlike parametric classifiers, which assume that the data are normally distributed, ML classifiers are non-parametric. Non-parametric classifiers do not make assumptions about the data distribution to estimate essential parameters (Jain, Duin & Mao 2000; Hubert-Moy et al. 2001). This is especially advantageous when working with RS data, because in most cases RS data are not normally distributed. Several ML algorithms are available and have become popular for RS use, namely *k*-nearest neighbour (*k*NN) (Franco-Lopez, Ek & Bauer 2001; Ying Li & Bo Cheng 2009; Falkowski et al. 2010), support vector machine (SVM) (Lizarazo 2008; Li et al. 2010; Petropoulos, Kalaitzidis & Prasad Vadrevu 2012), decision tree (DT) (Punia, Joshi & Porwal 2011; Gómez et al. 2012; Hladik & Alber 2014) and random forest (RF) (Gislason, Benediktsson & Sveinsson 2006; Chan & Paelinckx 2008; Rodriguez-Galiano et al. 2012a). ML can easily be automated, allows for combinations of categorical and continuous input variables, and has the ability to capture hierarchical and non-linear relationships (Hladik & Alber 2014). More detailed discussions on ML classifiers are available in Sections 2.1.3.6, 3.3.2.7 and 4.3.3.3.

1.4 PROBLEM FORMULATION

As discussed in Section 1.2, several RS approaches can be used to identify saline soil. Direct approaches have been frequently investigated, but most studies were performed within large cultivated fields affected severely by salt accumulation. The extent of the salt-affected areas were also large enough to employ medium spatial resolution satellite imagery, namely Landsat (30 m) (Lenney et al. 1996; McFarlane, George & Caccetta 2004; Fernandez-Buces et al. 2006; Rodríguez, González & Zaballos 2007; Iqbal & Mehdi 2008; Abdelfattah, Shahid & Othman 2009; Elnaggar & Noller 2010; Aldakheel 2011; Mohamed, Morgun & Goma Bothina 2010; Iqbal 2011; Wang et al. 2013; Taghizadeh-Mehrjardi et al. 2014; Taghizadeh-Mehrjardi et al. 2016), IRS (20 m) (Dwivedi & Sreenivas 1998; Dwivedi et al. 2001; Abbas & Khan 2007; Abbas et al. 2013) or ASTER (15 m) (Gao & Liu 2008). The occurrence of small patches of salt accumulation and the relatively small size of irrigated fields in South Africa (Nell & Van Niekerk 2014), coupled with the elongated shapes of many fields, reduces the effectiveness of medium resolution imagery to detect salt-affected areas. It is likely that high or very high resolution (VHR) imagery will be much more effective in the South African context, but such imagery has not yet been locally evaluated for salt accumulation monitoring. The few international studies that have employed VHR imagery for mapping salt-affected areas (Sidike, Zhao & Wen 2014; Setia et al. 2013; Douaoui & El Ghadiri 2015) did not consider advanced classification techniques such as ML. In addition, no comparison of ML and geostatistical techniques for modelling salt-affected soils – using empirical measurements and terrain derivatives as input – has been attempted to date. These gaps in knowledge open several research opportunities.

The following research questions were set:

1. How effective is VHR multispectral imagery for direct detection of salt accumulation in South African conditions?
2. Which multispectral bands, SIs and other image transformation methods are the most effective for directly identifying salt accumulation?
3. How viable is geomorphometry (indirect) for modelling salt accumulation within agricultural fields?

1.5 RESEARCH AIM AND OBJECTIVES

The aim of this research is to evaluate VHR EO (direct) and geomorphometry (indirect) approaches for identifying salt-affected or salt-prone areas within agricultural fields.

To achieve the research aim, the following objectives have been set:

1. Review the EO and geomorphometry literature, specifically looking at how these approaches can be used to monitor salt accumulation.
2. Identify appropriate study areas in which the various techniques can be evaluated.
3. Collect and acquire empirical data, satellite images and elevation datasets for the selected study areas, and prepare them for analyses.
4. Determine the VHR multispectral bands, SIs and other image transformations most appropriate for identifying salt accumulation.
5. Apply several statistical and ML approaches to the multispectral derivatives to discriminate between salt-affected and unaffected areas.
6. Identify the DEM derivatives that show the most potential for modelling salt-affected areas.
7. Compare the effectiveness of ML and geostatistical approaches applied to DEM derivatives for classifying salt-affected and unaffected soils.
8. Synthesise the results of the experiments to make recommendations on mapping salt accumulation in irrigation schemes.

1.6 RESEARCH METHODOLOGY AND AGENDA

This research consisted of two experiments: one carried out on VHR satellite imagery and the other on elevation datasets. An investigation was launched into the relationship between these datasets and the occurrence of salt accumulation, while the possibility of accurately mapping salt accumulation using quantitative methods was also determined. The first experiment examined VHR satellite imagery, while the second experiment focussed on elevation data and terrain analysis approaches.

Figure 1.1 shows the structure of this thesis and the research design. This chapter, which introduced the aims and objectives of the study, is followed by an overview of earth observation (EO), geomorphometry and EO approaches in mapping salt accumulation (Chapter 2). Literature on ruleset-based approaches and supervised algorithms are also discussed in Chapter 2. Various variables that can be derived from RS data and elevation data are also discussed.

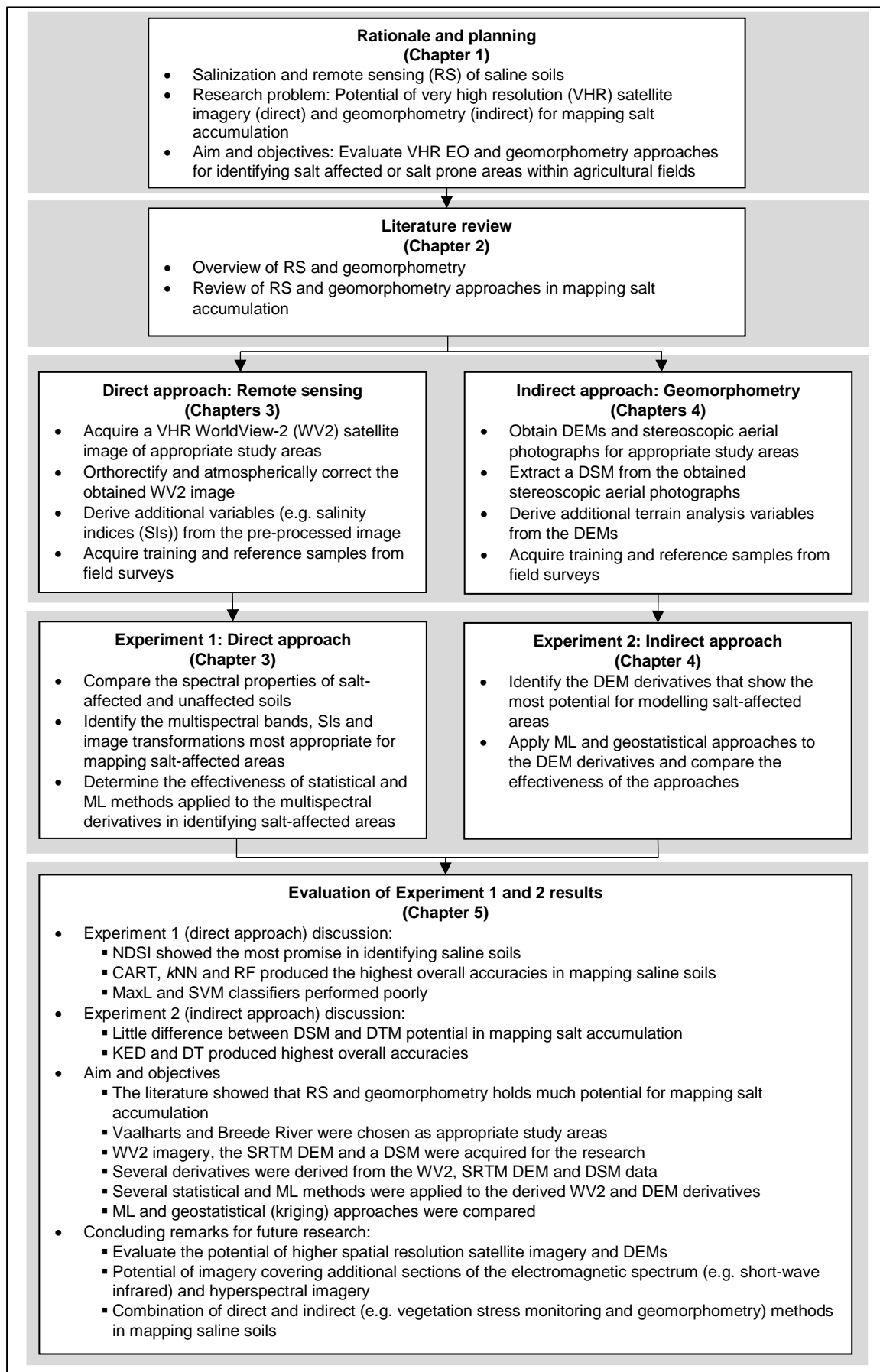


Figure 1.1: Research design for evaluating the potential of VHR WV2 imagery and elevation datasets for mapping salt accumulation within irrigation schemes

Chapter 3 presents the results of the first experiment (evaluation of a VHR multispectral image for soil salinity monitoring in a moderately affected irrigated area), followed by Chapter 4, which is based on the second investigation (efficacy of machine learning and geomorphometry for modelling salt accumulation in irrigated fields). The research done in Chapter 3 and Chapter 4 was prepared for submission to scientific journals and may therefore be duplicated in certain theoretical discussions, figures and tables. Chapter 5 provides a summary of the findings of the direct- and indirect approaches, revisits the aims and objectives, provides suggestions for future research and draws conclusions from the conducted experiments.

CHAPTER 2: EARTH OBSERVATION

This chapter provides an overview of the electromagnetic spectrum (ES), remote sensing (RS) and geomorphometry. The reflectance properties of particular surfaces and the importance of pre-processing and image classification is discussed first, followed by a description of geomorphometry. In terms of the latter, focus is placed on digital elevation models, digital terrain modelling and the terrain derivatives that can be derived from elevation datasets. The chapter concludes with a discussion of geospatial techniques for detecting and modelling salt accumulation. These include spectral analysis of bare soil, vegetation stress monitoring, spatial indices, separability analysis, regression analysis, principal component analysis and geostatistics.

2.1 REMOTE SENSING (RS)

RS is the analysis of electromagnetic radiation (EMR) reflected from objects or phenomena where the observer is not in direct contact with the target (Lillesand, Chipman & Kiefer 2008; Mather & Koch 2011). Many activities can be included in such a broad definition. EO by RS is the interpretation of EMR emitted from objects on the Earth's land, water or ice surfaces by airborne or satellite borne instruments (Mather & Koch 2011). Throughout this thesis, RS will be regarded as such.

EMR reflected from the Earth's surface contains information on the chemical, physical and biological properties of soils, water and vegetation (Chuvieco & Huete 2010). RS sensors capture EMR emitted and reflected from the earth's surface. Many forms of EMR can be measured, namely visible light (blue, green and red), infrared (IR) and microwaves (Lillesand, Chipman & Kiefer 2008). Other forms of EMR can also be captured, such as X-rays or ultraviolet, but these regions of the ES are less useful for RS purposes due to atmospheric scattering and absorption (Mather & Koch 2011). Figure 2.1 shows the extent of the ES utilized for RS purposes. The visible region (0.4 to 0.7 μm) can be subdivided into the three primary colours: blue (0.4 to 0.5 μm), green (0.5 to 0.6 μm) and red (0.6 to 0.7 μm) (Chuvieco & Huete 2010). The blue region is most affected by atmospheric scattering and is therefore used less for RS purposes than the green and red regions (Mather & Koch 2011). IR radiation consists of wavelengths longer than the red portion of the spectrum, extending from 0.7 to 14 μm (Campbell 2006). This region can also be subdivided into three portions, namely NIR (0.7 to 1.2 μm), MIR (1.2 to 8 μm) and thermal infrared (TIR) (8 to 14 μm). NIR is best used in discriminating green vegetation, MIR for soil and vegetation moisture content and TIR for mapping surface temperature (Lillesand, Chipman & Kiefer 2008; Chuvieco & Huete 2010). The longest wavelengths used for RS purposes are in the microwave region (>1 mm) (Campbell 2006). Microwaves can penetrate clouds, rain, snow, smoke (Lillesand, Chipman

& Kiefer 2008; Mather & Koch 2011) and vegetation cover at various depths. This enables surface roughness and soil moisture analysis (Chuvienco & Huete 2010).

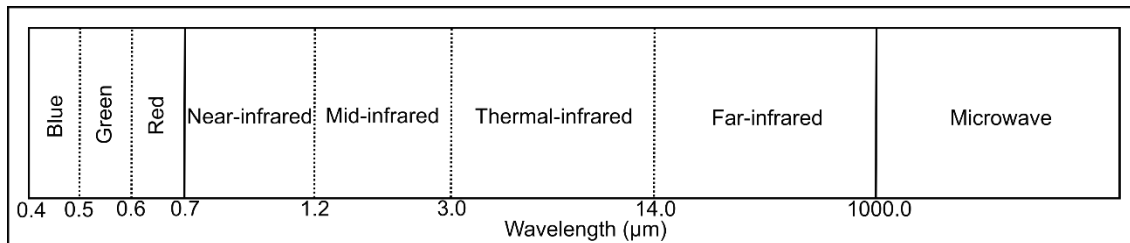


Figure 2.1: Section of the electromagnetic spectrum most commonly used for remote sensing purposes

The reflected radiation is captured by airborne or satellite borne sensors in several bands or regions of the ES. Two types of sensors can be used: passive or active sensors. Passive sensors make use of the sun as their source of energy, whereas active sensors emit their own energy and record the backscatter from the Earth's surface (Harris 1987; Campbell 2006). Active sensors have the advantage of being able to operate at either day or night (Mather & Koch 2011). The data recorded by the sensors are stored in a digital image consisting of a two-dimensional array of pixels, referred to as a raster image (Liu & Mason 2009; Mather & Koch 2011), while the brightness of each pixel is called the digital number (DN). Each raster can also consist of several bands, where each band covers different ranges of the electromagnetic spectrum. This allows the capturing of an object's reflectance at varying wavelengths, better known as the spectral reflectance signature.

Remotely sensed imagery has several important properties, which can be grouped into spatial, spectral, radiometric and temporal resolutions. These properties vary among the available sensors and are therefore important to consider in relation to the problem at hand. Each will be discussed separately.

It is difficult to define spatial resolution (Mather & Koch 2011), but for optic-electronic sensors, the concept of instantaneous field of view (IFOV) is most commonly used. IFOV can be described as the area on the ground captured by a sensor at a particular altitude and time (Chuvienco & Huete 2010; Mather & Koch 2011). Higher spatial resolution will minimize mixed pixels, which is the average radiance of several objects encompassed by the pixel (Lillesand, Chipman & Kiefer 2008).

The spectral resolution of remotely sensed imagery refers to the number of bands and their accompanying bandwidths (Harris 1987; Campbell 2006). Multispectral sensors collect data in several bands, each encompassing a wide range of the electromagnetic spectrum, while hyperspectral sensors capture information in many very narrow, contiguous bands throughout the visible, near-infrared (NIR) and mid-infrared (MIR) regions (Lillesand, Chipman & Kiefer 2008).

The sensitivity (quantization levels) with which sensors record small variations in radiance is referred to as the radiometric resolution. The greater the radiometric resolution, the greater the

ability of the sensor to detect small variations in the target objects (Chuvieco & Huete 2010; Mather & Koch 2011).

Temporal resolution is the revisiting period of a particular sensor and varies with the objectives set for the sensor (Chuvieco & Huete 2010).

The most appropriate spatial, spectral, radiometric and temporal resolutions are dependent on the problem at hand (Chuvieco & Huete 2010). These characteristics need to be taken into careful consideration in conjunction with the classifications that need to be performed. High spatial, spectral and radiometric resolutions will allow an evaluation of small objects with varying spectral responses at different wavelengths. Section 2.1.1 will be focusing on surface reflectance properties.

2.1.1 Surface reflectance properties

EMR interacting with the Earth's surface can either be reflected, absorbed or transmitted. Reflection is the result of redirected light as it interacts with a surface object, whereas transmission occurs when light energy passes through an object without significant attenuation (Campbell 2006). The nature of the surface, the wavelength of the energy and the angle of illumination determine the amount of reflection, absorption and transmission that will occur (Lillesand, Chipman & Kiefer 2008). This section focuses on the reflectance properties of soil, vegetation and water.

2.1.1.1 Soil reflectance properties

Spectral reflectance of soils generally increases as wavelength increases (Mather & Koch 2011) and is influenced by the biochemical properties (e.g. organic matter or iron concentration), moisture content, texture and surface roughness of the immediate soil surface (Harris 1987; Lillesand, Chipman & Kiefer 2008; Chuvieco & Huete 2010). Dry soils normally have greater reflectance than moist soil at the same wavelength (Harris 1987), while the presence of iron oxide significantly reduces soil reflectance (Lillesand, Chipman & Kiefer 2008). The visible and NIR regions contain a weak absorption feature at 0.7 to 0.87 μm due to ferric iron, and a strong absorption feature near 1 μm attributed to ferrous iron (Chuvieco & Huete 2010; Mather & Koch 2011). Water absorption bands also occur between 1.3 to 1.5 μm and 1.75 to 1.95 μm , with a decline in reflectance at wavelengths longer than 2 μm if clay minerals are present (Lillesand, Chipman & Kiefer 2008; Mather & Koch 2011). Soil reflectance is the highest in the region between the two water absorption bands (Mather & Koch 2011). Soil moisture content is strongly related to soil texture, with coarse, sandy soils emitting higher reflectance than fine-textured soils, mainly because they tend to be well drained (Lillesand, Chipman & Kiefer 2008).

2.1.1.2 Vegetation reflectance properties

The reflectance properties of vegetation are influenced by the leaf biochemical, plant physiologic and the canopy structural and morphologic properties. Chlorophyll A and chlorophyll B accounts for most (60 to 75%) of the absorption in the blue (0.45 μm) and red (0.65 μm) regions of the EMS, with carotenoids and xanthophylls pigments contributing most in the blue region (0.45 μm) (Chuvienco & Huete 2010). These bands are better known as the chlorophyll absorption bands (Lillesand, Chipman & Kiefer 2008). At 0.55 μm , absorption is less intense, resulting in the green appearance of healthy vegetation (Harris 1987; Chuvienco & Huete 2010). Reflectance from vegetation canopy increases sharply between 0.65 and 0.76 μm (red edge (RE)), remaining high in the NIR region (0.75 to 1.35 μm). Internal leaf structure has an impact on reflectance between 1.35 and 2.5 μm , but reflectance is mostly influenced by leaf water content at 1.45 and 1.95 μm (Chuvienco & Huete 2010; Mather & Koch 2011).

2.1.1.3 Water body reflectance properties

Water generally has a low reflectance compared to other land cover features, but has higher reflectance in the visible region of the electromagnetic spectrum, which then decreases beyond 0.7 μm (Harris 1987; Campbell 2006), with almost no reflection in the NIR region of the spectrum (Mather & Koch 2011). Reflectance from water bodies is influenced by water depth, chlorophyll content, dissolved particles and surface roughness (Chuvienco & Huete 2010). Higher reflectance occurs at the blue-green portion of the spectrum for clear water bodies, with increasing green reflectance and decreasing blue reflectance as chlorophyll content increases. Water containing high quantities of sediment resulting from soil erosion tends to have higher reflectance than clear water (Lillesand, Chipman & Kiefer 2008; Mather & Koch 2011). Shallow water bodies have greater reflectance than deep water bodies, with virtually no NIR reflectance at a depth of 20 m or more (Campbell 2006).

2.1.2 Pre-processing of imagery

Pre-processing is the correction of deficiencies and the removal of flaws present in satellite imagery (Mather & Koch 2011). This is performed before any analysis is carried out on satellite imagery. Sources of error can be grouped into four categories (Chuvienco & Huete 2010):

1. Errors caused by the sensor platform. This includes geometrical problems resulting from variations in velocity, orbit altitude and orientation along the three axes (roll, pitch and yaw);
2. Distortions produced as a result of the Earth's rotation;

3. Radiometric and geometric distortions caused by sensor performance, such as geometric deformation caused by the sensor zenith angle and calibration deterioration; and
4. Effects of the atmosphere on the Earth's radiance, namely scattering (aerosols, gases and water vapour) and attenuation of the signal arriving at and leaving from the surface to the sensor.

Not all of these errors are corrected at receiving stations, and therefore need to be handled by the analyst. Pre-processing steps typically include geometric (orthorectification) and radiometric (e.g. atmospheric correction) corrections (Campbell 2006).

2.1.2.1 Orthorectification

Orthorectification (or geometric correction) corrects distortions caused by variations in altitude, attitude and velocity of the sensor platform in relation to earth curvature, atmospheric refraction, relief displacement and panoramic distortions. The result is a geometrically corrected image (Lillesand, Chipman & Kiefer 2008). The process requires the collection of ground control points (GCPs) to relate the image coordinate system to a geographic coordinate system (Mather & Koch 2011). GCPs should be evenly distributed throughout the image, with good coverage near the image edges (Campbell 2006). This is followed by resampling, a process that estimates the pixel values of the geometrically corrected image based on the uncorrected image pixels. Three resampling approaches are most commonly used (Chuvieco & Huete 2010): nearest neighbour (NN), bilinear interpolation and cubic convolution. NN assigns each pixel in the corrected image the value of the nearest pixel in the uncorrected image. Compared to the other two methods, this approach requires the least computational time and involves less transformation of the original DN's, but distortions are introduced in linear features (highways, roads and geological faults). Bilinear interpolation weighs each nearest pixel based on their distance to the corrected pixel, taking four pixels into account. Pixels nearest to the corrected pixel have the highest weight (Lillesand, Chipman & Kiefer 2008). The cubic convolution resampling approach determines each corrected pixel value by considering the nearest 16 pixels in the uncorrected image. Both bilinear interpolation and cubic convolution reduce the effect of linear distortions, but the original pixel values are altered and the methods are more computationally intensive than NN (Campbell 2006).

2.1.2.2 Atmospheric correction

The atmosphere modifies both the downward solar irradiance and the upward surface radiance leaving the earth (Chuvieco & Huete 2010). As mentioned in Section 2.1.2, the magnitude of the true ground-leaving radiance from a point are attenuated due to atmospheric absorption and its directional properties are altered by scattering (Mather & Koch 2011). Variations in the

illumination geometry, namely the slope of the ground, disposition of topographic features and the sun's elevation and azimuth angles, also have an effect (Lillesand, Chipman & Kiefer 2008; Mather & Koch 2011). Another factor that needs to be taken into account is the angle of observation as it determines the path length of the atmosphere, especially when working with off-nadir (e.g. SPOT) or wide swath angle sensors (e.g. MODIS) (Chuvieco & Huete 2010). Taking these factors into account allows earth surface parameters such as reflectance, emissivity and temperature to be extracted (Richter 2014). Well-known atmospheric correction models include ATCOR (Richter 2014) and fast line-of-sight atmospheric analysis of spectral hypercubes (FLAASH). ATCOR performs atmospheric and topographic correction of optical imagery covering the solar spectral (0.4-2.5 μm) and thermal (8-14 μm) regions (Richter 2004), whereas FLAASH covers the visible to short-wave infrared (SWIR) regions (Cooley et al. 2002). The former is available in the PCI Geomatica and the latter in the ENVI software package (Chuvieco & Huete 2010).

2.1.3 Image classification

Image classification is the process of assigning informational (e.g. land cover) classes to all pixels in a remotely sensed image (Lillesand, Chipman & Kiefer 2008). Several classification approaches will be discussed in this section, namely unsupervised-, supervised- and rule-based classification. This will be followed by a description of well-known machine learning (ML) classifiers, including the *k*-nearest neighbour (*k*NN), maximum likelihood (MaxL), support vector machine (SVM), decision tree (DT) and random forest (RF) algorithms.

2.1.3.1 Unsupervised classification

Unsupervised classification is particularly useful when no prior knowledge (e.g. training samples) of the study area is available (Liu & Mason 2009). The approach makes use of clustering (Campbell 2006; Chuvieco & Huete 2010), which involves the identification of natural groups within a feature set. These natural groups identified by the unsupervised classification are called spectral classes. Identification of the spectral classes that best represent informational classes is performed by the analyst after the clustering has been carried out (Mather & Koch 2011). The analyst needs to compare the resulting spectral classes to some form of reference data in order to assign a particular class to each natural group (Lillesand, Chipman & Kiefer 2008). A major advantage of unsupervised classification is that no prior knowledge of the study area is required, but the approach may result in spectrally homogeneous classes that do not correspond to the informational category that is of interest to the analyst (Campbell 2006). Well-known

unsupervised classifiers include *k*-means, modified *k*-means and ISODATA (Mather & Koch 2011).

2.1.3.2 Supervised classification

The supervised classification approach classifies pixels of unknown identity by making use of samples of known identity, called training samples (Campbell 2006). Prior knowledge of the study area is therefore required by means of secondary sources or fieldwork. This allows the analyst to better identify representative areas for each target category. These areas are known as training fields (Chuvieco & Huete 2010). Supervised approaches consist of three stages, namely the training stage, classification stage and the output stage (Lillesand, Chipman & Kiefer 2008). During the training stage, the analyst identifies training samples suitable for each category (or class) and develops a numerical description of the target classes. The classification stage categorizes each pixel based on the class it most closely relates to. Lastly, an output is produced consisting of the classified study area (output stage). The selection of training samples within training fields is clearly an important step for a successful supervised classification, where the objective should be to collect sufficient training samples to accurately represent the spectral variation within each informational category (Campbell 2006; Mather & Koch 2011). A disadvantage of supervised classifiers is that the method is often biased due to the analyst assigning categories prior to considering the spectral characteristics of the image (Chuvieco & Huete 2010).

2.1.3.3 Rule-based classification

Rule-based approaches discriminate between target categories by establishing a set of rules (a ruleset) that is applied sequentially. The rules often consist of thresholds applied on the spectral values or other data sources (ancillary data), such as aspect, slope and elevation (Chuvieco & Huete 2010). The approach is very flexible to input data, allowing each informational class to be extracted from a subset of the input data as opposed to the entire feature set (Mather & Koch 2011).

Classification and regression trees (CART) is a well-known algorithm used to build DTs (Lawrence & Wright 2001). It recursively divides a feature set until an optimal degree of homogeneity is found at the terminal nodes. Results are improved by means of cross-validation using samples not used to build the trees, a process known as pruning (Chuvieco & Huete 2010). Pruning helps to minimize overfitting, a condition where the results are tailored to particular datasets (Lawrence & Wright 2001; Campbell 2006). CART is very sensitive to variations in the number of training samples and it is therefore important to ensure that the number of training samples for each category is balanced (Campbell 2006).

2.1.3.4 Pixel-based and object-based classifications

Pixel-based classifiers apply decision logic on a per-pixel basis, that is, to each pixel individually in isolation (Lillesand, Chipman & Kiefer 2008). Such an approach can be effective when the spatial resolution is similar to the information classes (land cover features) of interest (Duro, Franklin & Dubé 2012), but is not effective when the target features are larger than the pixel size.

Object-based approaches aggregate image pixels into non-intersecting, homogeneous image objects by making use of a segmentation algorithm. The results of multi-resolution segmentation (Comer & Delp 1995; Comer & Delp 1999), one of the most popular segmentation algorithms (Belgiu & Drăguț 2014), depend on the input data (e.g. spectral values) and the specified parameters (shape, compactness and scale) for the segmentation algorithm (Lillesand, Chipman & Kiefer 2008). The spectral homogeneity and the shape of the objects are influenced by the shape parameter, where the compactness factor adjusts the smoothness of boundaries and the compactness of edges. The scale parameter is the most crucial and influences the size of the produced objects by the segmentation algorithm (Myint et al. 2011). The resulting image objects are then classified (Liu & Xia 2010). Image objects allow the inclusion of additional information, namely texture, shape, the spatial relationship of image objects with neighbouring objects and ancillary spatial data (e.g. elevation) (Hussain et al. 2013). This approach also has the advantage of reducing within-class spectral variation and the severity of the well-known “salt-and-pepper” effect that is common in pixel-based approaches (Liu & Xia 2010). Even though object-based classifications have been shown to produce higher overall accuracies compared to pixel-based methods (Yan et al. 2006; Myint et al. 2011), the method has some limitations. The major disadvantages associated with object-based classification is over-segmentation and under-segmentation. The former occurs when real-world objects are segmented into smaller image objects, whereas the latter occurs when several different real-world objects are grouped into a single large image object (Liu & Xia 2010; Hussain et al. 2013).

Another problem associated with both pixel-based and object-based classifications is mixed pixels. Mixed pixels occur when pixels do not occupy a single homogenous class, representing the average brightness of several categories rather than one. Mixed pixels may also represent the brightness values of another category and increase in number as the spatial resolution of the image decreases (Campbell 2006). A pixel is also not a true geographic object in that each pixel is a cell representation of spectral values in a matrix that lacks real-world correspondence (Hussain et al. 2013). Long, linear features (e.g. roads) or features on the edges of large parcels, where contrasting reflectance values are immediately adjacent to one another, are the regions where mixed pixels

often occur. Both pixel-based and object-based classifications become problematic when a feature of interest is small relative to the spatial resolution of the image (Campbell 2006).

Duro, Franklin and Dubé (2012) compared pixel-based and object-based approaches by applying DT, MaxL and RF classifiers to SPOT-5 imagery in an agricultural setting. The results showed that object-based approaches produced a more visually appealing and generalized appearance for the land cover classes, but the improvement in overall accuracy (OA) of the object-based approach was not statistically significant compared to the OA of the pixel-based approach. The object-based approach was also found to be much more time-consuming than pixel-based classifications (Duro, Franklin & Dubé 2012). Cleve et al. (2008) found object-based approaches to better represent built area (e.g. urban) and surface vegetation, but yielded similar accuracies to pixel-based classifiers for the shadow and tree/shrub classes. Research performed by Yan et al. (2006) found both approaches to produce poor accuracies when classifying geological features (e.g. limestone, metamorphic and mixed sandstone with shale), and similar accuracies were observed for the agricultural and the river classes.

2.1.3.5 Parametric classifiers

A parametric classifier assumes the training data follow a normal (or Gaussian) distribution, which allows the classifier to calculate essential parameters (Jain, Duin & Mao 2000). Such classifiers extract the distribution from the data for each class by estimating the mean vector and the covariance matrix. The parametric classification (e.g. MaxL) is then based on the definition of some discriminant function based on the calculated parameters. Major disadvantages of parametric classifiers are that they assume that classes are symmetric in multispectral space and that they only use fixed-form decision boundaries (Hubert-Moy et al. 2001).

The MaxL is a well-known parametric classifier that makes use of training data to estimate the means and variances of the classes by assuming the training data are normally distributed (Harris 1987; Gibson & Power 2000). These estimates are then used to determine the probabilities for each class (Rees 2001; Albert 2002; Lillesand, Chipman & Kiefer 2008). According to Campbell (2006), MaxL is very sensitive to the quality of the training data and a decrease in accuracy has been observed with an increase in input features (Myburgh & Van Niekerk 2013). More information about the MaxL classifier is provided in the next section.

2.1.3.6 Machine learning classifiers

Non-parametric classifiers do not make any assumptions about the distribution of the training data and do not estimate parameters (Jain, Duin & Mao 2000). This is especially advantageous when

working with RS data, which are (in most cases) not normally distributed. ML thus provides good generality and versatility when it comes to classifications (Hubert-Moy et al. 2001).

Several ML classifiers are available for use in RS, including k NN, SVM, DT and RF. Short overviews of these classifiers are provided in this section. More details on ML and the different algorithms are provided in Sections 3.3.2.7 and 4.3.3.3.

k NN is a simple non-parametric, distance-based classifier that labels each unknown instance based on its k neighbouring known instances. A class is assigned to the unknown instance best represented by the training samples among the k neighbours (Cover & Hart 1967; Gibson & Power 2000). The k NN algorithm is effective in classifying data that is not normally distributed, but has the disadvantage of assigning equal weight to all variables even though certain variables may have higher priority. This can result in incorrect class assignments and diffuse clusters (Cunningham & Delany, 2007). To avoid this, only odd k -values (e.g. 1, 3 and 5) should be used, as suggested by Campbell (2006).

The efficiency of SVM classifiers for RS applications has been demonstrated by Lizarazo (2008), Li et al. (2010), Petropoulos, Kalaitzidis, and Prasad Vadrevu (2012). Myburgh and Van Niekerk (2013) showed that SVM produces more accurate results than k NN and MaxL for land cover mapping using SPOT-5 imagery. SVM determines the optimal separating hyperplane between classes (Novack et al. 2011) by focussing on the training samples close to the edge (support vector) of the class descriptors (Tzotsos & Argialas 2006; Lizarazo 2008). In cases where the relationship between classes and features are non-linear, the radial basis function (RBF) kernel is often applied (Li et al. 2010). (See Vapnik (2000) and Huang, Davis and Townshend (2002) for a detailed mathematical formulation of SVM.)

A DT identifies relationships between a continuous response variable, known as the dependent variable, and multiple, continuous variables known as the independent variables. DTs hierarchically split a dataset into increasingly homogeneous subsets known as nodes (Lawrence & Wright 2001; Pal & Mather 2003; Punia, Joshi & Porwal 2011; Novack et al. 2011; Gómez et al. 2012). By recursively splitting the feature datasets, a leaf node is reached, with the class associated with the node assigned to the observation (Pal & Mather 2003). According to Pal and Mather (2003) and Novack et al. (2011), each node is limited to a split in feature space orthogonal to the axis of the selected feature. Each branch of the DT consists of divisions (or rules) of the most probable class. Applying these rules will assign the most likely class to an unknown instance (Lawrence & Wright 2001).

There has been a notable increase in the use of the RF classifier for RS applications (Gislason, Benediktsson & Sveinsson 2006; Lawrence, Wood & Sheley 2006; Duro, Franklin & Dube 2012;

Immitzer, Atzberger & Koukal 2012) and it has been shown to be effective for many classification tasks (Lawrence and Wright, 2001; Gislason et al., 2006; Novack et al., 2011; Rodriguez-Galiano et al., 2012a; Rodriguez-Galiano et al., 2012b). RF, an enhancement of DTs (Immitzer, Atzberger & Koukal 2012), generates each DT by using a random vector sampled independently from the input vector. A vote is cast by each of the generated DTs (Leo Breiman 2001; Pal 2005; Bosch, Zisserman & Muoz 2007). Each classifier contributes a single vote to the assignment of the most popular class of the input variable (Breiman 2001; Rodriguez-Galiano et al. 2012a). RF makes use of bagging (Breiman 1996; Rodriguez-Galiano et al. 2012a), a method which generates a training set for feature selection. This allows RF classifiers to have a low (even lower than DT classifiers) sensitivity to training set size (Rodríguez-Galiano et al. 2012a). Two parameters are required to be set, namely the number of trees and the number of active (predictive) variables. Rodríguez-Galiano et al. (2012a) showed that stability in accuracy is achieved at 100 trees and that a small number of split variables are optimal for reducing generalization errors and correlations between trees. A more detailed discussion of the RF classifier can be found in Breiman (1996), Breiman (2001), Pal (2005) and Rodríguez-Galiano et al. (2012a). The next section deals with Geomorphometry, focusing on digital elevation models, digital terrain modelling and terrain derivatives.

2.2 GEOMORPHOMETRY

Geomorphometry consists of a set of processes that produces a compilation of terrain characteristics. The resulting terrain characteristics are evaluated along with other properties to assign a value to a land unit, expressed either by a numeric value or by a judgement of its worth in qualitative terms (Townshend et al. 1981; Hengl, Gruber & Shrestha 2003).

2.2.1 Digital elevation models

A digital elevation model (DEM) can be defined as a digital or numerical representation of terrain (Li, Zhu & Gold 2004). Figure 2.2 shows a comparison between a digital terrain model (DTM) and a digital surface model (DSM). A DSM represents the uppermost level of surface features, namely vegetation canopies and buildings (Hengl, Gruber & Shrestha 2003), while DTMs do not include such surface features and can therefore be described as a “bare earth model” (Liu & Mason 2009), representing only the terrain surface (Hengl, Gruber & Shrestha 2003; Campbell 2006).

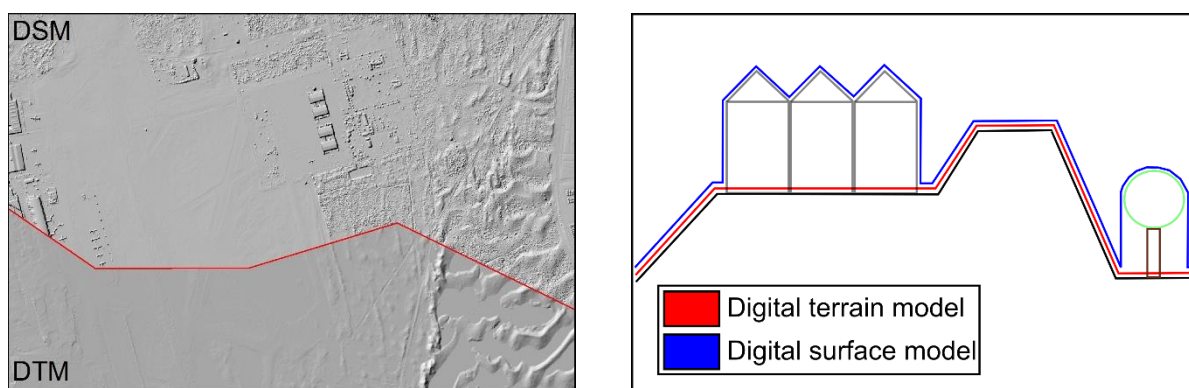


Figure 2.2: Difference between digital terrain models (DTM) and digital surface models (DSM)

An elevation dataset can either be stored as a raster (grid) or a vector triangulated irregular network (TIN). The TIN model represents the surface through contiguous, irregularly shaped triangles, whereas the raster format makes use of a matrix consisting of regularly spaced rows and columns. The coordinates associated with each node of a raster can be computed based on the coordinates of the origin of the area (Li, Zhu & Gold 2004).

2.2.2 Digital terrain modelling

Digital terrain modelling makes use of mathematical modelling to construct a DEM (Hengl, Gruber & Shrestha 2003; Li, Zhu & Gold 2004). DEM generation can be accomplished by means of photogrammetry, light detection and ranging (LiDAR) or synthetic aperture radar interferometry (InSAR) (Liu & Mason 2009). Photogrammetry is the process of obtaining useful spatial measurements and geometrically accurate data from photographs, namely DEM generation from stereoscopic images, thematic data and orthophotos (Lillesand, Chipman & Kiefer 2008).

Height can be obtained from two or more images covering the same scene. The ability to do this is known as stereoscopy (Campbell 2006). When two or more images of the same scene are captured from different perspectives, a displacement of objects is found from one image to another. Stereoscopic parallax, which increases as the distance between the object and the observation point increases, allows for distance or height measurements (Zomer, Ustin & Ives 2002; Fabris & Pesci 2005; Campbell 2006; Stal et al. 2013). An example of stereoscopic DEM development is the so-called advanced spaceborne thermal emission and reflection radiometer (ASTER) stereoscopic subsystem, which consists of nadir- and rear-viewing sensors that capture data in the NIR region of the spectrum. The captured stereo pair allows for the generation of a DEM consisting of an accuracy ranging from 15 m to 30 m, depending on the number of available GCPs for the region (Abrams 2000).

LiDAR is an active sensor that emits laser pulses to the observed surface and measures the time of pulse return (Lillesand, Chipman & Kiefer 2008; Chuvieco & Huete 2010). The computed return

time is then used to calculate the distance travelled by the emitted light to obtain the height of the surveyed ground position (Liu & Mason 2009). Imaging LiDARs are nadir viewing sensors that capture information in very narrow bands of wavelength in the visible and NIR region of the spectrum (Mather & Koch 2011). The NIR region has the ability to delineate open water, is sensitive to vegetation and has freedom from atmospheric scattering, whereas the green region is used to penetrate water bodies (Campbell 2006). Most LiDAR sensors are airborne, with the deactivated geoscience laser altimeter system (GLAS) being the most recent satellite platform sensor (Chuvieco & Huete 2010).

Radio detection and ranging (RADAR) is an active sensor that captures electromagnetic energy in the microwave region of the spectrum (Campbell 2006). Types of sensors include side-looking radar (SLR), side-looking airborne radar (SLAR) and the more modern synthetic aperture radar (SAR) systems (Lillesand, Chipman & Kiefer 2008). The spatial resolution of SLR and SLAR is dependent on orbital height and antenna length, with larger orbital heights increasing the required length of the antenna to achieve a reasonable spatial resolution (Mather & Koch 2011). This is very impractical for satellite borne sensors as an antenna of enormous proportions will be required (Chuvieco & Huete 2010). SAR synthesises a longer antenna length based on the Doppler principle (Li, Zhu & Gold 2004). It records the amplitude and the phase of the return signals, which allows the calculation of the object position relative to the antenna (Mather & Koch 2011). A pair of SAR images and the recorded phase differences can then be used to derive a topographic map of the earth's surface. This approach is a signal processing technique called InSAR (Li, Zhu & Gold 2004). The Shuttle Radar Topographic Mission (SRTM) made use of interferometric methods to create a worldwide DEM at a 30 m spatial resolution (Rabus et al. 2003; Hensley, Rosen & Gurrola 2000).

2.2.3 Terrain derivatives

DEMs allow for the extraction of several morphological and hydrological terrain parameters. Morphological terrain parameters are derived from DEMs by making use of neighbourhood operations to determine the rate of change, namely slope aspect, slope gradient and curvature. Hydrological (flow accumulation based) terrain parameters model the mass movement of water, nutrients and sediments between land units (Hengl, Gruber & Shrestha 2003; Li, Zhu & Gold 2004; Mather & Koch 2011). A brief overview of morphological and hydrological terrain parameters is provided in Sections 2.2.3.1 and 2.2.3.2 respectively. More detailed discussions can be found in Hengl, Gruber and Shrestha (2003) and Olaya (2004). The derivatives described below are all available in the System for Automated Geoscientific Analyses (SAGA) (Conrad et al. 2015).

2.2.3.1 Morphological terrain parameters

Morphological terrain parameters can be grouped as follows (Hengl, Gruber & Shrestha 2003):

- elevation change gradient (e.g. slope);
- orientation change gradient (e.g. aspect); and
- curvature gradient (e.g. plan and profile curvature).

Slope gradient (often simply called slope), the rate of change in elevation in the x- and y-direction, is calculated by computing the geometric mean of the cardinal and diagonal slopes in a 3×3 neighbourhood. High slope gradient values represent steep surfaces, whereas lower values represent flatter surfaces (Behrens et al. 2010). Slope aspect (shortened to aspect) is defined as the azimuth angle of the sloping surface. Values range from 0 to 360° (Li, Zhu & Gold 2004). Mid-slope position (MSP) is computed by allocating zero to mid-slope positions, whereas a value of one is allocated to maximum vertical distances to the mid-slope (e.g. valleys and ridges). Normalized height (NH) is calculated by assigning zero to the lowest point and one to the highest point in an elevation grid. Standardized height (STDH) is produced by multiplying the absolute height with the NH (Dietrich & Böhner 2008). Both NH and STDH take into account the size of the catchment area and the vertical offset of a position (Böhner & Selige 2006).

Curvature expresses the convexity or concavity of a surface, which includes measurements such as profile, plan and mean curvature. Profile (vertical) curvature, which is tangential to a contour, represents the ratio between the mean slope of cells with lower height values than the centre cell, and the mean slope calculated from the cells with higher cell values surrounding the centre cell. A convex profile is represented by positive profile curvature values, whereas negative values signify a concave surface. Plan (horizontal) curvature focuses on the aspect of the centre cell's neighbouring pixels and is tangential to a flow-line (Behrens et al. 2010). A positive plan curvature indicates divergence of flow and negative values represent concentrations of flow. Mean curvature is a measurement of the average plan curvature. Mean-convex landforms are described by positive mean curvature, where negative values describe mean-concave landforms (Hengl, Gruber & Shrestha 2003). Other curvature measurements include the longitudinal, cross-sectional, minimum and maximum curvatures (Wood 1996).

Additional well-known morphological derivatives include downslope distance gradient (DDG) (Hjerdt et al. 2004), convergence index, slope height (SH), valley depth, relative slope position (RSP), terrain ruggedness index (TRI), terrain surface texture and the topographic position index (TPI) (Olaya 2004; Böhner, Blaschke & Montanarella 2008; Conrad et al. 2015).

2.2.3.2 Hydrological terrain parameters

Hydrological terrain analysis is dependent on the flow model, including flow direction, flow accumulation, drainage network and catchments. Flow direction is based on water's downhill flow, i.e. from a higher to a lower point. This allows flow direction to be determined from a DEM (Li, Zhu & Gold 2004). Calculation of flow direction can be performed by using the deterministic eight-node (D8) method (Zhou & Liu 2002; Olaya 2004). The D8 method records flow in one of eight directions, namely north, east, south, west, north-east, north-west, south-east and south-west. Flow direction will always be in the direction of the largest downslope. Flow accumulation can be determined from a produced flow direction dataset. Defined as the flow of water across a landscape, flow accumulation assigns each pixel the number of pixels that flow through it (Evans, Caccetta & Ferdowsian 1996). Pixels with zero flow accumulation represent peaks and ridge lines. Flow lines (drainage network) and catchments (watersheds) can subsequently be delineated from the flow accumulation dataset. A simple threshold value can be used to obtain the drainage network; whereas watersheds are delineated by forming a polygon along the ridge lines (zero flow accumulation) (Li, Zhu & Gold 2004).

The topographic wetness index (TWI), also known as the compound topographic index, describes the tendency of terrain to accumulate water (Hengl, Gruber & Shrestha 2003). High TWI values are an indication of high soil moisture (Olaya 2004). TWI can be defined as (Beven & Kirkby 1979):

Equation 2.1

$$\text{TWI} = \ln \frac{\alpha}{\tan \beta}$$

where $\tan \beta$ is the local upslope of the terrain surface; and α is the upslope area per contour length, which can be computed as (Beven & Kirkby 1979):

Equation 2.2

$$\alpha = \frac{A}{L}$$

where A is the upslope area and L is the contour length. Two noteworthy assumptions are made by TWI, namely that the hydraulic conductivity of the soil and precipitation is uniform, and that the groundwater table slope is adequately represented by the terrain surface slope (Sørensen & Seibert 2007). A modified version of the TWI, known as the SAGA wetness index (SWI), estimates a more realistic soil moisture for regions with small vertical distances to channels, such as valley floors. This is accomplished by making use of a modified catchment area calculation that does not simulate flow as a thin line (Böhner et al. 2002).

The height above nearest drainage (HAND) model produces a normalized DEM according to vertical distance distribution relative to drainage channels by making use of two steps (Rennó et al. 2008). First, the model produces a hydrologically sound DEM (e.g. removal of pits), delineates flow paths and extracts the channel network. This is followed by several computations performed on local drainage directions and the drainage network to produce the nearest drainage grid, or HAND model. Good drainage can be associated with high HAND values, whereas regions with poor drainage will consist of low HAND values. Regions with low drainage potential will more likely result in an accumulation of water, and therefore waterlogging (Nobre et al. 2011; Cuartas et al. 2012). A more detailed discussion on the HAND model's computations are available in Rennó et al. (2008).

2.3 GEOSPATIAL TECHNIQUES FOR DETECTING AND MODELLING SALT ACCUMULATION

This section deals with viable approaches for monitoring salt accumulation, namely spectral analysis, vegetation stress monitoring, spatial indices, separability analysis, regression analysis, principal component analysis and geostatistics. First, a discussion on the spectral response of salt-affected soils, including the salinity indices (SIs) calculated from multispectral imagery, is provided. This is followed by an overview of vegetation stress monitoring, spatial indices (e.g. texture), separability analysis and statistical approaches, namely regression modelling (RM), principal component analysis (PCA) and geostatistics, as these methods have been shown to be effective for delineating salt-affected soils.

2.3.1 Spectral analysis (direct approach)

The spectral response and the direct detection of salt-affected soils have been the focus of numerous RS studies (Khan et al. 2005; Abbas et al. 2013; Al-Khaier 2003; Setia et al. 2013; Wang et al. 2013). According to (Metternicht & Zinck 2003), the reflectance from salts is affected by salt quantity, salt mineralogy, surface roughness, soil colour and soil moisture. Khan et al. (2005) and Abbas et al. (2013) found that salt-affected soils have higher reflectance compared to other land cover or land use classes (e.g. crops, urban, water bodies). Similar results were found by Dwivedi and Sreenivas (1998). They showed that salt-affected affected soils have higher spectral responses than crops and waterlogged soils and reported that waterlogged soils have a lower spectral response in the NIR region of the spectrum, while having similar spectral responses to vegetation in the green and red bands due to the presence of hydrophytic vegetation. Several studies have shown that salt-affected soils have higher reflectance than unaffected soils (Al-Khaier 2003; Khan et al. 2005; Setia et al. 2013; Wang et al. 2013). Setia et al. (2013) also found that

highly saline soils consist of bright white patches, whereas moderately affected soils appear dull white and are similar in spectral response to soils affected by low salt accumulation. Utilizing the IRS-1B LISS II sensor, Abbas & Khan (2007) and Abbas et al. (2013) found a strong relationship between salt-affected soils and the visible spectrum (blue, green and red bands), but a poorer relationship was observed with the NIR band. Based on this research, the following SIs were developed (Abbas & Khan 2007):

Equation 2.3

$$S_1 = \frac{Blue}{Red}$$

Equation 2.4

$$S_2 = \frac{Blue - Red}{Blue + Red}$$

Equation 2.5

$$S_3 = \frac{Green \times Red}{Blue}$$

Equation 2.6

$$S_4 = \sqrt{Blue \times Red}$$

Equation 2.7

$$S_5 = \frac{Blue \times Red}{Green}$$

Equation 2.8

$$S_6 = \frac{Blue \times Red}{Green}$$

where S_1 - S_6 is the SI;
Blue is the blue band;
Green is the green band;
Red is the red band; and
NIR is the NIR band.

A high correlation between measured soil EC and SI S_3 was found in Abbas and Khan (2007), but a more recent study (Abbas et al. 2013) showed SI S_4 to perform better. Another SI is the normalized difference salinity index (NDSI) (Al-Khaier 2003):

$$NDSI = \frac{Red - NIR}{Red + NIR}$$

where $NDSI$ is the SI;
 Red is the red band; and
 NIR is the NIR band.

NDSI is essentially an inverse of the normalized difference vegetation index (NDVI) and as such produces low values for vegetation and high values for salt-affected soil. Khan et al. (2005) found NDSI to more accurately delineate salt-affected soils than SI S₄. Significant correlations ($R^2 = 0.57$; $p < 0.05$) were observed between NDSI and saline soil by Douaoui & El Ghadiri (2015). A strong relationship between the Quickbird sensor's green (520-600 nm) and NIR (760–900 nm) bands was also found with salt-affected soil (Setia et al. 2013). Utilizing the WorldView-2 (WV2) sensor bands, Abood, Maclean and Falkowski (2011) proposed the following variations of the NDSI:

Equation 2.10

$$NDSI_1 = \frac{Yellow - NIR_1}{Yellow + NIR_1}$$

Equation 2.11

$$NDSI_2 = \frac{Yellow - NIR_2}{Yellow - NIR_2}$$

Equation 2.12

$$NDSI_3 = \frac{Red - NIR_1}{Red + NIR_1}$$

Equation 2.13

$$NDSI_4 = \frac{Red - NIR_2}{Red + NIR_2}$$

Equation 2.14

$$NDSI_5 = \frac{RE - NIR_1}{RE + NIR_1}$$

Equation 2.15

$$NDSI_6 = \frac{RE - NIR_2}{RE + NIR_2}$$

where $NDSI_1-NDSI_6$ is the SI;

| | |
|------------------------|-----------------------------------|
| <i>Yellow</i> | is the yellow band; |
| <i>Red</i> | is the red band; |
| <i>RE</i> | is the red edge band; |
| <i>NIR₁</i> | is the NIR ₁ band; and |
| <i>NIR₂</i> | is the NIR ₂ band. |

Abood, Maclean and Falkowski (2011) found that the high soil reflectance in the visible bands (especially in the yellow band) makes NDSI₁ useful for delineating salt-affected soils, but that NDSI₂ provided better results owing to the relatively low reflectance of wet soils and water in the NIR₂ band. NDSI₄ and NDSI₅ performed poorly, which was attributed to the low reflectance of salts in the red and RE bands.

Fernandez-Buces et al. (2006) proposed a combined spectral response index (COSRI) to enunciate the combination of spectral responses of bare soil and vegetation. COSRI is defined as:

Equation 2.16

$$COSRI = \left(\frac{Blue + Green}{Red + NIR} \right) \times NDVI$$

| | | |
|-------|--------------|--|
| where | <i>COSRI</i> | is the SI; |
| | <i>Blue</i> | is the blue band; |
| | <i>Green</i> | is the green band; |
| | <i>Red</i> | is the red band; |
| | <i>NIR</i> | is the NIR band; and |
| | <i>NDVI</i> | is the normalized difference vegetation index. |

Vegetated areas will result in large COSRI values due to high reflectance in the NIR bands and low reflectance in the visible bands, whereas negative index values will be yielded for clouds, water, or salt-affected soils that have high reflectance values in the visible spectrum and low reflectance values with the NIR bands. Small concentrations of salt on the surface will result in index values close to zero (Fernandez-Buces et al. 2006). Wang et al. (2013) found COSRI to provide a good estimate of measured soil EC values ($R^2 = 0.72$).

2.3.2 Vegetation stress monitoring (indirect approach)

Performance-related indicators focus on the identification of plant stress caused by salt accumulation (Muller & Van Niekerk 2016a). As explained in Section 2.1.1.2, healthy vegetation has a low reflection at the blue and red bands of a RS sensor, whereas the green region produces a higher reflectance from vegetation canopy. Stressed vegetation also has a lower reflectance (than

healthy vegetation) in the NIR region of the spectrum (Harris 1987). Vegetation indices (VIs) take these vegetation properties into account by performing transformations on two or more bands, typically the chlorophyll-absorbing red region (0.6 to 0.7 μm) and the high reflecting NIR region (0.75 to 1.35 μm) of the spectrum. Band transformations are done in a manner that minimizes non-vegetation response and maximizes vegetation response (Chuvieco & Huete 2010). Several VIs are available, namely the simple ratio index (SRI), normalized difference vegetation index (NDVI) and soil-adjusted vegetation index (SAVI). Each of these VIs produce high values for healthy vegetation. SRI is a simple ratio-based index defined as (Campbell 2006):

Equation 2.17

$$SRI = \frac{NIR}{Red}$$

where SRI is the VI;
 Red is the red band; and
 NIR is the NIR band.

NDVI is a variant of the SRI with a dynamic range of -1 to 1. The NDVI is very popular for RS use because the VI compensates for changing surface slope, aspect, illumination conditions and other irrelevant factors. NDVI is defined as (Lillesand, Chipman & Kiefer 2008):

Equation 2.18

$$NDVI = \frac{NIR - Red}{NIR + Red}$$

where $NDVI$ is the VI;
 Red is the red band; and
 NIR is the NIR band.

SAVI is an optimization of the NDVI as it reduces the reflected bare ground signal. This is done by including a parameter (L) related to the differential penetration of red and NIR light through the vegetation canopy. SAVI is defined as (Chuvieco & Huete 2010):

Equation 2.19

$$SAVI = \left(\frac{NIR - Red}{NIR + Red + L} \right) \times (1 + L)$$

where $SAVI$ is the VI;
 Red is the red band;
 NIR is the NIR band; and
 L is the soil adjustment factor.

The main advantage of performance-related indicators is that the method takes subsurface conditions into account, which is a major limitation of the direct approach (see Section 2.3.1). The indirect approach, however, has several disadvantages, namely that poor vegetation health can be a result of poor farming practices or poor soil preparation (Furby et al. 1995); the effectiveness of VIs can be reduced due to high bare ground reflectance (Douaoui, Nicolas & Walter 2006); and poor correlations between VIs and soil EC has been found due to variations in different crop species' salt tolerances (Maas & Hoffman 1977; Aldakheel 2011).

2.3.3 Spatial indices (texture measures)

Texture contains information on the spatial distribution of tonal variations, where tone is based on the varying shades of grey of cells in an image (Haralick, Shanmugam & Dinstein 1973). Baraldi and Parmiggiani (1995) define texture as the visual effect that is produced by the spatial distribution of tonal variations over relatively small areas, while Irons and Petersen (1981) describes tone as the brightness or darkness of a surface. Texture has been found to be useful for many RS applications (Haralick, Shanmugam & Dinstein 1973; Cai et al. 2010; Odindi & Mhangara 2013). Cai et al. (2010) classified salt-affected soil by making use of a SVM classifier and texture features. Results showed an improved OA with the inclusion of a single texture measure, but best results were achieved by including a combination of several texture measures. The mean, variance and homogeneity texture measures were found to provide the best results for mapping soil salinity. Puissant, Hirsch and Weber (2005) showed that window sizes larger than 7×7 will contribute less to the separation of classes and that homogeneity is the optimal texture measure for RS classifications.

2.3.4 Separability analysis

Feature selection has been shown to improve classification accuracies (Lu & Weng 2007; Myburgh & Van Niekerk 2013), especially when the number of training sets is disproportional to the number of features (Pal & Mather 2005; Oommen et al. 2008; Myburgh & Van Niekerk 2014). Spectral separability analysis of salt-affected soils using the pairwise transformed divergence method and RS data has been performed by Dwivedi and Sreenivas (1998). Salt-affected soils were found to be easily separable from other classes. The Jeffries-Matusita (JM) distance, another separability analysis algorithm, has been used for RS purposes by several researchers (Gao et al. 2011; Laliberte, Browning & Rango 2012). The algorithm identifies variables that have the best separability between classes and can be calculated as (Nussbaum, Niemeyer & Canty 2006):

Equation 2.20

$$J = 2(1 - e^{-B})$$

where J is the JM distance; and
 B is the Bhattacharya distance.

The Bhattacharya distance (B) is the mean and standard deviation of the training samples of the two classes (Bhattacharyya 1943). Ranging from 0 to 2, a J value equal to 2 is an indication of highly separable, uncorrelated classes, whereas a J value equal to 0 represents classes that are completely correlated and therefore inseparable. More classification errors can therefore be expected with lower J values (Heumann 2011). For a more detailed discussion on JM distance see Section 3.3.2.4 and Nussbaum, Niemeyer and Canty (2006).

2.3.5 Regression analysis

Regression analysis is used to describe a functional relationship, which means that the value of one variable (dependent variable) can be determined by the value of the second variable (independent variable), but the reverse is not true (McKillup 2006). The dependent variable can therefore be determined from the independent variable. Stepwise multiple regression is another regression method that can be used to describe a functional relationship (Clark & Kokaly 1999). It fits an observed dependent dataset using a linear combination of independent variables by simultaneously removing variables that are unimportant. Partial least squares (PLS) regression were found by Mashimbye et al. (2012) to be very effective for salt accumulation modelling using spectral data as it reduces a large number of measured collinear spectral variables to a few non-correlated latent variables. This is done by utilizing a bilinear calibration method and using data compression. A linear relationship is specified between a set of dependent variables and predictor variables, thereby extracting the orthogonal predictor variables and accounting for as much of the variation of the dependent variables as possible (Hansen & Schjoerring 2003; Cho et al. 2007; Mashimbye et al. 2012).

2.3.6 Principal component analysis

PCA reduces the number of original images (variables) by identifying the ideal linear combination of the original images that accounts for the variation of pixel values (Campbell 2006). Based on the eigenvectors and eigenvalues of the variance-covariance matrix, principal components are of the form (O'Sullivan & Unwin 2003):

Equation 2.21

$$PC_i = e_{i1}X_1 + \dots + e_{ij}X_j + \dots + e_{ip}X_p$$

where PC_i is the principal component of the data;
 e_i is the eigenvector; and

X_i is the original image data.

The resulting principal component images are statistically uncorrelated and will be equal in number to the number of original images provided (Mather & Koch 2011). The first principal component contains the largest percentage of the total variance, decreasing in percentage with the second principal component, the third principal component and so on. This allows a subset of the resulting principal components to be used for further analysis (Lillesand, Chipman & Kiefer 2008). PCA approaches have been used for detecting soil salinity in agricultural fields with varying success (Eldeiry & Garcia 2008).

2.3.7 Geostatistics

Geostatistics, which includes kriging, is a non-linear, statistical interpolation technique that takes into account the spatial structure of the surface to be interpolated from by analysing the training (sample) data (O'Sullivan & Unwin 2003). Geostatistics have several advantages compared to other interpolation techniques. First, an analysis of the spatial structure of the data is performed. This allows the average spatial variability to be integrated into the estimation in the form of a variogram (semivariogram). Kriging also provides an estimation error, the kriging standard deviation (Wackernagel 2010), and non-linear interpolation eliminates the assumption of linearity present in linear interpolation methods (DeMers 2005). The approach also accounts for clustering when weighing neighbouring points (Gallichand et al. 1992). Kriging relies on a variogram, which is a weighting scheme where sampling points closer to the point of interest are assigned a higher weight than sampling points further from the point of interest (Li et al. 2007). The distance between the plotted samples is called the lag. By making use of a variogram to model the correlations between neighbouring samples, kriging is able to account for autocorrelation (Eldeiry & Garcia 2009). The experimental variogram can be defined as (O'Sullivan & Unwin 2003):

Equation 2.22

$$2\gamma(d) = \frac{1}{n(d)} \sum_{n_{ij}=d} (z_i - z_j)^2$$

where $\gamma(d)$ is the variogram;
 D is the distance between the control points;
 $n(d)$ is the number of pair of points at separation;
 z_i is the value at location i ; and
 z_j is the value at location j .

The squared differences in values between the locations are known as the variances (semivariances) (O'Sullivan & Unwin 2003). Important parameters to take into account when performing kriging is the nugget, range and the sill. The nugget is the variance at zero distance, while the range is the distance at which the variogram levels off and the variance is constant (Wackernagel 2010). The constant variance beyond the range is called the sill (Gundogdu & Guney 2007).

Several variations of the kriging algorithm are available, such as ordinary kriging (OK), co-kriging (CK), universal kriging (UK), kriging with external drift (KED) and regression-kriging (RK). Algorithms that only make use of the primary variable to perform the interpolation are known as univariate, whereas multivariate kriging algorithms make use of explanatory (secondary) variables to calculate the estimation (Wackernagel 2010).

The estimation and mapping of soil attributes have been the principal use of geostatistics by soil scientists (Goovaerts 1999), particularly for interpolating salt accumulation from soil sample analysis results (Gallichand et al. 1992; Utset et al. 1998; Li et al. 2007; Eldeiry & Garcia 2008; Eldeiry & Garcia 2009; Juan et al. 2011; Taghizadeh-Mehrjardi et al. 2014). Bishop and McBratney (2001) found KED to produce better results in estimating EC than OK and RK, while Motaghian and Mohammadi (2011) showed similar results when comparing KED, RM, OK, CK and RK in modelling soil saturated hydraulic conductivity. The importance of incorporating ancillary variables were also noted by Li et al. (2007), in which case CK and RK showed higher performance than OK. For a more detailed discussion on the available kriging methods, see Sections 2.3.7 and 4.3.3.2. More information on the methods can also be found in Goovaerts (1999), Hengl, Heuvelink and Stein (2003) and Hengl, Heuvelink and Rossiter (2007).

2.4 LITERATURE SUMMARY

The literature reviewed in this chapter showed that RS (Section 2.1) and geomorphometry (Section 2.2) holds much potential for identifying and mapping salt-affected soils. More research is clearly needed on the effectiveness of VHR multispectral imagery, as most research focused on low, medium and high resolution imagery. VHR imagery will also be the most appropriate for identifying salt accumulation in South African irrigation schemes, where salt accumulation generally occurs in small, elongated patches. The availability of a multitude of SIs and spatial indices that can be derived from multispectral datasets also increases the potential of multispectral images. These indices can also be produced from hyperspectral imagery, but due to the scarcity and cost of hyperspectral data and the low spatial resolution of currently available datasets, such an approach will not be viable or cost-effective for monitoring salt accumulation over large extents (e.g. irrigation scheme level). Multispectral imagery with several bands (e.g. WV2) allows for the

calculation of more SIs and spatial indices. VHR multispectral imagery is therefore the most appropriate for investigating the potential of the direct approach in the context of this study (see Chapter 3).

Geomorphometry has been shown to be an alternative method for identifying salt accumulation in agricultural fields. The availability of global DEM data (e.g. SRTM DEM), the possibility to derive DEM data from other RS sources (e.g. stereoscopic images), and the potential to derive several morphological and hydrological terrain parameters from elevation data makes geomorphometry an attractive option. LiDAR shows the most potential for producing highly detailed VHR DEMs, but, as with hyperspectral imagery, the scarcity of LiDAR data makes it unfeasible for monitoring salt accumulation on a large scale. DEMs (globally available) and VHR DEMs (generated from freely available stereoscopic imagery) seem to be the most cost-effective elevation sources in the context of this study (see Chapter 4).

Several possible approaches for identifying salt accumulation were discussed in Chapter 2, namely separability analysis, regression analysis, geostatistics (Section 2.3) and ML (Section 2.1.3). Applying these approaches to VHR multispectral and terrain transformations (geomorphometry) to identify the most successful transformation and best performing ML method in mapping salt accumulation is of interest. The potential of ML methods applied to VHR multispectral imagery needs investigation and the occurrence of salt accumulation in small, elongated patches in South African irrigation schemes must also be considered. Geomorphometry has shown potential in identifying salt-affected soil, but more research is needed on the comparison of the performance of ML methods with that of geostatistical algorithms (e.g. KED).

Two experiments were carried out to investigate these gaps in the current knowledge and are discussed in the following two chapters. Chapter 3 focusses on the potential of VHR multispectral imagery and ML in identifying salt accumulation, whereas Chapter 4 presents a comparison of ML methods with geostatistical algorithms, applied to terrain derivatives (geomorphometry). Both experiments were applied in selected South African irrigation schemes.

CHAPTER 3: AN EVALUATION OF MULTISPECTRAL VHR IMAGERY FOR SOIL SALINITY MONITORING*

3.1 ABSTRACT

Conventional methods for monitoring salt accumulation within irrigation schemes involve regular field visits to collect soil samples for laboratory analysis. RS has been proposed as a less time-consuming, cost-effective alternative as it provides imagery covering large areas throughout the year. This study evaluated the efficacy of VHR WV2 imagery to map areas affected by salt accumulation. Classifications based on thresholds obtained from JM distance, RM, CART, as well as supervised classification approaches, were evaluated for discriminating between salt-affected and unaffected soils in Vaalharts, South Africa. The WV2 bands were supplemented with SIs, principal components and texture measures to increase the number of predictive variables. In situ soil samples were used for model development, classifier training and accuracy assessment. The results showed a simple threshold implemented on a NDSI was the most successful in separating classes, with an OA of 80%. The findings suggest that VHR satellite imagery holds much potential for monitoring salt accumulation, but more research is needed to investigate why the classification results tend to overestimate salt-affected areas. More work is also needed to evaluate the transferability of the techniques to other irrigation schemes.

3.2 INTRODUCTION

The term ‘salinity’ is used to describe the processes and impacts of salt and water, while also being a measure of the amount of salt in soil or water (Mcghie 2005). For the purpose of this study, salinity refers to the accumulation of soluble salts in the soil (Al-Khaier 2003). Salt accumulation can occur naturally or as a result of human interference. Processes such as the clearance of vegetation, irrigation and reshaping the landscape through earth works can increase the volume of water and salt in the landscape and change how and where these two components move and accumulate (Mcghie 2005). Salt accumulation is of major concern in many parts of the world due to its negative environmental impact on agricultural areas, which often leads to a reduction in crop yields. Salt accumulation can also lead to lower property values, eutrophication of rivers, damage to infrastructure, increased soil erosion and engineering difficulties (Metternicht & Zinck 2003). According to Ghassemi, Jakeman and Nix (1995), about 77 million hectares (ha) of the global land surface is affected by high salinity caused by human activity. As much as 58% of these salt-affected areas occur in irrigated areas.

*This chapter was published by the Applied Journal of Remote Sensing in Volume 10, Issue 2 (Vermeulen & Van Niekerk 2016) and consequently conforms to the prescribed structure of that journal. Some duplication between the content of this chapter and other chapters (especially Chapters 2 and 4) can also be expected.

Waterlogging, which is caused by poor drainage, is another major concern associated with salt-affected soil. Dwivedi, Sreenivas and Ramana (1999) states that an area becomes waterlogged when the water table rises to an extent that the soil pores in the root zone of a crop become saturated, resulting in the restriction of the normal circulation of air, decline in the level of oxygen and increase in the level of carbon dioxide. Prolonged waterlogging results in secondary salinization, which in turn can influence soil salinity (Dwivedi 1997). Poor drainage can result in waterlogged soil, for example where there is a natural accumulation of water at foot slopes and valley bottoms; regions close to or adjacent to large open water surfaces; poor surface water management; water leaking from dams, pipes, canals or irrigation mainlines close to man-made obstructions (e.g. bridges); and over-irrigation.

It has been estimated that 18% of South Africa's irrigated land is either salt-affected or waterlogged (Backeberg et al. 1996). Although this proportion is relatively small compared to Argentina (34%), Egypt (33%), Iran (30%), Pakistan (26%) and the United States of America (23%) (Ghassemi, Jakeman & Nix 1995), only 13.7% of South Africa's land area is suitable for irrigation (Department of Agriculture, Forestry and Fisheries 2013) and proactive measures are therefore required to prevent further losses of this scarce resource.

Conventional methods for monitoring salt accumulation within irrigation schemes involve regular field visits to collect soil samples, followed by laboratory analyses. Many field visits are often required to effectively monitor large irrigation schemes. According to Nell and Van Niekerk (2014), salt-affected areas in South Africa are relatively small (often as narrow as 1–2 m), which further limits the viability of in situ methods. RS has been proposed as a less time-consuming and more cost-effective method for monitoring salt accumulation as satellite images cover large areas on a regular, timely basis (Abbas et al. 2013). According to Farifteh, Farshad and George (2006), there are two types of indicators that can be used for detecting salt-affected soils, namely soil-related and performance-related indicators. Soil-related indicators, or direct methods, include white salt crusts, puffy soil, dark greasy surfaces, dehydrated cracks and coarser topsoil, while performance-orientated indicators, or indirect methods, include spotty growth of crops, the presence of dead trees, blue-green tinge and moisture stress.

Several studies have investigated the spectral properties of saline soils. Rao et al. (1995) and Abbas and Khan (2007) found that salt-affected soils have higher reflectance values in the visible and NIR regions of the electromagnetic spectrum. This was confirmed by Metternicht and Zinck (2003) and Elnaggar and Noller (2010) who showed that salt-affected soils with visible surface salt encrustations are smoother than non-saline surfaces and cause high reflectance in the visible and the NIR regions of the spectrum. Farifteh, Farshad and George (2006) found that both the

colour and the surface roughness of salt-affected soils influence their spectral properties. However, increased moisture, ferric oxides and clay decreases reflectance and makes it difficult to identify salt-affected soils (Metternicht & Zinck 2003). Similar observations were made by Khan et al. (2005), Iqbal (2011), Setia et al. (2013) and Sidike, Zhao and Wen (2014). These findings led the development of several SIs calculated from image bands which have been shown to be effective in discriminating saline soils from unaffected soils (Fernandez-Buces et al. 2006; Abbas & Khan 2007; Abbas et al. 2013).

Most studies that have investigated the use of RS methods for detecting and monitoring salt-affected areas were carried out in areas where the cultivated fields are large, salt accumulation is severe and where the extent of affected areas are large enough to allow for the use of medium resolution imagery such as those acquired by Landsat (30 m) (Lenney et al. 1996; McFarlane, George & Caccetta 2004; Fernandez-Buces et al. 2006; Rodríguez, González & Zaballos 2007; Iqbal & Mehdi 2008; Abdelfattah, Shahid & Othman 2009; Elnaggar & Noller 2010; Aldakheel 2011; Mohamed, Morgun & Goma Bothina 2010; Iqbal 2011; Wang et al. 2013; Taghizadeh-Mehrjardi et al. 2014; Taghizadeh-Mehrjardi et al. 2016), IRS (20 m) (Dwivedi & Sreenivas 1998; Dwivedi et al. 2001; Khan et al. 2005; Abbas & Khan 2007; Abbas et al. 2013) or ASTER (15 m) (Gao & Liu 2008). VHR multispectral imagery (e.g. QuickBird, WV2) has been used to detect and map salt accumulation (Sidike, Zhao & Wen 2014; Setia et al. 2013; Douaoui & El Ghadiri 2015), but these studies did not take into account additional spatial features (e.g. texture measures) or applied ML classifiers to the feature datasets derived from the VHR imagery. Obstacles to also overcome in South African irrigation schemes is the relatively small size of irrigation fields (especially when the fields are elongated) and the occurrence of small patches of salt accumulation (Nell & Van Niekerk 2014). Medium resolution satellite imagery will therefore have little value in such cases. These obstacles were taken into account by Muller and Van Niekerk (2016a) and Muller & Van Niekerk (2016b), but these authors focused on indirect methods (e.g. vegetation stress monitoring) in mapping salt-accumulation. The aim of this study (which forms part of a larger research project (Commission 2011) was to evaluate the use of VHR WV2 imagery for detecting salt accumulation in highly dynamic irrigated fields where affected areas are relatively small in extent and where visible evidence of soil salinity (e.g. salt encrustations and precipitation) is often not present. The study evaluated both supervised and threshold-based classification approaches. Suitable thresholds were determined using three methods, namely 1) separability analysis; 2) RM; and 3) CART, while five supervised classification algorithms, namely 1) *k*NN; 2) MaxL; 3) SVM; 4) DT; and 5) RF were assessed. The WV2 panchromatic and multispectral bands were supplemented with several additional features including the first principal component,

texture measures and SIs. Soil analysis results of samples collected during field surveys were used for model building, classifier training and accuracy assessment.

This article is structured into four sections, the first of which provides an overview of the study area and methods used. This is followed by a description of the reflectance profiles of salt-affected and unaffected soils in the study area. The results of the separability analysis, RM and CART, as well as the performance of the supervised classifiers are discussed in the context of finding an operational solution for proactive salt accumulation monitoring in irrigation schemes. The paper concludes with a summary of the findings and suggestions for further research are made.

3.3 METHODS

3.3.1 Study area

The study area (Figure 3.1c) is a 100 km² section of the Vaalharts irrigation scheme (Figure 3.1b) located in the Northern Cape province of South Africa (Figure 3.1a), close to the small towns Hartswater, Pampierstad and Jan Kempdorp. The area extends from 24.7° to 24.8°E and 27.7° to 27.9°S and has an altitude ranging from 1064 to 1154 m above mean sea level. Vaalharts covers an area of 36 950 ha and has a semi-arid climate with cold winters and long, warm summers (Barnard et al. 2012). The mean annual rainfall of the scheme is 400 mm, most of which occurs during the summer months. The mean monthly rainfall from November to April is 47.3 mm (Schulze, Lynch & Maharaj 2006), while the mean maximum and minimum temperatures are 38.8°C and 4.4°C respectively. During winter months the mean monthly rainfall drops to 4.1 mm, with a mean maximum temperature of 31.8°C and a mean minimum temperature of -4.8°C (Schulze & Maharaj 2006).

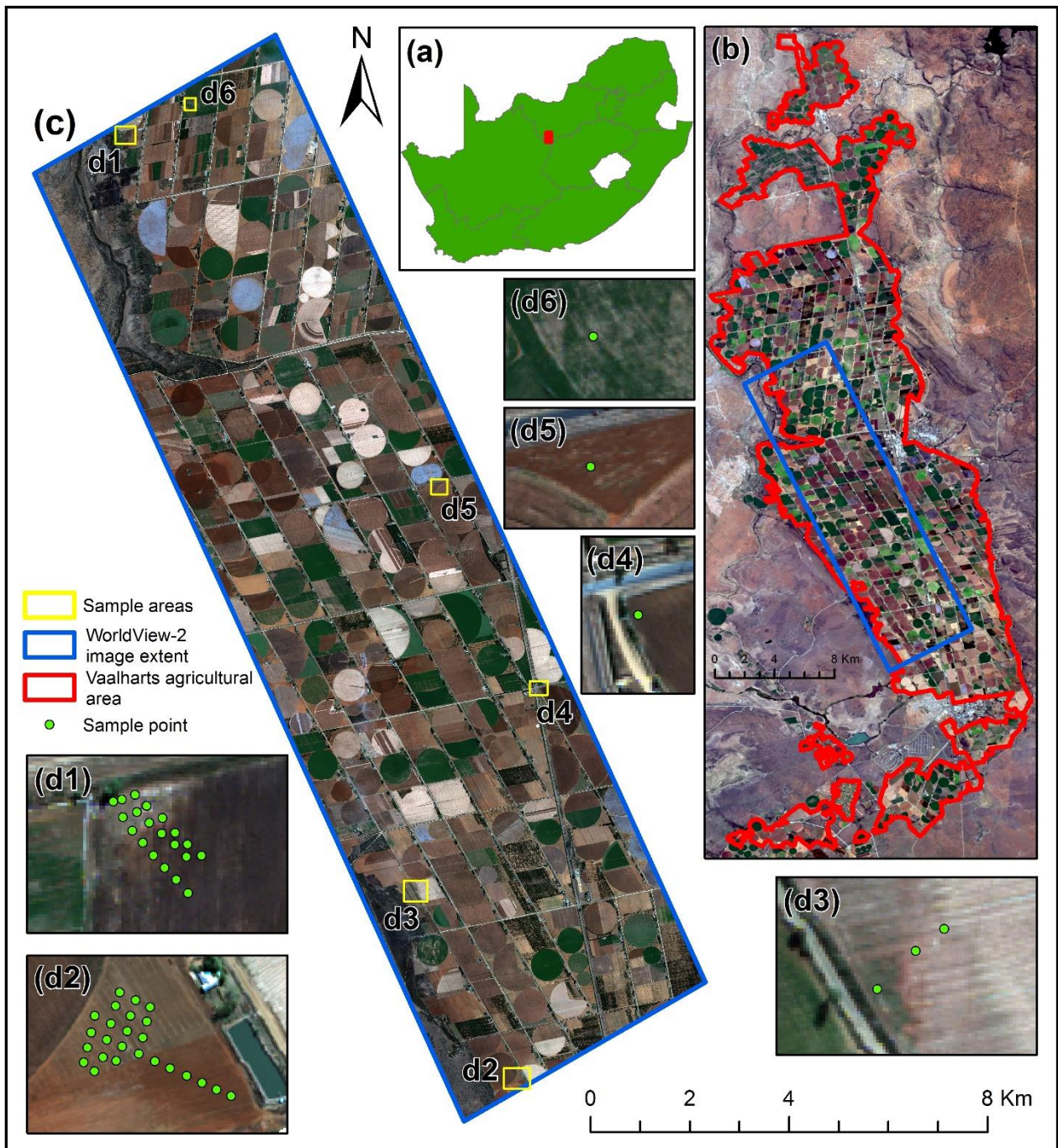


Figure 3.1: Location of the study area in South Africa (a) with the extent of the Vaalharts irrigation scheme (b) and the WorldView-2 image (c), as well as the distribution of sample points in the six collection sites (d1 to d6)

Vaalharts is known for its sandy soils and insufficient natural drainage, which often lead to waterlogging and salt accumulation (Maisela 2007). The dominant salts in the study area are Ca and Mg (HCO_3). Soils in the scheme typically consist of 8% clay, 2% silt, 68% fine sand and 22% medium and coarse sand (Streutker 1977). Maize, wheat, barley, lucerne and groundnuts are the main crops cultivated. Most of these crops are planted on a rotational basis (Maisela 2007; Kruger, Van Rensburg & Van den Bergh 2009).

3.3.2 Data collection and preparation

3.3.2.1 Satellite image collection and pre-processing

A WV2 image, captured on 23 May 2012, was acquired. The image has a spatial resolution of 0.50 m (0.46 m at nadir) for the panchromatic band and 2 m (1.84 m at nadir) for the multispectral bands (DigitalGlobe 2015). WV2 was chosen because it offered the highest combination of spatial and spectral resolution at the time. The sensor provides eight multispectral bands, namely coastal blue (CB) (400–450 nm), blue (450–510 nm), green (510–580 nm), yellow (585–625 nm), red (630–690 nm), RE (705–745 nm), NIR₁ (770–895 nm) and NIR₂ (860–1040 nm) (DigitalGlobe 2015). The acquisition date was chosen to coincide with the time of the year when most crops have been harvested and the majority of the fields are bare; therefore, when the proportion of exposed soils is maximized.

Twelve GCPs collected during the field survey and the 5 m resolution Stellenbosch University digital elevation model (SUDEM) (Van Niekerk 2012) were used to orthorectify the WV2 image. The ATCOR-2 model was used for radiometric and atmospheric corrections (Richter 2014). Mean elevation (1138.8 m) of the study area was calculated from the SUDEM and provided as input for the ATCOR-2 model. Rural and mid-latitude winter were respectively selected as the appropriate aerosol type and atmospheric condition. Adjacency correction was also performed to improve the quality of the atmospheric corrected WV2 image.

Vegetated areas were excluded from the analyses by using a NDVI threshold of 0.35. Man-made urban structures, such as roads and buildings, were also removed from the analysis by a digitized field mask of the irrigation scheme. All pre-processing operations were performed by making use of PCI Geomatica 2013 software.

3.3.2.2 Field surveys

A total of 51 in situ soil samples were collected from June to September 2012 using a clustered, random sampling scheme (Table 3.1). Soil samples were collected along transects or in regular grids in three sampling sites (Figure 3.1d1, Figure 3.1d2 and Figure 3.1d3). Individual samples were collected in the remaining three sample sites (Figure 3.1d4, Figure 3.1d5 and Figure 3.1d6). To improve the sampling efficiency, the sampling sites were selected to correspond to areas with visible evidence (e.g. precipitation) of salt accumulation. Samples were then collected in the immediate neighbourhood where no evidence of salt accumulation was apparent (Table 3.1). The samples were collected at a depth of 20 cm by means of a soil auger. A differential global positioning system (GPS) with accuracy of 10 cm was used to record the positions of each sample. Visible salt precipitation at each sample location was photographically recorded and qualified as

being either high, low or absent. The EC, which is a measure of how saline a soil sample is, was determined within a laboratory using the saturated paste technique (Committee 1991). Samples with EC measurements of less than 400 mS m⁻¹ were classified as non-saline, whereas samples with EC measurements equal to or greater than 400 mS m⁻¹ were grouped as saline in accordance with Nell and Van Niekerk (2014).

Table 3.1: Summary of sample site EC measurements and field notes

| Sample site | # of samples ^{a)} | | EC (mS m ⁻¹) | | | | Sample site field notes |
|-------------|----------------------------|----|--------------------------|---------|--------|--------------------|--|
| | SA | UA | Minimum | Maximum | Mean | Standard deviation | |
| d1 | 20 | 0 | 2100 | 9500 | 5405 | 2594.5 | Clear indication of salt precipitation on the soil surfaces; Waterlogging occurs between 45 and 70 cm at sample locations. |
| d2 | 7 | 18 | 19 | 1050 | 220 | 249.9 | Salt accumulation on the soil surfaces and within the subsoil at sample locations. |
| d3 | 2 | 1 | 150 | 7500 | 3716.7 | 3004.5 | Salt precipitation on the soil surfaces. |
| d4 | 0 | 1 | 90 | 90 | 90 | 0 | Outlet to drainage canal. |
| d5 | 1 | 0 | 4009 | 4009 | 4009 | 0 | Salt precipitation on the soil surfaces. |
| d6 | 1 | 0 | 800 | 800 | 800 | 0 | No signs of either salt accumulation or waterlogging. |

^{a)} SA refers to salt-affected and UA to unaffected

3.3.2.3 Feature set development

A feature set consisting of 69 input variables were considered for differentiating salt-affected from unaffected areas (Table 3.2). All of the WV2 bands and several SIs developed specifically for the direct detection of salt-affected soil (Khan et al. 2005; Fernandez-Buces et al. 2006; Abbas & Khan 2007; Iqbal 2011; Abbas et al. 2013; Setia et al. 2013; Sidike, Zhao & Wen 2014; Wang et al. 2013) were included in the feature set. They are:

$$1. S_1 = \text{Blue}/\text{Red}$$

Equation 3.1

$$2. S_2 = (\text{Blue} - \text{Red})/(\text{Blue} + \text{Red})$$

Equation 3.2

$$3. S_3 = (\text{Green} \times \text{Red})/\text{Blue}$$

Equation 3.3

$$4. S_4 = \sqrt{\text{Blue} \times \text{Red}}$$

Equation 3.4

$$5. S_5 = (\text{Blue} \times \text{Red})/\text{Green}$$

Equation 3.5

$$6. S_6 = (\text{Red} \times \text{NIR})/\text{Green}$$

Equation 3.6

$$7. \text{ Normalized difference salinity index (NDSI)} = (Red - NIR)/(Red + NIR)$$

$$8. \text{ Combined spectral response index (COSRI)} = ((Blue + Green)/(Red + NIR)) \times ((NIR - Red)/(NIR + Red))$$

Table 3.2: Considered features for analysis

| Type | | Features | # of features |
|-------------------------------------|-----------|---|---------------|
| Spectral features | Mean | Panchromatic, CB, blue, green, yellow, red, RE, NIR ₁ , NIR ₂ | 9 |
| Salinity indices | Mean | S ₁ × 4, S ₂ × 4, S ₃ × 4, S ₄ × 4, S ₅ × 4, S ₆ × 4, NDSI × 6, COSRI × 8 | 38 |
| Texture features (3×3; 5×5; 7×7) | GLCM | Contrast, entropy, homogeneity, variance | 21 |
| Image transformations | Histogram | Energy, entropy, variance | |
| | Mean | PC1 | 1 |

For the purposes of this study, the SIs were modified for WV2 imagery by alternating the blue or CB WV2 bands as the ‘blue’ variable, the yellow, red or RE WV2 bands as the ‘red’ variable and the NIR₁ or NIR₂ WV2 bands as the ‘NIR’ variable. Various permutations of these band combinations were applied to the indices to produce a total of 38 SIs.

A PCA was performed on the multispectral WV2 bands to condense most (96%) of the spectral variance into a single component (Campbell 2006). The resulting first principal component (PC1) was included in the feature set and used as input to the texture measures. Texture measures based on histogram statistics and second-order statistics computed from grey level co-occurrence matrices (GLCM) (Haralick, Shanmugam & Dinstein 1973; Clausi 2002) were included in the feature set. The histogram measures considered were energy, entropy and variance, while the GLCM measures were contrast, entropy, homogeneity and variance. Three window sizes, namely 3×3, 5×5 and 7×7 were used for generating the texture measures. Texture measures were also carried out on the panchromatic band and each of the multispectral bands. This combination of input variables allowed the texture calculations to be assessed at all possible spatial and spectral resolutions offered by the WV2 image. PCI Geomatica 2013 software was used to perform all the texture calculations.

3.3.2.4 Separability analysis

The JM distance measure, as implemented in the SEaTH (SEparability and THresholds) software package (Nussbaum, Niemeyer & Canty 2006), was used to score the features according to class separation. The algorithm firstly identifies features that have the best separability between classes, and then the threshold of separation for each feature is determined (Nussbaum, Niemeyer & Canty 2006; Gao et al. 2011; Heumann 2011). The JM distance is calculated as (Nussbaum, Niemeyer & Canty 2006):

$$J = 2(1 - e^{-B})$$

where J is the JM distance; and

B is the Bhattacharya distance.

The Bhattacharya distance (B) is the mean and standard deviation of the training samples of the two classes (Bhattacharyya 1943). The resulting J value ranges from 0 to 2, where $J = 0$ indicates that the two classes are completely correlated and therefore inseparable, while $J = 2$ indicates that the two classes are completely uncorrelated and separable. Lower values of J will consequently produce more classification errors (Nussbaum, Niemeyer & Canty 2006; Gao et al. 2011; Heumann 2011). According to Nussbaum, Niemeyer and Canty (2006), Heumann (2011) and Odindi and Mhangara (2013), a J value of 2 indicates excellent intra-class separation; a value equal to or greater than 1.9 good separation; and a value below 1.7 indicates poor separation. J values of less than 1 suggest a requirement for new training data (Nussbaum, Niemeyer & Canty 2006; Heumann 2011).

A limitation of the JM distance is the assumption that sample values within classes are normally distributed. In cases where this is not true, the threshold value might be substantially different, but the separability measure is still likely to be valid (Gao et al. 2011). A more detailed discussion on the JM distance can be found in Nussbaum, Niemeyer and Canty (2006).

Each of the features in Table 3.2 was included in the separability analysis. The scheme to which the analyses were applied is based on the quantitative soil EC measurements only and consists of a salt-affected ($EC \geq 400 \text{ mS m}^{-1}$) and an unaffected ($EC < 400 \text{ mS m}^{-1}$) class. The features which provided the highest class separation (J value) and the accompanying threshold values were used to generate salt accumulation maps.

3.3.2.5 Regression modelling

RM was used to analyse the statistical relationship between the measured soil EC and the spectral bands, SIs and texture measures. IBM SPSS v20.0 software was employed to generate a series of linear, logarithmic, inverse, quadratic, cubic, power and exponential models. Stepwise multiple regression and PLS regressions were also carried out on all 69 variables.

3.3.2.6 Classification and regression trees (CART)

CART (by Salford Systems) was applied to the full feature set (all 69 variables) to generate a DT, with each branch consisting of divisions (thresholds) to the most probable class (Lawrence & Wright 2001). In accordance with Campbell (2006) and Lawrence and Wright (2001), a pruning

step was applied on the resulting tree to guard against overfitting. This involved cross-validation during which the data is divided into subsets and results from some subsets are validated against results from other subsets.

3.3.2.7 Supervised classification

A pixel-based supervised classification approach was used to classify pixels of unknown identity using samples of known identity (Rees 2001; Campbell 2006). The classifiers considered were k NN, MaxL, SVM, DT and RF. The k NN algorithm assigns a class to a pixel according to the k -nearest trained pixels (Cover & Hart 1967; Gibson & Power 2000). The MaxL classifier makes use of training data to estimate the means and variances of each class (Harris 1987; Gibson & Power 2000) and determines the probability of an unknown pixel belonging to a particular class (Rees 2001; Albert 2002; Lillesand, Chipman & Kiefer 2008). SVM determines the optimal separating hyperplane between classes (Novack et al. 2011) by focussing on the training samples close to the edge (support vector) of the class descriptors (Tzotsos & Argialas 2006; Lizarazo 2008). A DT classifier identifies relationships between multiple response (dependent) variables and an independent variable. DTs hierarchically split a dataset into increasingly homogeneous subsets known as nodes (Pal & Mather 2003; Novack et al. 2011; Punia, Joshi & Porwal 2011; Gómez et al. 2012). The algorithm reaches a leaf node by recursively partitioning the feature data. When a leaf node is reached, the class associated with the node is assigned to the observation (Pal & Mather 2003). RF is an ensemble classifier based on DTs, where each DT is generated using a random vector sampled independently from the input vector. Each DT casts a vote (Leo Breiman 2001; Pal 2005; Bosch, Zisserman & Muñoz 2007) and contributes to the assignment of the most popular class to the independent variable (Leo Breiman 2001; Rodriguez-Galiano et al. 2012b). A more detailed discussion on the RF classifier can be found in Breiman (1996); Breiman (2001); Pal and Mather (2005); and Rodriguez-Galiano et al. (2012a).

OpenCV implementations of the k NN, SVM, DT and RF algorithms were used within eCognition 8.9 software (Bradski 2000), while chessboard segmentation (with a scale parameter of one pixel) was used to emulate a pixel-based approach and ENVI 5.0 to apply the MaxL classifier. A k value of one, three and five was used for the k NN classifications (Campbell 2006). The RBF was chosen as the kernel type for the SVM classifier, as recommended by Hsu, Chang and Lin (2010) and Li et al. (2010). The maximum number of trees for the RF classifier was set to 100. The number of active variables, which is the number of randomly selected features used to find the best splits at each node, was set to three (Rodriguez-Galiano et al. 2012a). Default parameters were used for the MaxL and DT classifiers.

3.3.2.8 Accuracy assessment

Maps were created from the rule-based (threshold-based) and supervised classification outputs to identify problem areas within the study area. An independent set of 20 soil samples was used to assess the accuracy of the maps. The root mean square error (RMSE) was calculated for the top-performing regression models (Eldeiry & Garcia 2009; Adhikari et al. 2013). Confusion matrices were generated to calculate the OA, producer's accuracy (PA), user's accuracy (UA), Kappa coefficient and the area under receiver operating characteristic (AUROC) curve (Evangelista 2006; Congalton & Green 2009).

3.4 RESULTS

The results of the soil analyses are shown in Figure 3.2. The majority (60.8%) of the samples were salt-affected. The 2:3 balance between salt-affected and unaffected samples was considered suitable for classifier training and accuracy assessment purposes.

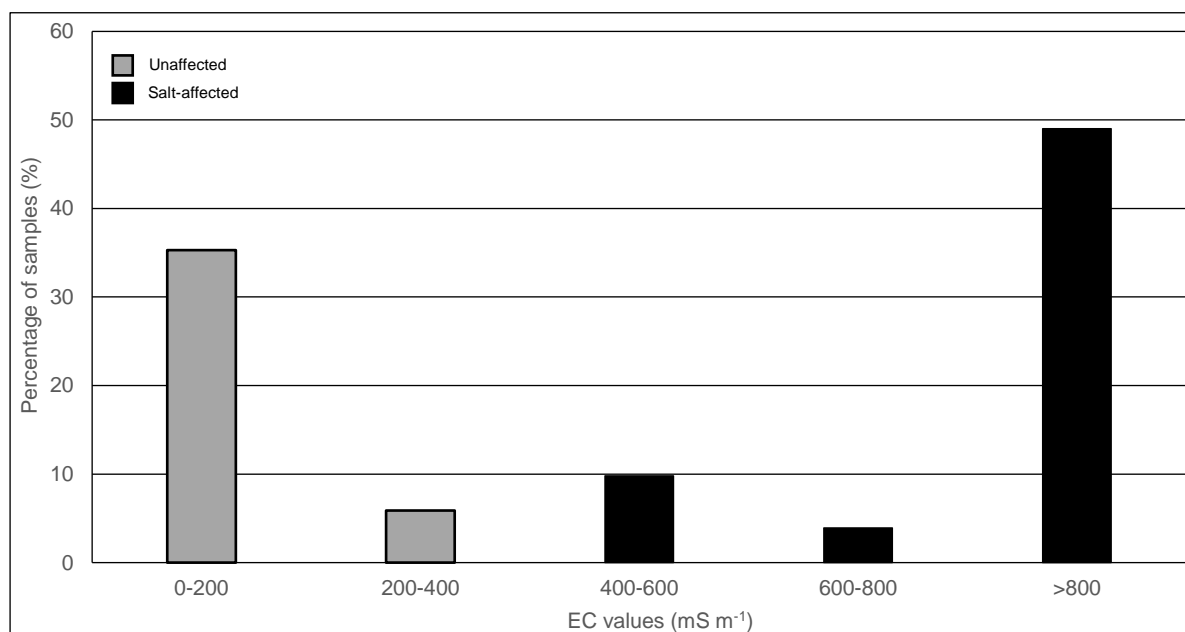


Figure 3.2: EC values of the collected soil samples, showing that there was a good balance between salt-affected and unaffected soil samples

Figure 3.3 shows photographic examples of sampled areas that were found to be salt-affected. In Figure 3.3a clear evidence of salt precipitation was present, while in Figure 3.3b very little evidence of salt precipitation was noticeable. In Figure 3.3c no salt precipitation was apparent, although some evidence of waterlogging was observed. These examples demonstrate that salt accumulation in the study area does not necessarily manifest in visible cues that can be easily exploited by using simple reflectance thresholds. Only eight (25%) of the salt-affected samples had clearly visible evidence of salt precipitation (Figure 3.3a). It was also observed that salt

accumulation is often concentrated in relatively small patches and salinity levels can vary substantially over very short (e.g. 2–5 m) distances.

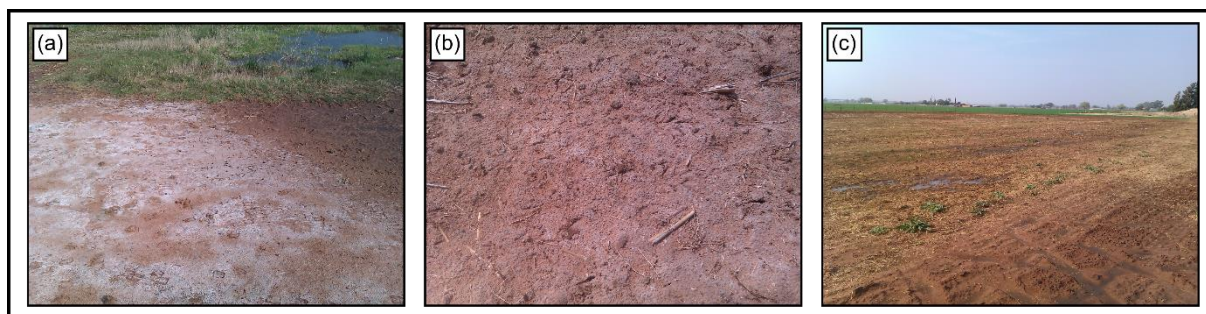


Figure 3.3: Examples of salt-affected soils in the study area. Clear evidence of salt precipitation is visible in (a), with less precipitation visible in (b). In (c) no salt precipitation is visible, but indications of waterlogging are observed.

3.4.1 Spectral profiles and separability analysis results

Figure 3.4 compares the reflectance of salt-affected and unaffected soils in each of the WV2 bands. The spectral properties of salt-affected and unaffected soils are very similar in the CB and blue bands, with more noticeable differences in the remaining bands. In contrast to Rao et al. (1995), Metternicht and Zinck (2003), Abbas and Khan (2007) and Elnaggar and Noller (2009), salt-affected soils had lower reflectance values in the longer wavelengths (510–690 nm) of the visible spectrum. The standard deviation error bars in Figure 3.4 show that there is substantial overlap between the recorded reflectance values. This was confirmed when separability was quantified using SEaTH. The highest JM value (0.38) achieved was in the yellow band, which indicates that the classes are not separable when individual bands are used. The large overlap between the different classes was attributed to the inconsistencies in salt precipitation and other visible clues of salt accumulation that were observed during the field visits.

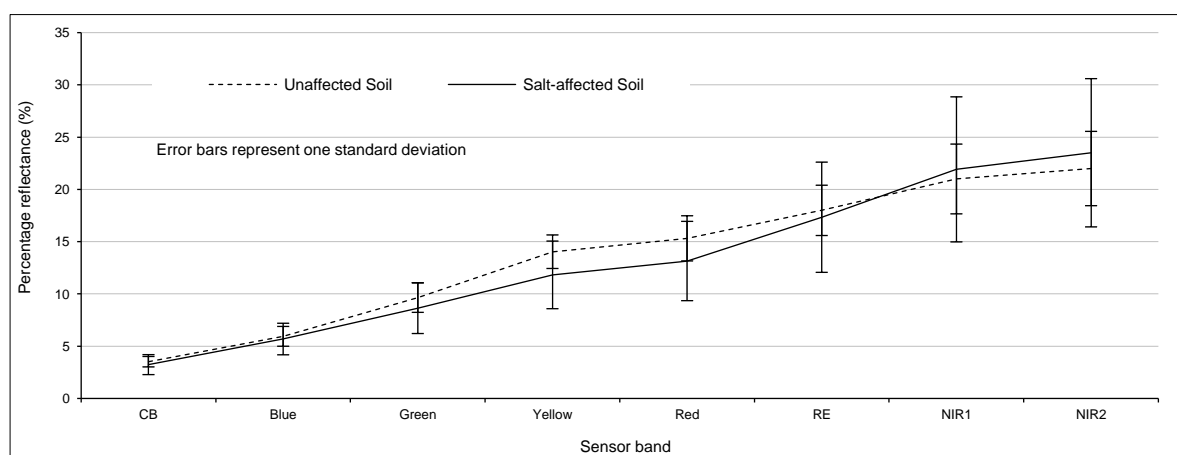


Figure 3.4: Spectral profile of salt-affected and unaffected samples as extracted from the WorldView-2 image

Better separability was achieved when multiple bands were combined as SIs. Of all the SIs evaluated, NDSI (using the red and NIR₁ bands as input) produced the highest separability between

the salt-affected and unaffected classes, with a J value of 0.91 and a threshold of -0.19. This threshold was implemented to produce a thematic map of salt-affected and unaffected areas (see Section 3.4.3).

3.4.2 Regression modelling and DT analysis

Table 3.3 shows the results of the RM of EC measurements and the individual WV2 image bands, SIs and texture measures. For the sake of brevity, only features that achieved an R^2 of 0.4 or more in any of the models are included in the table. None of the WV2 bands or texture measures met this requirement. The best fit was achieved by NDSI (using the yellow and NIR₁ bands as input) ($R^2 = 0.64$, $p < 0.001$, $RMSE = 2498.3 \text{ mS m}^{-1}$), with the cubic model providing the best description of this relationship. The NDSI had been successfully employed in several studies (Khan et al. 2005; Iqbal 2011).

Table 3.3: Results of regression analyses used to determine the relationship between EC and WorldView-2 features

| Salinity index | Band combination | Regression model (R^2) ^{a)} | | | | | | |
|----------------|-----------------------------|--|-------------|---------|-----------|-------------|-------|-------------|
| | | Linear | Logarithmic | Inverse | Quadratic | Cubic | Power | Exponential |
| NDSI | Yellow; NIR ₁ | 0.26 | - | 0.27 | 0.47 | 0.64 | - | 0.34 |
| NDSI | Yellow; NIR ₂ | 0.23 | - | 0.30 | 0.45 | 0.49 | - | 0.34 |
| NDSI | Red; NIR ₁ | 0.18* | - | 0.39 | 0.56 | 0.56 | - | 0.25 |
| NDSI | Red; NIR ₂ | 0.16* | - | 0.27 | 0.41 | 0.41 | - | 0.25 |
| COSRI | CB; red; NIR ₁ | 0.19 | 0.28 | 0.33 | 0.43 | 0.43 | 0.38 | 0.28 |
| COSRI | CB; red; NIR ₂ | 0.23 | 0.30 | 0.33 | 0.42 | 0.43 | 0.41 | 0.33 |
| COSRI | CB; RE; NIR ₁ | 0.24 | 0.31 | 0.34 | 0.44 | 0.51 | 0.41 | 0.32 |
| COSRI | CB; RE; NIR ₂ | 0.27 | 0.32 | 0.35 | 0.42 | 0.48 | 0.43 | 0.37 |
| COSRI | Blue; red; NIR ₁ | 0.19 | 0.29 | 0.34 | 0.43 | 0.43 | 0.40 | 0.28 |
| COSRI | Blue; RE; NIR ₁ | 0.22 | 0.30 | 0.34 | 0.43 | 0.43 | 0.42 | 0.33 |
| COSRI | Blue; RE; NIR ₂ | 0.24 | 0.32 | 0.35 | 0.46 | 0.49 | 0.42 | 0.33 |
| COSRI | Blue; red; NIR ₂ | 0.27 | 0.33 | 0.35 | 0.44 | 0.47 | 0.44 | 0.37 |

^{a)} All results were significant at a 0.001 level, except for those indicated with * (0.01 level)

The results from the stepwise regression analyses showed that the NIR₂ band was the first variable to be taken into account ($R^2 = 0.39$, $p < 0.001$), followed by COSRI (blue, red and NIR₂) and COSRI (CB, red and NIR₁). The resulting model produced a R^2 of 0.51 ($p < 0.001$). The best PLS regression model had a goodness-of-fit of 0.39 (R^2) and took 38 variables into account.

Figure 3.5 compares this model to the calculated NDSI and measured soil EC (mS m^{-1}) values. Two outliers (labelled A and B in Figure 3.5) were identified and removed, resulting in a slight improvement in the goodness-of-fit ($R^2 = 0.68$, $p < 0.001$) of the model.

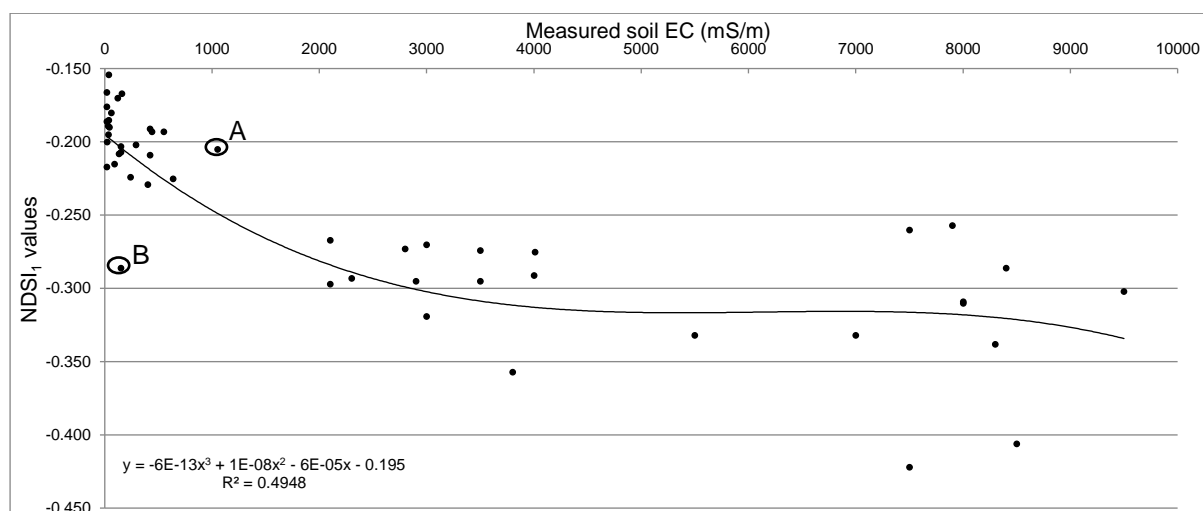


Figure 3.5: Relationship between NDSI (red and NIR₁) and measured soil EC. Two outliers (A and B) were identified and removed.

A threshold value of 400 mS m⁻¹ was applied to the regression model to produce a classification of salt-affected (< 400 mS m⁻¹) and unaffected (≥ 400 mS m⁻¹) areas and a map was produced (see Section 3.4.3). The CART analysis identified a single feature – NDSI (using yellow and NIR₁ as input variables) – as primary splitter. Salt-affected (< 400 mS m⁻¹) samples were associated with NDSI values of less than -0.22. This threshold was applied on the NDSI to produce a thematic map of salt-affected areas.

3.4.3 Classification accuracy results

The thematic maps obtained from implementing the thresholds of the RM and CART analysis were supplemented with a series of maps generated by the supervised classifiers. The accuracies of the resulting maps were assessed using an independent set of samples. Table 3.4 provides a summary of the accuracies achieved.

Table 3.4: Summary of salt-affected and unaffected classification accuracies

| Method | Approach | Class | Producer's accuracy (%) | User's accuracy (%) | Overall accuracy (%) | Kappa | AUROC ^{a)} |
|----------------------------|------------|---------------|-------------------------|---------------------|----------------------|-------------|---------------------|
| SEaTH (NDSI) | Threshold | Salt-affected | 66.7 | 88.9 | 75 | 0.51 | 0.76* |
| | | Unaffected | 87.5 | 63.6 | | | |
| Regression analysis (NDSI) | Threshold | Salt-affected | 83.3 | 76.9 | 75 | 0.47 | 0.74* |
| | | Unaffected | 62.5 | 71.4 | | | |
| CART (NDSI) | Threshold | Salt-affected | 75 | 90 | 80 | 0.60 | 0.8* |
| | | Unaffected | 87.5 | 70 | | | |
| kNN (k = 3) | Classifier | Salt-affected | 84.6 | 91.7 | 80 | 0.58 | 0.79* |
| | | Unaffected | 85.7 | 75 | | | |
| DT | Classifier | Salt-affected | 66.7 | 88.9 | 75 | 0.51 | 0.76* |
| | | Unaffected | 87.5 | 63.6 | | | |
| RF | Classifier | Salt-affected | 83.3 | 83.3 | 80 | 0.58 | 0.79* |
| | | Unaffected | 75 | 75 | | | |
| SVM | Classifier | Salt-affected | 100 | 60 | 60 | 0 | 0 |
| | | Unaffected | 0 | 0 | | | |
| MaxL | Classifier | Salt-affected | 83.3 | 71.4 | 70 | 0.35 | 0.69* |
| | | Unaffected | 50 | 50 | | | |

^{a)} AUROC results significant at a 0.05 level (*)

The -0.22 NDSI (yellow and NIR₁) threshold identified by CART produced the most accurate classification with an OA of 80%, Kappa of 0.6 and AUROC of 0.8. The salt-affected class recorded a very high UA (90%), but the PA was lower (75%). The accuracies of the thematic maps generated by the *k*NN (with *k* = 3 producing the best results) and RF supervised classifiers were only marginally lower, with both achieving an OA of 80%, Kappa of 0.58 and AUROC of 0.79.

The accuracies of the maps produced using the regression analysis and SEaTH thresholds were on par with the supervised DT classifier, with OAs of 75%. MaxL achieved an OA of 70%, but the low Kappa (0.35) suggests high agreement by chance (Garrett & Viera 2005; Evangelista 2006; Johnson, Chawla & Hellmann 2012). The worst-performing classifier was SVM, which achieved an OA of only 60% and a very low Kappa (0) and AUROC (0).

Figure 3.6 shows the thematic maps produced from the various classifications. Twenty-seven percent of the study area was covered by vegetation and was excluded from the maps (shown in white). At a glance it seems that there is substantial variation between the different outputs, with some of the models, in particular MaxL (Figure 3.6g) and SVM (Figure 3.6h), severely overestimating salt-affected areas. Based on previous research (Khan et al. 2005; Iqbal 2011), NDSI (red and NIR₁) using a threshold of -0.23 (Figure 3.6a) seems to be the most realistic representation of salt accumulation in the study area. The maps produced from the NDSI (yellow and NIR₁) cubic regression model (Figure 3.6b) and CART analysis (Figure 3.6c) is almost identical as NDSI (yellow and NIR₁) is used in both cases. Only small differences are evident in the maps produced by the *k*NN (Figure 3.6d) and DT (Figure 3.6e) supervised classifiers, while RF (Figure 3.6f) classified fewer fields as salt-affected.

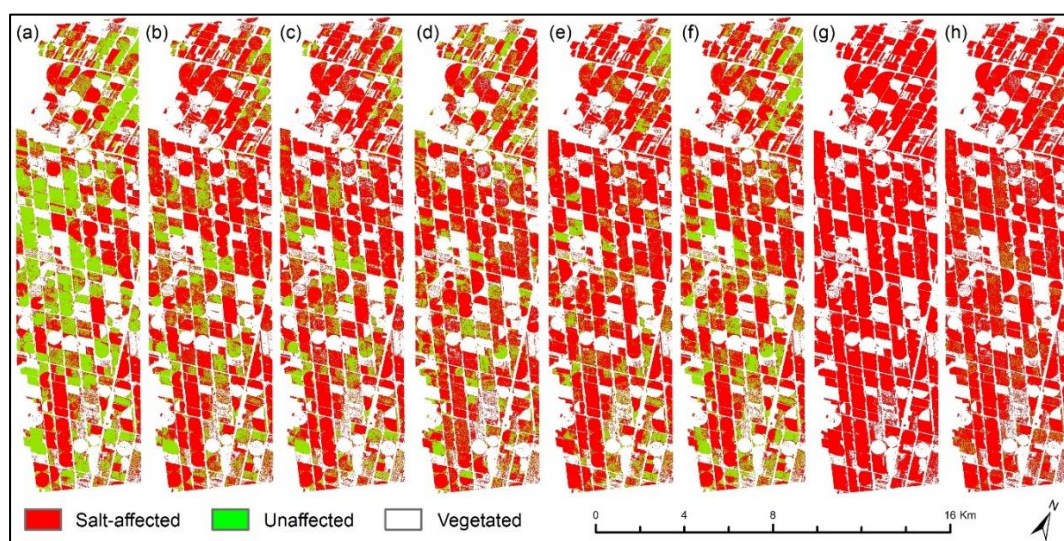


Figure 3.6: Produced maps from the ruleset-based and supervised classifications, namely (a) NDSI (red and NIR₁) SEaTH threshold, (b) NDSI (yellow and NIR₁) cubic regression model, (c) NDSI (yellow and NIR₁) CART threshold, (d) *k*NN (*k* = 3), (e) DT, (f) RF, (g) SVM and (h) MaxL

3.5 DISCUSSION

Notable differences in the spectral properties of salt-affected and unaffected soils were recorded in the green, yellow, red, RE, NIR₁ and NIR₂ bands (Figure 3.4), but in contrast to the findings of Rao et al. (1995), Metternicht and Zinck (2003) and Elnaggar and Noller (2010), salt-affected soils generally had a lower reflectance in the visible region of the electromagnetic spectrum. This discrepancy is attributed to the relatively low levels of salt precipitation occurring in the study area. Soils with salt precipitation have high reflectance values in the visible and NIR regions of the electromagnetic spectrum (Rao et al. 1995; Metternicht & Zinck 2003; Elnaggar & Noller 2010), but in this study only 25% of the samples representing salt-affected soils had sufficiently high levels of salt precipitation for it to be noticeable. In most cases salt-affected soils appeared smooth and dark, most likely because salt accumulation in the study area often coincides with waterlogging (i.e. secondary salinization) and the reflection of wet soils are generally lower in the visible and NIR spectra (Metternicht & Zinck 2003). It is noteworthy that, even in the absence of visible cues, relatively good classification accuracies were obtained. Clearly the non-visible bands (e.g. RE, NIR₁, NIR₂) must have contributed to the separation of the two classes.

NDSI (using the yellow and NIR₁ bands) produced a regression model with a moderately strong fit ($R^2 = 0.64$, $p < 0.001$, $RMSE = 2498.3 \text{ mS m}^{-1}$), although the OA of the resulting model was relatively low (75%) compared to some of the other classifiers. When plotted (see Figure 3.5) it was observed that the relationship between NDSI and EC is erratic when salinity levels are high and that the model generally overestimated EC. PLS regression reduces a large number of measured collinear spectral variables to a few non-correlated latent variables (Hansen & Schjoerring 2003; Cho et al. 2007; Mashimbye et al. 2012), but in contrast to Mashimbye et al. (2012) PLS (38 latent variables) produced a weak model ($R^2 = 0.39$) compared to the cubic regression model based on the NDSI.

From the results it seems that most of the classifications overestimated salt accumulation. The way in which field samples were collected may have influenced the results, as areas where salt accumulation is likely to occur were targeted. Although samples were also systematically collected outside targeted areas (where no evidence of salt accumulation was apparent), most (63%) of the soil samples collected were salt-affected. This caused a slight bias towards salt-affected training and reference data, which may have had a negative effect on the classifications. The relatively high overall accuracies (80%) of the *k*NN and RF classifiers are partly attributed to their insensitivity to imbalanced datasets. The *k*NN classifier only considers the closest known values for classification purposes and RF uses bagging to overcome some of the limitations of other classifiers (Leo Breiman 2001; Johnson, Chawla & Hellmann 2012). Another likely reason for the

relatively good performance of RF is the relatively small sample set (51) and the large (69) number of features considered. RF has been shown to perform well under such conditions (Breiman 1996; Rodriguez-Galiano et al. 2012a). In contrast to Lizarazo (2008), Li et al. (2010), Petropoulos, Kalaitzidis and Prasad Vadrevu (2012) and Myburgh and Van Niekerk (2013), SVM produced low accuracies. Efforts to improve the accuracy of the SVM classifier by tuning the input parameters were unsuccessful. MaxL also showed poor accuracies, most likely due to its sensitivity to large input feature sets (Myburgh & Van Niekerk 2013).

A factor that complicated the detection of salt accumulation in this study was the disturbance caused by soil preparations (e.g. ploughing). Vaalharts is a highly dynamic irrigation scheme in which crops are rotated throughout the year. Many of the fields visited during the survey were recently ploughed in preparation for planting. This altered the soil surface (and reflectance) and would have had a negative effect on classification accuracies. Also, even though the image acquisition date was specifically selected at a time of the year when most of the crops have been harvested, only 73% of the study area was bare at the time. The efficiency of targeting the spectral properties of bare soils (i.e. direct approach) for operational salt accumulation detection was thereby reduced, especially since costly imagery needs to be acquired over large areas.

It was observed that salt accumulation was often concentrated in small patches and that salinity levels varied substantially over very short distances (e.g. 2–5 m) (see Figure 3.3). In many cases the spatial resolution of the WV2 imagery was sufficiently high to detect such variations, but some salt-affected areas were depicted as unrealistically large, continuous areas (see Figure 3.6). This overestimation of salt accumulation will likely be amplified when lower resolution imagery (e.g. Landsat 8, SPOT-5) is used. More work is needed to investigate the impact of spatial resolution on mapping small patches of salt-affected areas.

The spectral resolution of the WV2 sensor is higher than most other VHR sensors, but is limited to the visible and NIR region of the electromagnetic spectrum. Using hyperspectral data on South African soils, Mashimbye et al. (2012) found that the 2257 nm band in the SWIR region of the electromagnetic spectrum showed the strongest correlation to salt-affected soils. The addition of a SWIR (1195–2365 nm) band to the recently-launched WorldView-3 sensor consequently holds great potential for monitoring salt accumulation with multispectral imagery.

3.6 CONCLUSIONS

This study evaluated the use of VHR WV2 imagery for modelling and mapping salt accumulation by observing bare soils. In addition to the WV2 image bands, the first principal component, a number of texture measures and several SIs were also considered as possible predictor variables.

Three threshold classifications based respectively on RM, the JM separability measure and CART, as well as five supervised classifiers (kNN, MaxL, SVM, DT and RF) were evaluated. The results demonstrated that a threshold determined by CART analysis was the most accurate in differentiating salt-affected and unaffected soils, but that the accuracy of the kNN and RF classifications were only marginally lower. Overall, NDSI (yellow and NIR₁) was the best predictor of salt accumulation as it featured in the separability analysis, RM and CART.

We conclude that the use of WV2 imagery to identify salt-affected soils can produce good classification accuracies. The models, however, tended to overestimate salt accumulation and large variations between the results from the different classifications were noted. The inconsistencies in the visual appearance of salt-affected soils are the most likely reason for misclassifications. Temporal factors, such as soil preparation (e.g. ploughing) and the impact of water (e.g. rainfall, irrigation) will likely have a negative impact on the classification accuracies. Small patches of vegetation, the soil mineralogy and whether the soils are waterlogged will also influence the visual appearance of salt-affected soils. Salt-affected soils were also found to mostly occur in small patches and vary over short distances, making it difficult to accurately map. Subsurface conditions are also not considered in this approach.

VHR imagery capable of recording radiation in the SWIR region of the electromagnetic spectrum (e.g. WorldView-3) might produce better results, but it is unlikely that it will overcome all of the limitations of the direct approach (i.e. detecting salt accumulation by observing bare soils). Indirect detection methods (e.g. vegetation stress monitoring, hydrological modelling) that take subsurface conditions into consideration might produce better results. Ideally a combination of direct and indirect methods should be used. Clearly, more research is needed before such methods can be operationalized for detecting and monitoring salt accumulation in irrigated areas.

CHAPTER 4: MACHINE LEARNING PERFORMANCE FOR PREDICTING SOIL SALINITY USING DIFFERENT COMBINATIONS OF GEOMORPHOMETRIC COVARIATES*

4.1 ABSTRACT

Conventional methods of monitoring salt accumulation in irrigation schemes require regular field visits to collect soil samples for laboratory analysis. Identifying areas prone to salt accumulation by means of geomorphometry (i.e. terrain analyses using DEMs) can potentially save time and costs. This study evaluated the extent to which DEM derivatives and ML algorithms (kNN, SVM, DT and RF) can be used for predicting the location and extent of salt-affected areas within the Vaalharts and Breede River irrigation schemes of South Africa. In accordance with local management policies, salt-affected areas were defined as regions with soil electrical conductivity (EC) values greater than 4 dS/m. Two DEMs, namely the one-arch second SRTM DEM and a photogrammetrically-extracted digital surface model (DSM), were used for creating the derivatives. Wetness indices as well as hydrological and morphometric terrain analysis techniques were used to generate predictive variables. For comparative purposes, the predictive variables were also used as input to regression modelling and geostatistics, namely kriging with external drift (KED). Thresholds were applied to the regression models and KED results to obtain a binary classification. EC values based on in situ soil samples were used for model development, classifier training and accuracy assessment.

The results show that KED achieved the highest overall accuracy (OA) in Vaalharts (79.6%), whereas KED and ML (DT) showed the most promise in the Breede River (75%). The findings suggest that the use of elevation data and its derivatives as input to geostatistics and ML holds much potential for monitoring salt accumulation in irrigated areas, particularly for simulating subsurface conditions. More work is needed to investigate the potential of using ML and DEM derivatives, along with other geospatial datasets such as satellite imagery (that have been shown to be effective for monitoring surface conditions), for the operational modelling of salt accumulation in large irrigation schemes.

*This chapter was published by Geoderma in Volume 299 (Vermeulen & Van Niekerk 2017) and consequently conforms to the prescribed structure of that journal. Some duplication between the content of this chapter and other chapters (especially Chapters 2 and 3) can also be expected.

4.2 INTRODUCTION

Salinity is a term used to describe the amount of salt in soil or water (Mcghie 2005). For the purpose of this study, salinity refers to the accumulation of soluble salts in the soil due to natural processes or human activities (Al-Khaier 2003). The way in which salts move and accumulate in soils can be affected by poor drainage (waterlogging), irrigation practices, clearance of vegetation and the reshaping of the landscape through earth works (Mcghie 2005). In large quantities, salts limit the normal growth of plants. This and other negative impacts of salt accumulation on crop production is a global concern (Metternicht & Zinck 2003).

An estimated 18% of the soils in South African irrigation schemes is salt-affected or waterlogged (Backeberg et al. 1996). Although this percentage is relatively small compared to Argentina (34%), Egypt (33%), Iran (30%), Pakistan (26%) and the United States of America (23%) (Ghassemi, Jakeman & Nix 1995), only 13.7% of South Africa's land area is suitable for irrigated agriculture (Department of Agriculture, Forestry and Fisheries 2013). Proactive measures to reduce the effect of salt accumulation are therefore needed to prevent loss of productive agricultural land. Preventative measures include careful consideration of crop water requirements and irrigation water quality, as well as frequent monitoring of salt levels in soils (Shainberg & Shalhevet 1984).

Conventional methods of monitoring salt-affected soils require regular field visits and laboratory analyses, which are often not viable for frequent monitoring of large areas. Although there has been an increase in the use of proximal (in situ) sensors (Viscarra Rossel et al. 2011), such instruments normally monitor soil conditions within relatively small ranges (within 2 m). This necessitates the incorporation of a large number of sensors to effectively monitor extensive areas at the required (i.e. within field) spatial resolutions. Owing to its ability to observe large areas on a regular, timely basis, remote sensing has also been used as an alternative method for monitoring salt accumulation (Abbas et al. 2013; Akramkhanov et al. 2011; Dwivedi 1997; Dwivedi et al. 1999; Elnaggar & Noller 2010; Sulebak et al. 2000). However, a major drawback of using remotely sensed imagery is its inability to effectively monitor subsurface processes that do not directly influence the spectral responses of the topsoil (Vermeulen & Van Niekerk 2016).

The use of geomorphometry – terrain analysis using digital elevation data (Pike 2000) – to model areas that are susceptible to salt accumulation has produced good results. Elnaggar and Noller (2010) found a significant correlation between soil EC, and elevation, slope and wetness indices. Similarly, Sulebak et al. (2000) identified a strong, significant correlation ($R^2 = 0.8$) between terrain data (slope, aspect and profile curvature) and soil moisture using a stepwise RM approach. Sulebak et al. (2000) observed that low slope gradients were associated with high soil wetness values and Akramkhanov et al. (2011) found significant correlations (as determined by stepwise

multiple regression) between soil EC and environmental factors such as distance to drainage, profile curvature, slope and groundwater table depth. Taghizadeh-mehrjardi et al. (2016) found wetness indices, the multi-resolution valley bottom flatness index and elevation to be the most important predictors of soil salinity.

Geostatistics have been used widely in salt accumulation studies (Gallichand et al. 1992; Utset et al. 1998; Li et al. 2007; Eldeiry & Garcia 2008; Eldeiry & Garcia 2009; Juan et al. 2011; Taghizadeh-Mehrjardi et al. 2014), particularly for interpolating salt accumulation from soil sample analysis results. Kriging, a generic term used to refer to a group of generalized least squares regression algorithms, has been shown to produce good results, as it provides linear unbiased estimates and weights surrounding sample points to account for clustering (Hengl, Heuvelink & Rossiter 2007; Gallichand et al. 1992). Several variations of the kriging algorithm are available, but co-kriging (CK), universal kriging (UK), regression-kriging (RK) and KED seem to be the most popular for salt accumulation modelling (Gallichand et al. 1992; Bishop & McBratney 2001; Baxter & Oliver 2005; Li et al. 2007; Eldeiry & Garcia 2008; Motaghian & Mohammadi 2011; Taghizadeh-Mehrjardi et al. 2014).

CK, the simplest of these algorithms, is a multivariate extension of kriging that allows for the incorporation of auxiliary data to improve predictive capacity (Wackernagel 2010). CK is suitable when only a few auxiliary variables are being considered and when these variables do not cover all sample locations (Hengl, Heuvelink & Stein 2003). UK, RK and KED are mathematically equivalent algorithms that make use of auxiliary variables to compute the kriging trend model (Pebesma 2006). UK models the trend using coordinates only, whereas KED makes use of other auxiliary variables for estimating the trend function. RK calculates the drift and residuals separately, after which the results are summed (Hengl, Heuvelink & Rossiter 2007). Gallichand et al. (1992) found CK to produce better EC models compared to moving average methods, while Eldeiry and Garcia (2008) observed that RK produced a stronger model compared to those generated with RM. Performing RK, Taghizadeh-Mehrjardi et al. (2014) observed a moderate significant correlation ($R^2 = 0.49$) between soil EC and the evaluated variables, with wetness indices, geomorphological surfaces (rock outcrops), principal components, catchment aspect and valley depth being the main predictors. Li et al. (2007) showed that CK and RK produced better results than ordinary kriging (OK), emphasising the importance of incorporating ancillary data (e.g. terrain analysis derivatives) in the interpolation of EC. Comparing OK, RK and KED, Bishop and McBratney (2001) found KED to be the best predictor of soil EC, while Motaghian and Mohammadi (2011) demonstrated that KED produced more accurate results in modelling soil saturated hydraulic conductivity than RM, OK, CK and RK. Similarly, Baxter and Oliver (2005)

found that KED produced superior results (compared to CK and RK) in predicting potentially available nitrogen within agricultural fields.

In contrast to geostatistical methods, ML algorithms use samples of known identity (categories) to classify instances of unknown identity (Rees 2001; Campbell 2006). Various ML algorithms, including *k*NN (Nemes et al. 1999; Nemes, Rawls & Pachepsky 2006; Coopersmith et al. 2014), artificial neural networks (Behrens et al. 2005; Aitkenhead et al. 2012), SVM (Kovacevic, Bajat & Gajic 2010; Li, Im & Beier 2013), DT (Bui & Moran 2001; Jafari et al. 2014) and RF (Heung, Bulmer & Schmidt 2014), accompanied by auxiliary variables, have been employed to predict soil properties and classes. Evans, Caccetta and Ferdowsian (1996) produced reasonable accuracies (> 60%) for mapping saline soils with DTs. Similar observations were made by Evans, Ferdowsian and Campbell (1996). Also employing DTs for salt accumulation mapping, Elnaggar and Noller (2010) achieved very accurate results (60% and 98.8% for unaffected and salt-affected soils respectively) and attributed it to the algorithm's ability to incorporate a large number of disparate predictors in the model building process. DTs are, however, prone to overfitting (i.e. producing models that perform well on the training data, but poorly on general untrained data), while more powerful machine learning algorithms such as SVM and RF have been shown to be more robust (Rodriguez-Galiano et al. 2012a; Rodriguez-Galiano et al. 2012b; Myburgh & Van Niekerk 2014).

Although much work has been done on combining ML algorithms and remotely sensed imagery for mapping salt-affected areas (Abbas et al. 2013; Abbas & Khan 2007; Abood, Maclean & Falkowski 2011; Dwivedi & Sreenivas 1998; Elnaggar & Noller 2010; Muller & Van Niekerk 2016a; Vermeulen & Van Niekerk 2016), such data can only observe surface conditions. The use of DEMs (and its derivatives) as input to ML algorithms delineating salt-affected areas is of particular interest, as it would better represent subsurface conditions. However, we are not aware of any published studies in which ML algorithms were compared to other established methods (e.g. geostatistics) when only terrain variables were used as input. In addition, very little information is available on the impact of DEM properties on salt accumulation modelling.

This study aims to evaluate the use of several ML algorithms (*k*NN, SVM, DTs and RFs) for identifying areas in irrigated fields that are salt-affected. The main purpose is to determine the effectiveness with which these methods can produce simple binary maps of salt-affected and unaffected areas so that they can be used as a scoping mechanism to prioritize more detailed (in situ) investigations and to discard unaffected areas from further consideration. The results are compared to binary classifications applied to models generated by two established methods, namely RM and KED. The Vaalharts and Breede River irrigation schemes in South Africa (Figure 4.1 and Figure 4.2) were chosen as study sites. The landscapes of the two areas are very different,

with Vaalharts mostly consisting of flat terrain, while Breede River is located in a mountainous region. This allowed for a better comparison and evaluation of the techniques.

4.3 MATERIALS AND METHODS

4.3.1 Study areas

The Vaalharts irrigation scheme (Figure 4.1) is located in the Northern Cape Province of South Africa in the Harts River valley, close to the small towns of Hartswater and Jan Kempdorp. The irrigation scheme's altitude ranges from 1 064 m to 1 154 m above mean sea level and it covers an area of 36 950 ha. Vaalharts is known for its semi-arid climate, mean annual rainfall of 400 mm (Schulze, Lynch & Maharaj 2006), cold winters and long warm summers (Barnard et al. 2012). Most rain occurs during the summer months (November to April) when the mean monthly rainfall is 47.3 mm and the mean minimum and maximum temperatures are 4.4°C and 38.8°C respectively. During the winter months, the mean monthly rainfall drops to 4.1 mm and the mean minimum and maximum temperatures are -4.8°C and 31.8°C respectively (Schulze & Maharaj 2006).

The Vaalharts irrigation scheme mostly consists of sandy soils, but is prone to waterlogging and salt accumulation due to insufficient natural drainage (Maisela 2007). The dominant salts in the study area are Ca and Mg (HCO_3). Soils in the scheme typically consist of 8% clay, 2% silt, 68% fine sand and 22% medium and coarse sand (Streutker 1977). Maize, wheat, barley, lucerne and groundnuts are the main crops in the area (Kruger, Van Rensburg & Van den Berg 2009) and are mostly planted on a rotational basis (Maisela 2007).

Sloping towards the south, the Harts River valley is bordered by two plateaus, one to the east and one to the west. Due to the low gradient of the Harts River and an absence of incisions by the river (Gombar & Erasmus 1976; Barnard et al. 2012), the valley has an unvarying topography (Figure 4.1). Vaalharts consists of the Archaean Ventersdorp Supergroup and older basement rocks composed of Archaean Kraaipan Group sediments and volcanic rock. Most of the study area is overlaid by Rietgat and Allanridge Formations, both of the Ventersdorp Supergroup. The eastern region of the Harts River valley comprises the Allanridge Formation, which includes basalt and andesite. The Rietgat Formation includes sandstone, tuff, limestone and andesitic lavas (Liebenberg 1977). To the west of the valley, the Schimidtdrif and Camvellrand subgroups can be found, which consist of dolomite, limestone, quartzite, shale and chert (Schutte 1994).

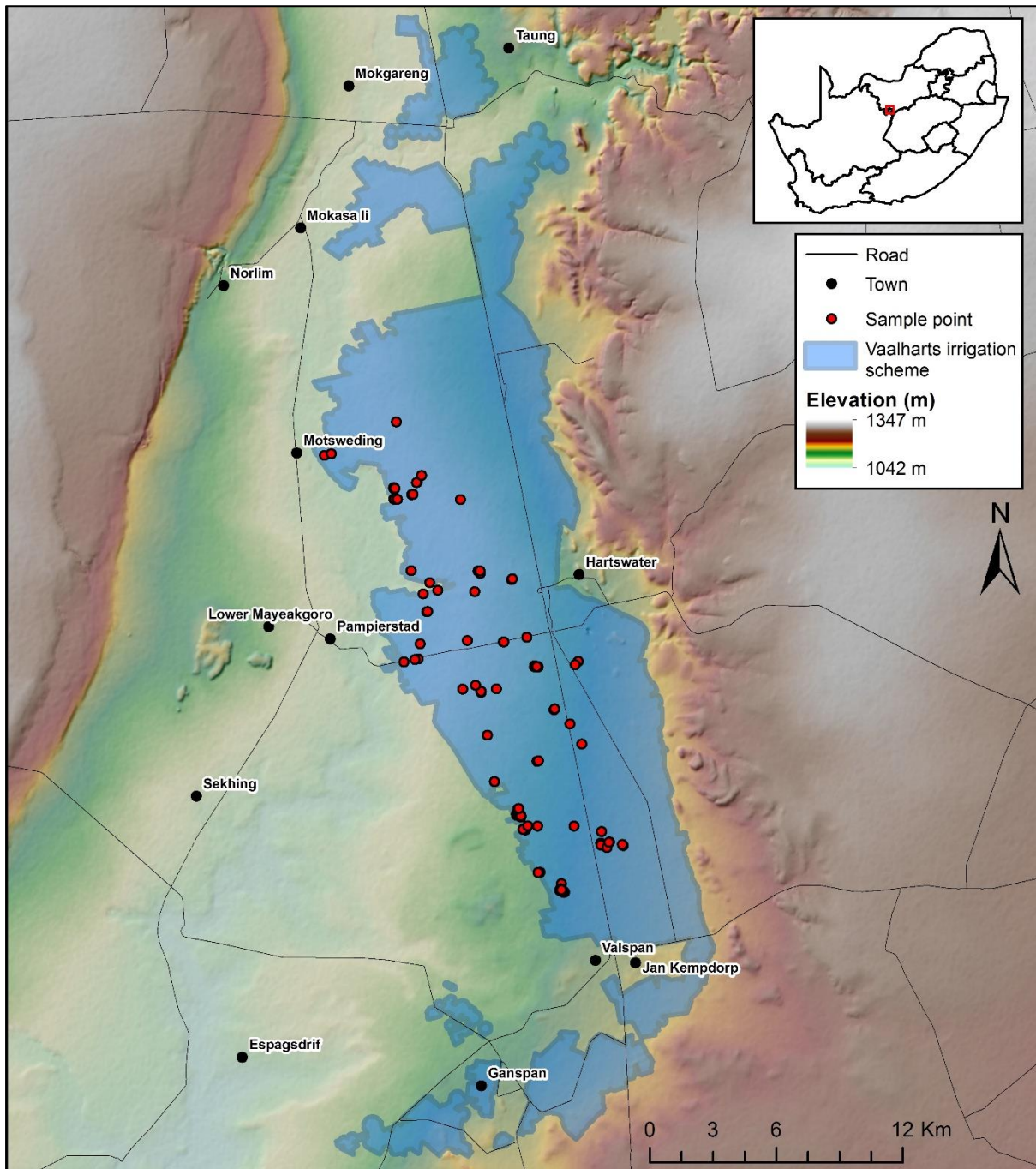


Figure 4.1: Location of the Vaalharts study area. Also shown is the extent of the Vaalharts irrigation scheme and the distribution of the soil samples obtained during the field surveys.

The Breede river irrigation scheme (Figure 4.2) is located in Breede River valley in the Western Cape province of South Africa and covers an area of 57 415 ha. Its altitude ranges from 91 m to 2064 m above mean sea level. Nearby towns include Robertson and Worcester. The area has a Mediterranean climate and a mean annual rainfall of 324 mm. Rainfall mostly occurs during the winter months (between May and October), when the mean monthly rainfall is 31 mm (Schulze, Lynch & Maharaj 2006). During these months, the mean minimum and maximum temperatures are 1.3°C and 30.7°C respectively (Schulze & Maharaj 2006). In summer the mean minimum and maximum temperatures increase to 4.3°C and 37.6°C respectively (Schulze & Maharaj 2006),

while the mean monthly rainfall drops to 10.8 mm (Schulze, Lynch & Maharaj 2006). Vines, orchards and lucerne are the main crops planted in the area. Due to the inflow of saline irrigation from various irrigation districts, the quality of the irrigation water in the Breede River progressively deteriorates in a downstream, south-eastern direction. This creates problems for users who extract water for agricultural irrigation at the lower end of the river (Ghassemi, Jakeman & Nix 1995).

The central region of the Breede River valley has a gentle hilly topography and lies between the Langeberg Mountains in the north and the Riviersonderend Mountains in the south. The Langeberg Mountains can reach heights of about 2 064 m, whereas heights of the Riviersonderend Mountain range between 300 m and 800 m. These mountain ranges consist of sandstone and resistant quartzites to the north, and sandstone and shales to the south (Kirchner 1995; Ghassemi, Jakeman & Nix 1995). The mountain ranges composed of quartzites mostly comprise Hutton, Clovelly, Constantia, La Motte and Champagne soils, whereas pediments and valley floors consist of the Clovelly, Constantia, La Motte, Fernwood and Champagne soils. Irrigated soils along the Breede River may also be composed of Dundee, Oaklead and Fernwood soils (Lambrechts 1979). The dominant salts in Breede River are Na and Cl (NaCl).

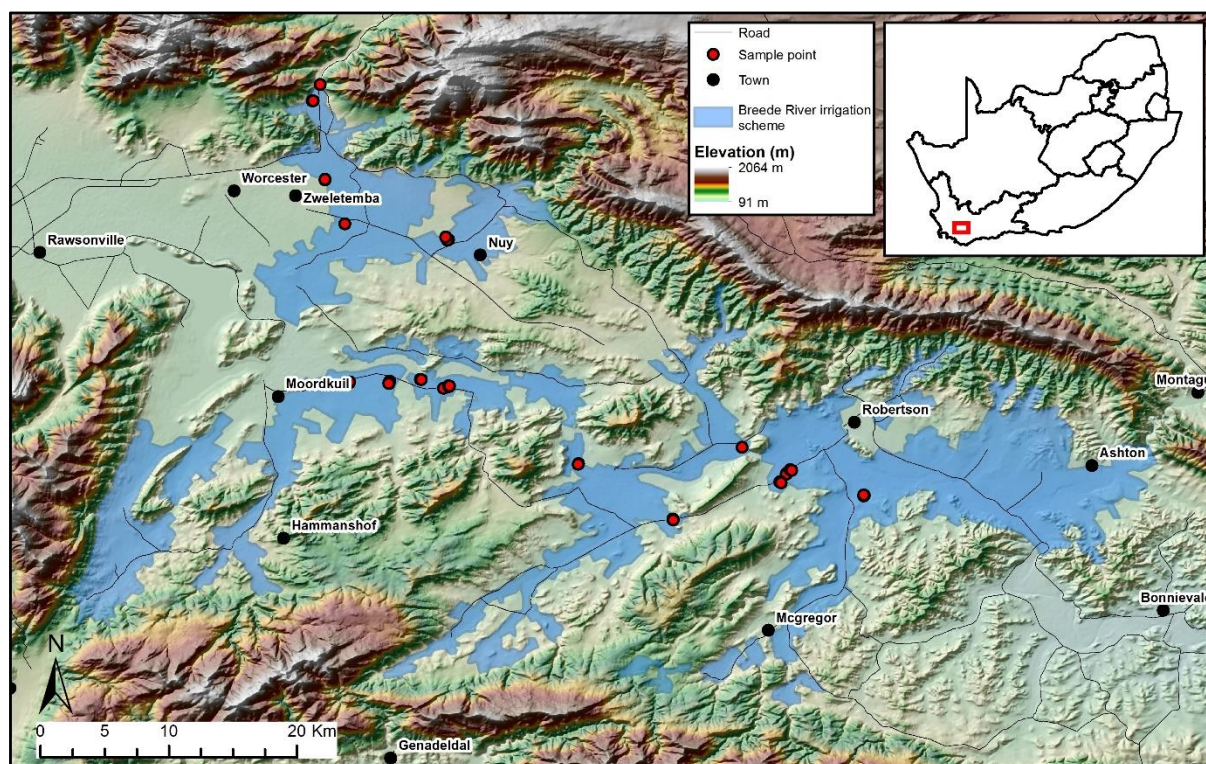


Figure 4.2: Location of the Breede River study area. Also shown is the extent of the Breede River irrigation scheme and the distribution of the soil samples obtained during the field surveys.

4.3.2 Data collection and preparation

Stereoscopic aerial photographs, the SRTM DEM, as well as soil samples were collected for this study. Details about each dataset are provided in the following subsections.

4.3.2.1 Digital elevation models (DEMs)

The 30 m resolution SRTM DEM was acquired for both study areas (Rabus et al. 2003). The SRTM DEM covers the entire globe and is freely available. The DEM was produced from C-band radar (Hensley, Rosen & Gurrola 2000) and has a horizontal accuracy of 20 m and an absolute vertical accuracy of about 16 m (Smith & Sandwell 2003). According to Guth (2006) and Hayakawa, Oguchi and Lin (2008), the SRTM DEM underestimates slope in high-relief areas and overestimates average slope in flat regions. More information on the accuracy and resolution of the SRTM DEM can be found in Hayakawa et al. (2008) and Huggel et al. (2008).

Stereoscopic aerial images acquired from the Chief Directorate: National Geospatial Information (CD: NGI) of South Africa was used to develop a 2 m spatial resolution DSM of each study area. The DSM generation comprised two steps, namely 1) epipolar pair generation; and 2) image matching. During epipolar pair generation, the y-parallax between left and right stereo images was removed to reduce the processing time of identifying matching pixels during the image matching step (Zomer, Ustin & Ives 2002; Deilami & Hashim 2011). Image matching was then used to automatically identify matching features (points, lines, curves and regions) on the overlapping stereo images. Elevation values were then extracted to produce high quality DSMs (Zhang & Fraser 2008). PCI Geomatica 2013 software was used for generating the DSMs in this study.

Given that groundwater flow tends to follow general topographic patterns and therefore depend less on small-scale variations (Sørensen & Seibert 2007), the resolution of the generated DSMs was resampled to 20 m using the Aggregate tool in ArcGIS 10. A cell factor of four and the mean aggregation type was employed. Thompson et al. (2001) also found that lowering a DEM's horizontal resolution reduces local variance (noise) and results in a product that is smoother and more suitable for terrain analyses.

4.3.2.2 Input variable generation

The System for Automated Geoscientific Analyses (SAGA) software package was used to generate the following DEM derivatives (Elnaggar & Noller 2010; Akramkhanov et al. 2011; Taghizadeh-Mehrjardi et al. 2014; Taghizadeh-Mehrjardi et al. 2016): 1) elevation; 2) slope aspect; 3) slope gradient; 4) convergence index; 5) cross-sectional curvature (CSC); 6) longitudinal curvature; 7) relative slope position (RSP); 8) mid-slope position (MSP); 9) normalized height

(NH); 10) slope height (SH); 11) standardized height; 12) downslope distance gradient (DDG); 13) real surface area; 14) terrain ruggedness index; 15) terrain surface texture (TST); 16) topographic position index (TPI); 17) channel network base level (CNBL); 18) closed depressions; 19) LS-factor (slope length and steepness factor); 20) valley depth; 21) vertical distance to channel network (VDTCN); 22) catchment area; 23) slope limited flow accumulation (SLFA); 24) topographic wetness index (TWI); 25) SAGA wetness index (SWI) (Böhner et al. 2002; Böhner, McCloy & Strobl 2006); and 26) height above nearest drainage (HAND) (Rennó et al. 2008). All 26 variables were derived from the SRTM DEM and DSMs respectively, resulting in two feature sets per study area.

A PCA, which condenses variables to produce a set of uncorrelated variables ordered in terms of variance (Eldeiry & Garcia 2009; Behrens et al. 2010), was applied to each feature set. Nearly all (99.9%) of the variance of the input variables were condensed to a single component for both the DSM and SRTM DEM derivatives in Vaalharts. In Breede River, the first principal component contained 99.9% of the variance associated with the DSM derivatives, while containing 85.6% of SRTM DEM derivatives. The resulting first principal component (PC1) was included in each feature set. Table 4.1 summarizes the derivatives (27) considered in this study.

Table 4.1: DEM derivatives included in each feature set

| Type | Variables ^{a)} | # of variables |
|-----------------------|---|----------------|
| Elevation | Mean height above sea level, NH, STDH | 3 × 2 |
| Hydrology | CNBL, closed depressions, LS-factor, valley depth, VDTCN, catchment area, SLFA, HAND | 8 × 2 |
| Morphometry | Aspect, slope, convergence index, CSC, longitudinal curvature, RSP, MSP, SH, DDG, real surface area, terrain ruggedness index, TST, TPI | 13 × 2 |
| Wetness indices | TWI, SWI | 2 × 2 |
| Image transformations | PC1 | 1 × 2 |

^{a)}NH, normalized height; CNBL, channel network base level; LS-factor, slope length and steepness factor; VDTCN, vertical distance to channel network; SLFA, slope limited flow accumulation; HAND, height above nearest drainage; CSC, cross-sectional curvature; RSP, relative slope position; MSP, mid-slope position; SH, slope height; DDG, downslope distance gradient; TST, terrain surface texture; TPI, topographic position index; TWI, topographic wetness index; SWI, SAGA wetness index; PC1, first principal component.

4.3.2.3 Soil sample collection

A total of 175 and 63 soil samples were collected for the Vaalharts and Breede River study areas respectively. The sample size was based on the suggestion of Beleites et al. (2013) that a minimum of 25 samples per class is needed to assess the performance of a classifier. A comparatively larger number of samples was collected in the Vaalharts area owing to the large range of annual crops that is being produced on a rotation basis throughout the year. Samples were clustered in and around areas where clear indications of salt accumulation occurred (e.g. visible salt crusts on the soil surface). Unaffected soil samples were also collected in the immediate neighbourhood. Topsoil samples were collected at a depth of 0–20 cm by means of a soil auger. The sample positions were measured using a differential GPS with an accuracy of 10 cm. The EC was

determined in a laboratory using the saturated paste technique described by the Non-Affiliated Soil Analysis Work Committee (1991) and Nell and Van Niekerk (2014).

4.3.3 Analyses

A range of 27 terrain derivatives were generated from two different DEMs and used as input to the ML classifiers. For comparison purposes, the same field data was used as input to RM and KED. The results of the experiments were interpreted in the context of finding an operational solution for monitoring salt accumulation in large irrigated areas.

4.3.3.1 Regression modelling

RM, as implemented in IBM SPSS v20.0 software, was used to statistically analyse the relationship between the soil EC and the DEM derivatives. Linear, logarithmic, inverse, quadratic, cubic, power and exponential regression models were evaluated. Stepwise multiple regression and partial least squares (PLS) were also carried out on the 27 input variables (Hansen & Schjoerring 2003; Cho et al. 2007).

4.3.3.2 Geostatistics

By considering a continuous attribute (z) at any unsampled location (u) using z -data ($\{z(u_\alpha), \alpha = 1, \dots, n\}$), the basic linear regression estimator ($Z^*(u)$) for all kriging algorithms can be defined as (Goovaerts 1999):

Equation 4.1

$$Z^*(u) - m(u) = \sum_{\alpha=1}^{n(u)} \beta_\alpha(u) [Z(u_\alpha) - m(u_\alpha)]$$

where $\beta_\alpha(u)$ is the weight assigned to datum $z(u_\alpha)$ interpreted as a realization of the random variable $Z(u_\alpha)$ and is located within a given neighbourhood $W(u)$ centred on u . To minimize error variance, the $n(u)$ weights are chosen under the constraint of unbiasedness of the estimator. Variants in kriging methods are dependent on the trend $m(u)$ variable of the algorithm. Intended as a generalized case of kriging, KED models the trend as a function of the available auxiliary data (Hengl, Heuvelink & Rossiter 2007). The $m(u)$ trend for KED is calculated as follows (Goovaerts 1999):

Equation 4.2

$$m(u') = \sum_{k=0}^K a_k(u') f_k(u')$$

where $\alpha_k(u') \approx a_k$ constant but unknown $\forall u' \in W(u)$.

A more detailed description of kriging can be found in Goovaerts (1999).

KED was performed on each individual variable as well as on the full set (27). Subsets of derivatives were also evaluated to investigate whether a reduction in feature space dimensionality improves the results. The subsets consisted of the two, three and four individual derivatives with the highest OAs. In addition to the non-logarithmic KED models, logarithmic transformations were also applied to each of the models to reduce the effect of skewed distributions and very large values, as was the case with the EC values obtained in this study (Gundogdu & Guney 2007). Several variograms (e.g. exponential, quadratic) that define the variations between neighbouring values as a function of the geographic distance between the evaluated points within a study area (Eldeiry & Garcia 2009) were employed.

Two types of variogram approaches to estimate a grid from a set of points, namely global-fit and local-fit, were used. The latter only takes into account the significant sample points identified for a selected area within the study area, whereas global-fit calculates a single function for the entire study area (Gundogdu & Guney 2007). The SAGA software package was used to perform the global-fit KED.

A threshold value of 4 dS/m was applied to the regression and geostatistical models to produce a binary classification of salt-affected and unaffected areas. Modelled values greater than this threshold were considered salt-affected. A sensitivity analysis was carried out to investigate whether the use of different thresholds (from 2 to 6 dS/m) would have any marked impact on the classification results.

4.3.3.3 Machine learning

The *k*NN, SVM, DT and RF ML classifications were performed using the OpenCV implementations of the algorithms (Bradski 2000). *k*NN is a simple non-parametric, distance-based classifier that labels each unknown instance based on its *k* neighbouring known instances (Cover & Hart 1967; Gibson & Power 2000). *k*NN has the disadvantage of assigning equal weight to all variables, even though certain variables may have higher priority. This can result in incorrect class assignments and diffuse clusters (Cunningham & Delany 2007). To avoid this, only odd *k*-values (namely 1, 3 and 5) were used in this study, as suggested by Campbell (2006).

SVM determines the optimal separating hyperplane between classes by focussing on the training samples (support vectors) close to the edge of the class descriptors and consequently minimizing misclassifications (Tzotsos & Argialas 2006; Lizarazo 2008; Novack et al. 2011). As recommended by Hsu et al. (2010), the kernel type for the SVM classifier was set to the radial

basis function. The remaining parameters were left as default. See Vapnik (2000) and Huang et al. (2002) for a more detailed explanation of SVM.

A DT identifies relationships between a response variable known as the dependent variable, and multiple, continuous variables known as the independent variables. DTs hierarchically split a dataset into increasingly homogeneous subsets known as nodes (Punia, Joshi & Porwal 2011; Gómez et al. 2012). By recursively splitting the feature datasets, a leaf node is reached, with the class associated with the node assigned to the observation (Pal & Mather 2003). According to Pal and Mather (2003) and Novack et al. (2011), each node is limited to a split in feature space orthogonal to the axis of the selected feature. Each branch of the DT consists of divisions (or rules) of the most probable class. Applying these rules will assign the most likely class to an unknown instance (Lawrence & Wright 2001).

RF is an enhancement of DTs (Immitzer, Atzberger & Koukal 2012) and generates each DT by using a random vector sampled independently from the input vector. A vote is cast by each of the generated DTs (Breiman 2001; Pal 2005; Bosch, Zisserman & Muoz 2007). Each classifier contributes a single vote to the assignment of the most popular class of the input variable (Breiman 2001; Rodriguez-Galiano et al. 2012a). RF makes use of bagging (Breiman 2001; Rodriguez-Galiano et al. 2012b), a method that generates a training set for feature selection. This allows RF classifiers to have a low (even lower than DT classifiers) sensitivity to training set size (Rodriguez-Galiano et al. 2012a). Two parameters are required to be set, namely the number of trees and the number of active (predictive) variables. The number of active variables for RF was set to one, three, five and ten, whereas the number of trees was set to 100. Rodriguez-Galiano et al. (2012a) showed that stability in accuracy is achieved at 100 trees and that a small number of split variables are optimal for reducing generalization errors and correlations between trees. A more detailed discussion of the RF classifier can be found in (Breiman 1996; Breiman 2001; Rodriguez-Galiano et al. 2012b).

A total of 125 and 43 soil samples (70% of total) were used for training the classifiers in the Vaalharts and Breede River study areas respectively, while the rest of the samples were used for accuracy assessment.

4.3.4 Accuracy assessment

Maps were created from the rule-based and supervised classifications to identify salt-affected areas within the study areas. An independent set of 50 and 20 soil samples were used as reference samples in the Vaalharts and Breede River study areas respectively. Confusion matrices were used

to calculate the OA, PA, UA, kappa coefficient and the AUROC curve (Evangelista 2006; Congalton & Green 2009).

4.4 RESULTS

Figure 4.3 shows that a good balance between salt-affected and unaffected samples was achieved. More dramatic differences in salinity levels were noted during the field surveys for Vaalharts compared to Breede River. Samples consisting of EC values of less than 4 dS/m were classified as unaffected, whereas samples with EC measurements equal to or greater than 4 dS/m were considered to be salt-affected (Non-Affiliated Soil Analysis Work Committee, 1991; Nell & Van Niekerk, 2014).

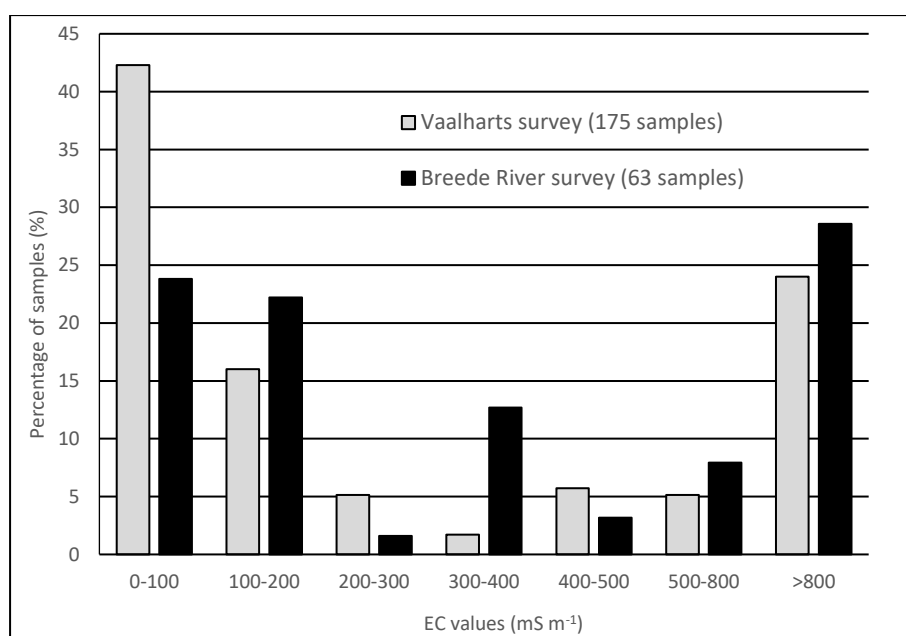


Figure 4.3: EC values of soil samples collected in the study areas

Table 4.2 shows the mean, median, minimum, maximum, coefficient of variation (CV), kurtosis and skewness of the training and reference samples for each of the study areas. From Table 4.2 it is clear that there is sufficient relation between the training and reference.

Table 4.2: Statistical profiles of the training and reference samples for each study area

| Measurement (dS/m) ^{a)} | Vaalharts | | | Breede River | | |
|----------------------------------|-------------|----------|-----------|--------------|----------|-----------|
| | All samples | Training | Reference | All samples | Training | Reference |
| Mean | 9.7 | 9.5 | 10.2 | 12.2 | 9.5 | 18.2 |
| Median | 1.5 | 1.3 | 3 | 3.2 | 3.2 | 2.9 |
| Minimum | 0.1 | 0.1 | 0.1 | 0.4 | 0.4 | 0.6 |
| Maximum | 95 | 95 | 84 | 81.6 | 81.6 | 80.8 |
| CV | 2.1 | 2.1 | 1.9 | 1.7 | 1.8 | 1.4 |
| Kurtosis | 7.4 | 7.4 | 8.4 | 4.4 | 9.3 | 1.1 |
| Skewness | 2.8 | 2.8 | 2.9 | 2.3 | 3 | 1.5 |

^{a)}CV, coefficient of variance

Table 4.3 summarizes the accuracies of the RM, KED and ML classifications. For the sake of brevity, only the three strongest models for each method are included in the table. Also provided

are the source DEM and the feature set on which the method was performed. For the regression models the goodness-of-fit (R^2) values are noted.

Table 4.3: Three top-performing regression models, KED models and ML classifiers for the study areas

| Method | Study area ^{a)} | DEM | Feature ^{b)} | Model | $R^{2(c)}$ | Class | PA (%) | UA (%) | OA (%) | Kappa | AUROC ^{d)} |
|----------------------|--------------------------|------------|-----------------------|-------------|---------------|---------------|--------|-----------|-------------|----------------|---------------------|
| Regression modelling | VH | SRTM | SH | Quadratic | 0.68* | Salt-affected | 72 | 72 | 72 | 0.44 | 0.72*** |
| | | | | | | Unaffected | 72 | 72 | | | |
| | VH | SRTM | SH | Cubic | 0.71* | Salt-affected | 76 | 65.5 | 68 | 0.36 | 0.68*** |
| | | | | | | Unaffected | 60 | 71.4 | | | |
| | VH | SRTM | DDG | Cubic | 0.65* | Salt-affected | 40 | 50 | 50 | 0 | 0.5*** |
| | | | | | | Unaffected | 60 | 50 | | | |
| BR | DSM | NH | Power | 0.15** | Salt-affected | 60 | 66.7 | 65 | 0.3 | 0.65*** | |
| | | | | | Unaffected | 70 | 63.6 | | | | |
| BR | DSM | VD | Exponential | 0.12** | Salt-affected | 20 | 50 | 50 | 0 | 0.5*** | |
| | | | | | Unaffected | 80 | 50 | | | | |
| BR | SRTM | RSP | Quadratic | 0.11** | Salt-affected | 100 | 50 | 50 | 0 | 0.5*** | |
| | | | | | Unaffected | 70 | 63.6 | | | | |
| Kriging | VH | DSM | CSC,ASP,STDH | KED | | Salt-affected | 91.7 | 73.3 | 79.6 | 0.59 | 0.8*** |
| | | | | | | Unaffected | 68 | 89.5 | | | |
| | VH | SRTM | TST | KED | | Salt-affected | 100 | 68.6 | 77.6 | 0.55 | 0.78*** |
| | | | | | | Unaffected | 56 | 100 | | | |
| | VH | DSM | CSC,ASP | KED | | Salt-affected | 91.7 | 68.8 | 75.5 | 0.51 | 0.76*** |
| | | | | | | Unaffected | 60 | 88.2 | | | |
| BR | SRTM | NH | KED | | Salt-affected | 90 | 69.2 | 75 | 0.5 | 0.75*** | |
| | | | | | Unaffected | 60 | 85.7 | | | | |
| BR | SRTM | DDG | KED | | Salt-affected | 80 | 72.7 | 75 | 0.5 | 0.75*** | |
| | | | | | Unaffected | 70 | 77.8 | | | | |
| BR | DSM | TRI, VD | KED | | Salt-affected | 80 | 72.7 | 75 | 0.5 | 0.75*** | |
| | | | | | Unaffected | 70 | 77.8 | | | | |
| Machine learning | VH | SRTM & DSM | All | DT | | Salt-affected | 56 | 73.7 | 68 | 0.36 | 0.68*** |
| | | | | | | Unaffected | 80 | 64.5 | | | |
| | VH | DSM | All | RF (a = 5) | | Salt-affected | 40 | 76.9 | 64 | 0.28 | 0.64*** |
| | | | | | | Unaffected | 88 | 59.5 | | | |
| | VH | SRTM | All | kNN (k = 1) | | Salt-affected | 56 | 66.7 | 64 | 0.28 | 0.64*** |
| | | | | | | Unaffected | 72 | 62.1 | | | |
| BR | DSM | All | DT | | Salt-affected | 90 | 69.2 | 75 | 0.5 | 0.75*** | |
| | | | | | Unaffected | 60 | 85.7 | | | | |
| BR | SRTM | All | DT | | Salt-affected | 70 | 70 | 70 | 0.4 | 0.7*** | |
| | | | | | Unaffected | 70 | 70 | | | | |
| BR | DSM | All | RF (a = 5) | | Salt-affected | 50 | 62.5 | 60 | 0.2 | 0.6*** | |
| | | | | | Unaffected | 70 | 58.3 | | | | |

a)VH, Vaalharts; BR, Breede River

b)SH, slope height; DDG, downslope distance gradient; NH, normalized height; VD, valley depth; RSP, relative slope position; CSC, cross-sectional curvature; ASP, aspect; STDH, standardized height; TST, terrain surface texture; TRI, terrain ruggedness index

c)*, regression results significant at a 0.001 level; **, regression results significant at a 0.01 level

d)***, AUROC results significant at a 0.05 level

Note: The bold values represents the best performing model for each method.

4.4.1 Regression modelling

SH derived from the SRTM DEM produced the strongest model ($R^2 = 0.71$, $p < 0.001$) in Vaalharts, with the relationship being best described by a cubic model. A scatterplot of this model is provided in Figure 4.4. From the scatterplot it is clear that RM tends to underestimate the EC for highly saline samples, with a large proportion of highly saline samples being modelled as having near-zero dS/m values. Weak regression models were produced in the Breede River, with normalized height generating the best model ($R^2 = 0.15$, $p < 0.001$). Weaker models were produced from the stepwise multiple and the PLS regression for both Vaalharts ($R^2 < 0.6$) and Breede River ($R^2 < 0.1$). The kappa values of the best performing regression models suggest a “fair agreement” with the reference data (Landis & Koch 1977).

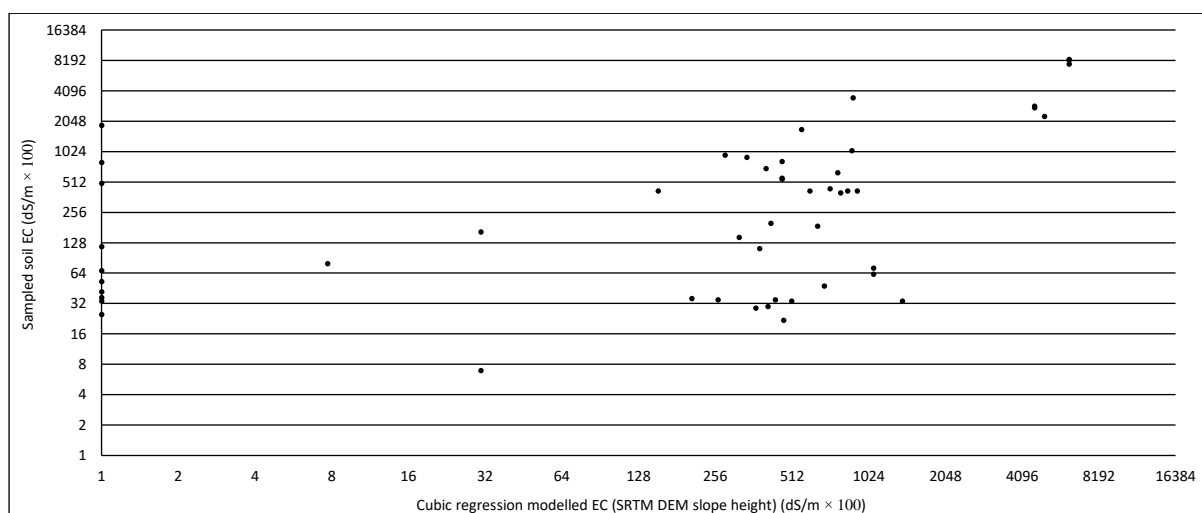


Figure 4.4: Scatterplot of Vaalharts SRTM DEM cubic regression model derived from slope height

The model achieved an OA of 68% ($\kappa = 0.36$) when classified. The marginally weaker ($R^2 = 0.68$, $p < 0.001$) quadratic model produced a slightly better classification (OA = 72%; $\kappa = 0.44$). In spite of the poor goodness-to-fit of this model, it was still reasonably successful (OA = 65%; $\kappa = 0.3$) in separating salt-affected from unaffected soils when classified. As explained in Section 4.3.3.2, different thresholds (from 2 to 6 dS/m) for classifying salt-affected and unaffected areas were considered to assess model sensitivity. The results (not shown here) were consistent with those when 4 dS/m was used as threshold. In some cases, overall accuracies did improve slightly, but at the expense of an imbalance between the user's and producer's accuracies.

4.4.2 Geostatistics

The exponential algorithm was chosen as the appropriate variogram for both the non-logarithmic and logarithmic KED models for Vaalharts and for the logarithmic Breede River KED model, while the quadratic algorithm was found to best represent the non-logarithmic model for Breede River. The non-logarithmic KED model combining the DSM derived cross-sectional curvature, aspect and SH variables achieved the highest OA (79.6%) for Vaalharts ($\kappa = 0.59$). When the scatterplot of this model is interpreted (Figure 4.5a), it is clear that the relationship between the modelled and measured EC is erratic. The KED model also tends to underestimate a large number of highly saline samples as non-saline. The SRTM derived normalized height model (non-logarithmic) showed the most promise for Breede River, producing the highest accuracy (OA = 75%; $\kappa = 0.5$). According to the κ values of these models, there is a “moderate agreement” with the reference data (Landis & Koch 1977). Interestingly, a logarithmic transformation of the input data produced lower OA compared to the untransformed models for both Vaalharts (OA < 65%) and Breede River (OA < 70%). As with the RM model for Vaalharts, a number of highly saline samples were incorrectly classified as being non-saline by the model.

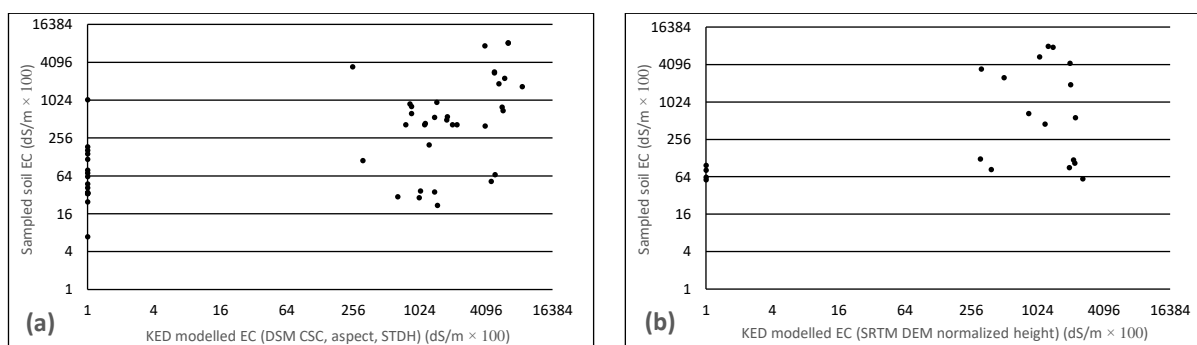


Figure 4.5: Scatterplots of (a) Vaalharts KED model produced from cross-sectional curvature, aspect and standardized height and (b) Breede River SRTM DEM KED model derived from normalized height

As with the RM, the KED models were largely insensitive to variations in classification thresholds (from 2 to 8 dS/m).

4.4.3 Machine learning

The DT classifier achieved the highest accuracy in both Vaalharts (OA = 68%; kappa = 0.36) and Breede River (OA = 75%; kappa = 0.5). The former model was based on both the SRTM DEM and the DSM variables, while in the latter only DSM derivatives were required to achieve the highest accuracies. RF (based on DTs) also attained higher accuracies than the other classifiers, achieving an OA of 64% (kappa = 0.28) in Vaalharts and an OA of 60% (kappa = 0.5) in Breede River. Both RF classifications consisted of the DSM feature set.

4.4.4 Classified maps

Figure 4.6 and Figure 4.7 show the thematic maps of the top four performing classifications for Vaalharts and Breede River respectively. The KED classifications in Vaalharts (Figure 4.6a to Figure 4.6c) appear to be very similar, whereas a substantial difference in the distribution of modelled salt-affected areas is observed when the quadratic regression model (based on SH) classification (Figure 4.6d) is considered.

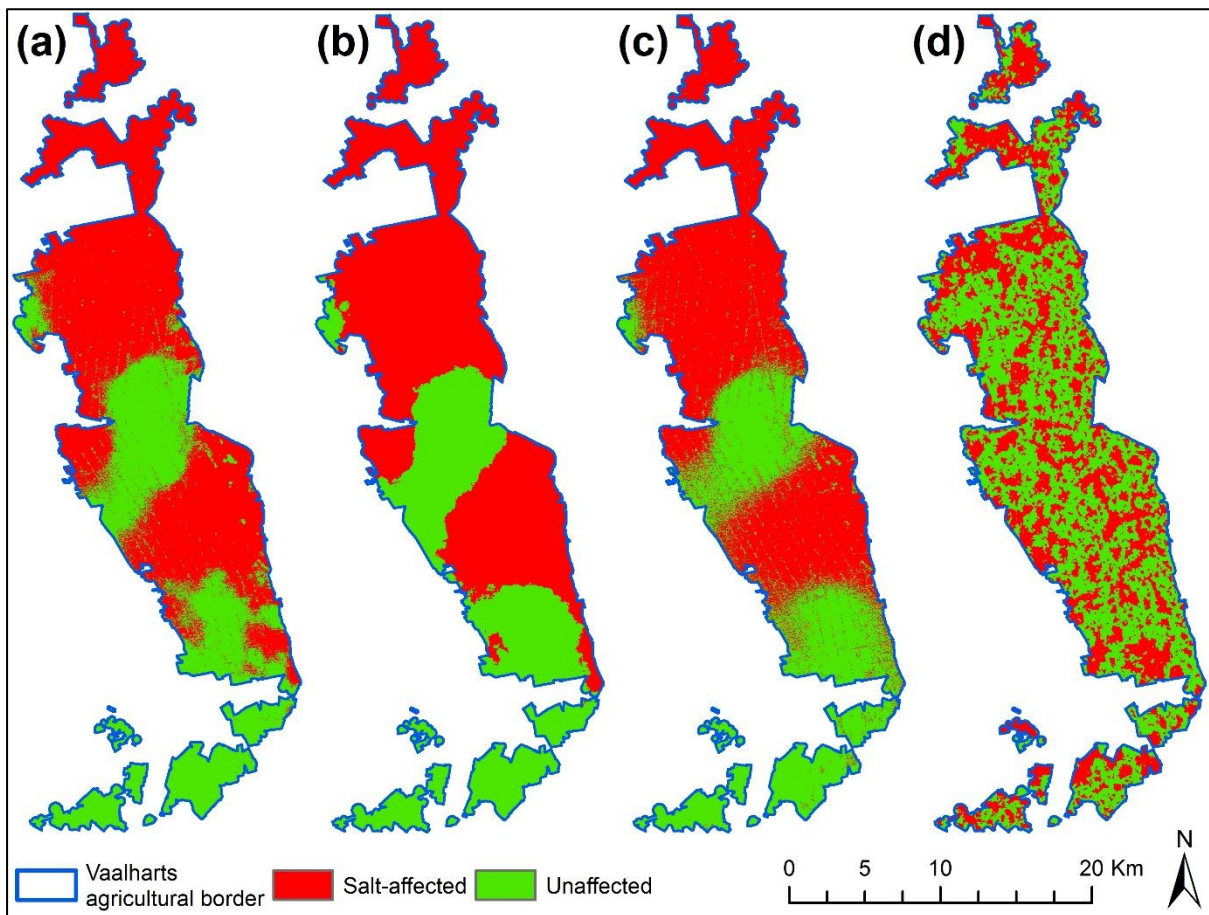


Figure 4.6: Maps produced from the (a) DSM KED model derived from CSC, aspect and standardized height, (b) SRTM DEM KED model derived from TST, (c) DSM KED model derived from CSC and aspect, and (d) quadratic regression model produced from SH for Vaalharts

In Breede River, the maps of the KED models (Figure 4.7a to Figure 4.7c) are less similar, but as with the Vaalharts, the KED models predict large, continuous salt-affected regions. The DT classification (based on the DSM derivatives) resulted in smaller patches of salt accumulation (Figure 4.7d).

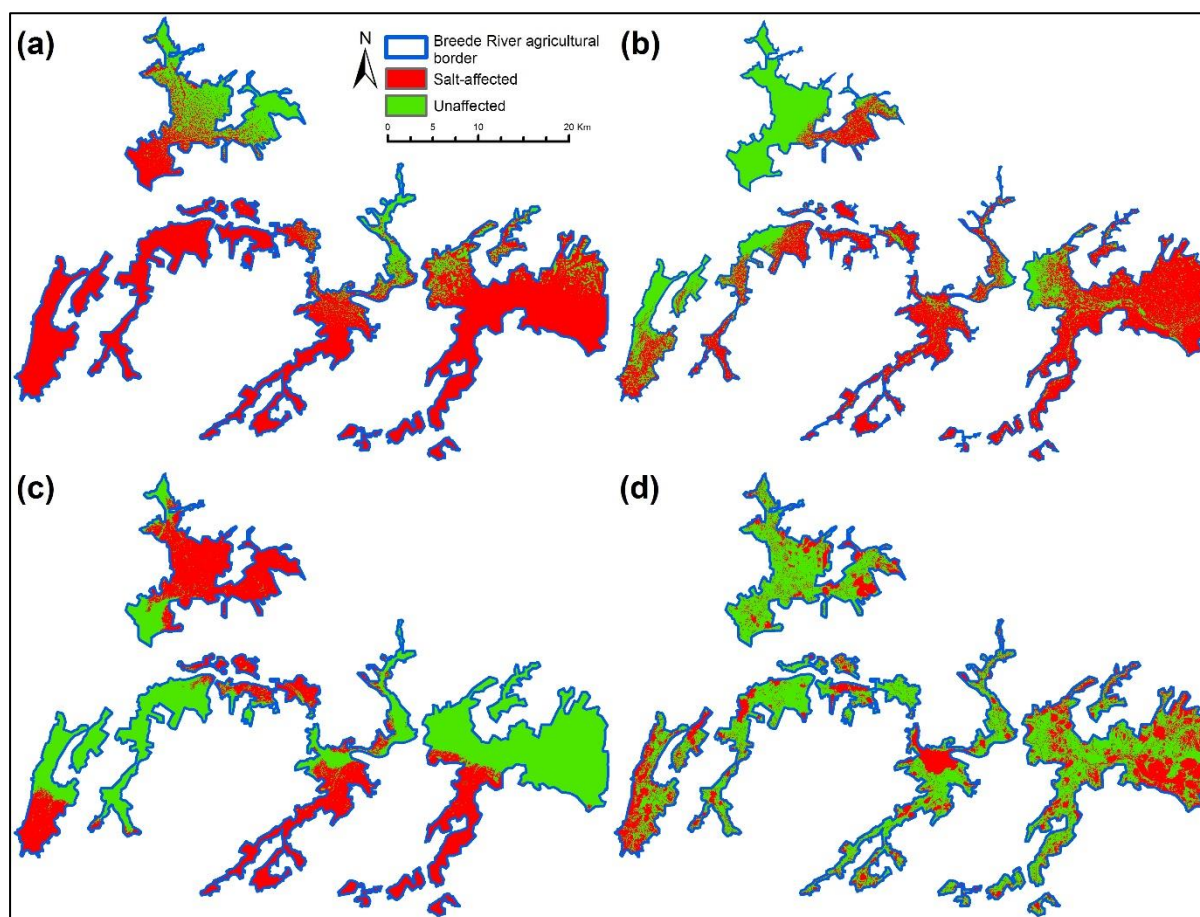


Figure 4.7: Maps produced from the (a) SRTM DEM KED model derived from normalized height, (b) SRTM DEM KED model derived from DDG, (c) DSM KED model derived from TRI and VD, and (d) DSM-based DT classifier for Breede River

4.5 DISCUSSION

In spite of its superior resolution, there was little difference between the DSM-based results and those generated from the SRTM DEM. This can be attributed to the influence of land cover features (e.g. vegetation), particularly in the Breede River where the crops are mainly perennial and woody (e.g. fruit trees and vineyards) (Ghassemi, Jakeman & Nix 1995). Improvements in accuracies were observed in some cases (especially in Vaalharts) where both the SRTM and DSM derivatives were used as input to the ML classifiers, which suggests that the data source did have an influence on the results. Better results may have been obtained with using a DTM generated from light detection and ranging (LiDAR) data, since it has the ability to penetrate foliage (Hesse 2010), but to obtain such data for large regions is still prohibitively expensive, especially in developing countries such as South Africa.

KED produced the most consistent results (OA and kappa standard deviation of 1.75% and 0.03 respectively) and attained the highest accuracies (mean OA and kappa of 76.28% and 0.53 respectively) throughout, which suggest that this technique is most suitable for modelling salt

accumulation when only DEM derivatives are used as input. This result is in agreement with Douaoui and El Ghadiri (2015); Douaoui, Nicolas and Walter (2006); Eldeiry and Garcia (2009); Gallichand et al. (1992); Juan et al. (2011); Taghizadeh-Mehrjardi et al. (2014). Although these studies focussed on OK, CK or RK, the high OA of the KED classification in the present study demonstrates its potential for modelling salt-affected soils. Our results also support the findings of Bishop and McBratney (2001), who applied KED to elevation and terrain data to model soil EC.

A major advantage of KED is its ability to include more than one terrain derivative as input. However, based on our experiments, a decrease in accuracy was observed when more than three derivatives were included in the KED model. Some form of input variable selection is consequently required prior to performing KED. The iterative variable selection approach used in this study will likely be too laborious for operational implementations.

Classifying the regression models into salt-affected and unaffected areas produced relatively poor results (mean OA of 59.2%). This is attributed to the large spatial variation of salt accumulation and the inability of regression modelling to consider autocorrelation effects (Overmars, De Koning & Veldkamp 2003). Spatial autocorrelation, which occurs when information from samples located near each other are not independent (Dormann et al. 2007), can have a positive or negative impact on accuracy assessment results due to the influence of errors at particular locations on neighbouring locations (Congalton 1991).

The ML classifiers showed improvement in accuracies (mean OA = 66.8%; kappa 0.34) over the regression models, but generally attained lower accuracies than the KED models (mean OA = 76.28%, kappa = 0.53). However, in Breede River, the DT classifier (based on DSM variables) was able to match the accuracies of KED (OA = 75%; kappa = 0.5), but was unable to compete with KED in Vaalharts. All of the other ML classifiers (*k*NN, RF and SVM) performed relatively poorly (OA < 70%; kappa ≤ 0.4) in both study areas when compared to the KED models. In spite of this relatively poor performance, ML should not be disregarded, as a major advantage of ML algorithms is their ability to incorporate various types of input data, including remotely sensed imagery. Several studies have shown that ML algorithms are very effective for mapping salt-affected areas using satellite imagery (Dwivedi & Sreenivas 1998; Abbas & Khan 2007; Abood, Maclean & Falkowski 2011; Muller & Van Niekerk 2016a; Abbas et al. 2013; Vermeulen & Van Niekerk 2016), but many authors have noted that such data only consider surface conditions (Dwivedi 1997; Dwivedi, Sreenivas & Ramana 1999; Metternicht & Zinck 2003). In this study we specifically focussed on using terrain data only because it is likely to better represent subsurface conditions. The fact that the DT classifier was able to match the KED results in Breede River is encouraging, because it supports the findings of Elnaggar and Noller (2010) that ML can be used

to investigate both surface (using remotely sensed imagery) and subsurface (using terrain data) conditions. Another advantage of DT is that the resulting tree can be interpreted to better understand the relationships between the input variables and salt accumulation. A model based on DT can also potentially be transferred to other areas with similar conditions without the need for collecting new samples. Clearly more work is needed to investigate the value of using DT (and other ML algorithms) when terrain data is combined with remotely sensed imagery – and other geospatial datasets such as soil type maps (where available) – for the operational monitoring of salt accumulation.

A number of highly saline samples were incorrectly classified by both KED and RM as having a near-zero salinity levels (see Figure 4.4 and Figure 4.5). During the field surveys it was observed that salt accumulation often occurred in small patches and that salinity levels varied dramatically over very short distances (< 10 m). In many cases, these variations occurred on homogenous terrain and were likely caused by farming practices (e.g. over-irrigation). The modelling errors could also have been a factor of the poor quality of the DEMs employed, as small variations within fields were often inadequately represented. The use of more detailed DEMs (e.g. those obtained from high-density LiDAR) will likely improve results.

In this study, a binary classification scheme (i.e. affected and unaffected) was adopted because the purpose was to identify salt-affected and unaffected areas so that they can be used as a scoping mechanism to prioritize more detailed (in situ) investigations. However, it would be of great value to investigate whether the techniques considered in this study would be able to differentiate more salinity classes, e.g. non-saline (< 2 dS/m), slightly saline (2–4 dS/m), moderately saline (4–8 dS/m) and strongly saline (> 8 dS/m).

4.6 CONCLUSION

This study evaluated the use of RM, KED and ML techniques for identifying areas in irrigated fields where salts are likely to accumulate. The methods were evaluated in two study areas, namely the Vaalharts and Breede River irrigation schemes of South Africa. The SRTM DEM and a DSM derived from high resolution stereoscopic aerial photographs were used as the primary data sources. A total of 27 derivatives were generated from the DEMs and used as input to the models evaluated. The results showed that KED outperformed the RM and ML classifiers in most cases, but that ML (specifically the DT classifier) was able to match KED in the Breede River. The source of elevation data did not have a marked influence on the model outputs; however, the higher resolution DSM performed better when combined with ML in the Breede River study area.

From the results of this study, it can be concluded that the use of elevation data and its derivatives, along with geostatistics and ML algorithms, hold much potential for identifying salt-affected areas in irrigated fields. More research is needed to investigate the value of using ML algorithms for classifying a combination of DEM derivatives, satellite images, proximal sensors, other geospatial datasets and a salinity classification scheme making use of multiple cut-off values. This is important in the context of finding operational solutions for identifying areas prone to salt accumulation, especially when considering that the routine collection of large sets of training (and reference) data is not viable for large irrigation schemes and that terrain derivatives can not adequately explain variations in ECe.

CHAPTER 5: DISCUSSION AND CONCLUSIONS

This chapter summarizes the findings of the experiments presented in Chapters 3 and 4. Findings from the direct- and geomorphometry approaches in mapping salt-affected soils are discussed, the aims and objectives are revisited, suggestions for future research are provided and conclusions from the experiments are made.

5.1 REFLECTION ON RESEARCH OBJECTIVES

The aim of the study was to identify direct- and indirect methods for mapping salt-affected or salt-prone soils within agricultural fields using ruleset-based (JM distance, CART and statistical modelling) and supervised classification (ML) approaches. The evaluated approaches were applied to features derived from VHR multispectral satellite imagery (direct approach) and elevation datasets (indirect approach). Conventional methods for monitoring salt accumulation within irrigation schemes require regular field visits and are therefore time-consuming and costly. It is therefore important to identify methods and derivatives (multispectral and terrain) that have the most potential for identifying salt-affected regions over large areas (e.g. irrigation schemes). The main objective of this study was thus to investigate the potential of multispectral RS and geomorphometry approaches for mapping salt accumulation in irrigated agricultural fields.

The first objective was to carry out a review of the literature on RS, geomorphometry and salinization (Chapter 2). Obtained literature showed that both RS and geomorphometry holds much potential for mapping salt accumulation. Most multispectral, bare soil studies focused on medium to low spatial resolution satellite imagery, which are not suitable for identifying salt accumulation in small irrigated fields or the occurrence of salt accumulation in small patches (as it often does in South African irrigation schemes). Although some previous studies had used VHR satellite imagery, none took into account additional spatial features, such as texture measures, and none applied ML.

Geomorphometry was chosen as an indirect method for modelling salt accumulation owing to its ability to take subsurface conditions into account, thereby addressing a well-known limitation of the direct approach. The potential of elevation datasets and geomorphometry techniques in mapping salt-affected soils has been shown in several studies, but none compared the potential of ML approaches to other established methods.

The purpose of the second objective was to identify appropriate study areas in which RS and geomorphometry techniques can be applied to discriminate between salt-affected and unaffected areas. Sections 3.3.1 and 4.3.1 provided information related to the chosen study areas.

The third objective was to collect and acquire empirical data, satellite images and elevation datasets for the selected study areas, and to prepare them for analyses. The acquired WV2 image was described in Chapter 3. The chapter also provided information on the pre-processing steps applied to the imagery, focusing on orthorectification and atmospheric correction. Two DEMs were obtained for the geomorphometry experiment, namely the SRTM DEM (DTM) and a DSM extracted from stereoscopic aerial photographs (Chapter 4). Accounts of the field visits during which in situ data (soil samples) were collected were provided in Chapters 3 and 4.

Determining the VHR WV2 multispectral bands, SIs and other image transformations most appropriate for identifying salt-affected soils in agricultural areas was the focus of the fourth objective (first experiment). A description on the SIs, texture measures and image transformations applied to the WV2 image was documented in Chapters 2 and 3.

The fifth objective (first experiment) focused on applying several statistical and ML methods to the derived VHR WV2 derivatives for identifying salt accumulation (direct approach). Statistical methods included regression analysis, PCA and separability analysis (e.g. JM distance). The MaxL parametric classifier and several non-parametric, ML classifiers (namely k NN, SVM, DT and RF) were applied to the multispectral derivatives. Descriptions of the applied statistical- and ML approaches were provided in Chapters 2 and 3.

As previously stated (see Chapter 3), direct approaches for mapping saline soil do not consider subsurface conditions. To overcome this limitation, the second experiment (objective six) focussed on geomorphometry techniques for identifying salt-affected or salt-prone regions within agricultural fields. Identifying DEMs derived from the SRTM DEM and the stereoscopically extracted DSM that showed the most potential for identifying salt-affected areas were the main focus of objective six. Derivatives attained from the elevation datasets, including several image transformations, wetness indices, and hydrological, morphometric and elevation algorithms were considered. Each of these algorithms were described in Chapters 2 and 4.

A comparison between the effectiveness of ML and geostatistical (kriging) approaches was the goal of the seventh objective (second experiment). ML approaches included k NN, SVM, DT and RF, where KED was the applied geostatistical approach. Chapters 2 and 4 provides descriptions of the approaches applied to the DEM derivatives.

The eighth objective aimed at combining the results from the two experiments and providing recommendations on mapping salt accumulation in irrigation schemes (Chapter 5).

5.2 FINDINGS OF DIRECT AND GEOMORPHOMETRY APPROACHES IN MAPPING SALINE SOILS

The two experiments evaluated the efficacy of direct approaches and indirect approaches, specifically geomorphometry, in mapping saline soil in irrigation schemes. The findings of both experiments are summarized in this section.

5.2.1 ML using VHR multispectral imagery

An evaluation of the reflective properties of salt-affected soils in the Vaalharts irrigation scheme, located in the Northern Cape province of South Africa, found that soils affected by salt accumulation had lower reflectance in the visible region of the electromagnetic spectrum compared to unaffected soils. This is in contrast to the findings of Rao et al. (1995), Metternicht and Zinck (2008) and Elnaggar and Noller (2010), who found salt-affected soils to produce higher reflectance in the visible and NIR regions. The low number of samples (25%) representing high levels of salt precipitation on the soil surface and the frequent occurrence of waterlogging (i.e. secondary salinization) and salt accumulation within the same sampling regions most likely contributed to this discrepancy. Waterlogged or wet soils generally have lower reflectance in the visible and NIR regions, resulting in a smooth and dark appearance (Metternicht & Zinck 2003). Differences in the spectral reflectance of salt-affected and unaffected soils were noted in the green, yellow, red, RE, NIR₁ and NIR₂ bands of the WV2 image. Higher reflectance was found for salt-affected soils in the NIR₁ and NIR₂ regions, which agrees with the findings of Rao et al. (1995), Metternicht and Zinck (2008) and Elnaggar and Noller (2010). In addition to the WV2 bands, several SIs, texture measures and the first principal component were also evaluated. NDSI, calculated from the yellow and NIR₁ bands, showed the most promise in predicting salt accumulation as it featured in the separability analysis, RM and CART. This result supports the findings of Abood, Maclean and Falkowski (2011), who showed that NDSI calculated from the WV2 yellow and NIR₁ bands is a good predictor of saline soil. Other studies have also found NDSI to provide a good estimate of saline soils (Khan et al. 2005; Setia et al. 2013; Douaoui & El Ghadiri 2015).

Several methods for predicting salt-affected soils were evaluated, namely RM, the JM separability measure, CART analysis and five supervised ML classifiers (*k*NN, MaxL, SVM, DT and RF). The threshold determined by the CART analysis produced the most promising result. NDSI (yellow and NIR₁) was selected by the CART analysis as the main and only predictor of the resulting tree. Assessment of the ML classifiers showed *k*NN and RF to produce accuracies that are only marginally lower than that of the CART analysis. The MaxL classifier attained poor accuracies in separating saline soils from unaffected soils, most likely a result of the method's inability to assess

large input feature sets (Myburgh & Van Niekerk 2013). SVM also performed poorly, which is in contrast to what Lizarazo (2008), Li et al. (2010), Petropoulos, Kalaitzidis and Prasad Vadrevu (2012) and Myburgh and Niekerk (2013) found. A moderately strong fit was obtained by the NDSI (yellow and NIR₁) cubic regression model, but the resulting model achieved a lower OA and kappa than the CART, kNN and RF classifications. Both the multistep and PLS regressions produced weaker models than the cubic regression.

Overestimation of salt accumulation were evident in the results. Most cases of salt accumulation were concentrated in small patches and varied substantially over short distances (e.g. 2–5m), but some salt-affected areas were depicted as unrealistically large, continuous areas. This can be attributed to the way in which soil samples were collected. Although both affected and unaffected areas were targeted during the field surveys, most samples were salt-affected (63%). The slight bias towards salt-affected training and reference samples may have had a negative impact on the classifications. This may explain the relatively good performance of kNN and RF, as both methods are insensitive to imbalanced training datasets (Breiman 1996; Breiman 2001; Johnson, Chawla & Hellmann 2012; Rodriguez-Galiano et al. 2012a). Soil preparations, such as ploughing, may also have had a negative effect on the classifications due to alteration of the soil surface, which affects the reflectance from the soil. Another factor to consider is the difficulty in obtaining imagery during a period in which the soil is completely bare within the irrigation fields. For this experiment, the WV2 image was acquired during the harvesting period, but only 73% of the study area was found to consist of bare soil. For more information on this experiment see Chapter 3.

5.2.2 Geomorphometry

The greatest disadvantage of the direct approach (i.e. detecting salt accumulation by observing bare soils) is that the method is limited to the spectral reflectance of the topsoil and therefore it is unable to detect subsurface conditions. Indirect methods, such as vegetation stress monitoring (Muller & Van Niekerk 2016a) and geomorphometry (see Section 2.2) allow subsurface processes to be taken into account. For the second experiment, digital elevation data were used to model areas that are susceptible to salt accumulation. In addition to the main objective, a DTM (30 m) and a DSM (20 m) were used to derive the evaluated terrain derivatives, and several methods, namely RM, KED and ML approaches, were compared. The Vaalharts and Breede River irrigation schemes of South Africa were chosen as study areas. The higher spatial resolution DSM showed no notable difference in accuracies compared to the lower spatial resolution DTM, but accuracy improvements were observed when both DEMs were provided as input for the machine learning classifiers. The small difference in accuracies may be a result of land cover features (e.g. vegetation) present in the DSM.

KED achieved the highest accuracy in identifying soils susceptible to salt accumulation in both Vaalharts and Breede River, whereas the DT classification performed on par with KED in Breede River. The potential of geostatistical approaches in mapping saline soil has been demonstrated by Gallichand et al. (1992), Bishop and McBratney (2001), Douaoui, Nicolas and Walter (2006), Eldeiry and Garcia (2009), Juan et al. (2011), Taghizadeh-Mehrjardi et al. (2014) and Douaoui and El Ghadiri (2015). A combination of the CSC, aspect and STDH variables, derived from the DSM, were included in the KED model for Vaalharts. NH (SRTM DEM derived) were the only trend variable included for the Breede River KED model. Although KED allows the inclusion of several variables to calculate the trend, a decrease in accuracy was observed when more than three variables were included. This severely limits the size of the method's feature dimensionality. Overall, RM mostly showed poor accuracies compared to KED and the ML classifiers, achieving a moderately strong fit between SH (DTM) and soil EC for Vaalharts (cubic). Weaker models were produced in Breede River, with the strongest fit achieved by NH derived from the DSM (power). Multistep and PLS regression showed no improvement in accuracies. The DT ML classifier also attained reasonable accuracies, especially in Breede River where DT performed on par with KED. For more information on this experiment, see Chapter 4. These results support the findings of Elnaggar and Noller (2010) who found that ML can be applied to map both surface (direct approach) and subsurface (indirect approach) conditions. ML approaches are also less time-consuming, allow the inclusion of a larger feature set (Myburgh & Van Niekerk 2013) and can more easily be automated in comparison to geostatistical methods.

5.3 SUGGESTIONS FOR FUTURE RESEARCH

An important approach that needs to be considered is a combination of direct and indirect methods (e.g. geomorphometry and vegetation stress monitoring). As stated in Section 3.6, direct methods do not take subsurface conditions into account. Combining vegetation stress monitoring and geomorphometry techniques with direct methods will overcome this disadvantage. Making use of hyperspectral imagery may also prove useful as it consists of 100s of narrowly defined spectral bands. Higher spatial resolution DEMs should also be considered when using geomorphometry, especially when the data is used in combination with high resolution multispectral or hyperspectral imagery. Geostatistical approaches, namely KED, clearly show high potential for identifying salt-affected areas in irrigation fields (see Chapter 4), but other kriging algorithms, such as RK or UK, should also be considered. A salinity classification scheme making use of multiple cut-off values should also be investigated.

5.4 CONCLUSION

Salt accumulation can have a severe negative impact on agricultural areas and crop yields. Traditional methods of monitoring salt accumulation in agricultural regions are costly and time-consuming, while RS approaches that can monitor large areas simultaneously are potentially more cost-effective.

This study investigated the potential of VHR multispectral satellite imagery and geomorphometry in identifying salt-affected or salt-prone soil. Focus was placed on the performance of ML classifiers, by comparing their outputs to those of other classification approaches (e.g. JM distance, RM and KED).

From the experiments presented in this thesis it can be concluded that direct and geomorphometry approaches hold much potential for mapping salt-affected soil. The ML classifiers also proved to be a viable option in identifying salt-affected or salt-prone soil. A combination of direct- and indirect (e.g. vegetation stress monitoring) approaches should be considered, and making use of alternative data sources such as hyperspectral imagery or higher spatial resolution DEMs may also prove useful. This thesis demonstrated that RS and geomorphometry are viable alternatives to conventional methods for monitoring salt accumulation. More work is needed to operationalize these methods so that they can be routinely applied over large areas. The resulting information should be made available to all agricultural producers so that South Africa's limited agricultural land can be protected from further degradation. Making this data available to producers will also help maximize agricultural yields and crop quality, thereby increasing food security and stimulating the economy in rural areas.

REFERENCES

- Abbas A & Khan S 2007. *Using Remote Sensing Techniques for Appraisal of Irrigated Soil Salinity*. In LKD Oxley, ed. Proceedings of the MODSIM 2007 International congress on Modelling and Simulation. pp. 2632–2638.
- Abbas A, Khan S, Hussain N, Hanjra MA & Akbar S 2013. Characterizing soil salinity in irrigated agriculture using a remote sensing approach. *Physics and Chemistry of the Earth* 56–57: 43–52.
- Abdelfattah M, Shahid S & Othman Y 2009. Soil Salinity Mapping Model Developed Using RS and GIS - A Case Study from Abu Dhabi , United Arab Emirates. *European Journal of Scientific Research* 26, 3: 342–351.
- Abood S, Maclean A & Falkowski M 2011. Soil Salinity Detection in the Mesopotamian Agricultural Plain Utilizing WorldView-2 Imagery. Michigan Technological University.
- Abrams M 2000. The Advanced Spaceborne Thermal Emission and Reflection Radiometer (ASTER): Data products for the high spatial resolution imager on NASA's Terra platform. *International Journal of Remote Sensing* 21, 5: 847–859.
- Adhikari K, Kheir RB, Greve MB & Greve MH 2013. Comparing Kriging and Regression Approaches for Mapping Soil Clay Content in a Diverse Danish Landscape. *Soil Science* 178, 9: 505–517.
- Africa SS of S 1991. *Methods of Soil Analysis*. In SSSSA: Non-Affiliated Soil Analysis Working Committee. Pretoria.
- Aitkenhead MJ, Coull MC, Towers W, Hudson G & Black H 2012. Predicting soil chemical composition and other soil parameters from field observations using a neural network. *Computers and Electronics in Agriculture* 82, 1: 108–116.
- Akramkhanov A, Martius C, Park S & Hendrickx J 2011. Environmental factors of spatial distribution of soil salinity on flat irrigated terrain. *Geoderma* 163, 1–2: 55–62. Available from: <http://dx.doi.org/10.1016/j.geoderma.2011.04.001>.
- Al-Khaier F 2003. Soil salinity detection using satellite remote sensing. Michigan Technological University. Available from: https://webapps.itc.utwente.nl/librarywww/papers_2003/msc/wrem/khaier.pdf.
- Albert TH 2002. Evaluation of remote sensing techniques for ice-area classification applied to the tropical Quaelccaya ice cap, Peru. *Polar Geography* 26, 3: 210–226.

- Aldakheel Y 2011. Assessing NDVI spatial pattern as related to irrigation and soil salinity management in Al-Hassa oasis, Saudi Arabia. *Journal of Indian Society of Remote Sensing* 39, 2: 171–180.
- Backeberg G, Bembridge T, Bennie A, Groenwald J, Hammes P, Pullen R & Thompson H 1996. *Policy proposal for irrigation in South Africa*.
- Baraldi A & Parmiggiani F 1995. An investigation of the textural characteristics associated with gray level cooccurrencematrix statistical parameters. *IEEE Transactions on Geoscience and Remote Sensing* 33, 2: 293–304.
- Barnard J, Bennie A, Du Preez C, Sparrow J & Van Rensburg L 2012. *Managing salinity associated with irrigation at Orange-Riet and Vaalharts irrigation schemes*.
- Baxter SJ & Oliver MA 2005. The spatial prediction of soil mineral N and potentially available N using elevation. *Geoderma* 128, 3–4 SPEC. ISS.: 325–339.
- Behrens T, Förster H, Scholten T, Steinrücken U, Spies E & Goldschmitt M 2005. Digital soil mapping using artificial neural networks. *Journal of Plant Nutrition and Soil Science* 168, 1: 21–33.
- Behrens T, Zhu A-X, Schmidt K & Scholten T 2010. Multi-scale digital terrain analysis and feature selection for digital soil mapping. *Geoderma* 155, 3–4: 175–185. Available from: <http://dx.doi.org/10.1016/j.geoderma.2009.07.010>.
- Beleites C, Neugebauer U, Bocklitz T, Krafft C & Popp J 2013. Sample size planning for classification models. *Analytica Chimica Acta* 760, Special issue: Chemometrics in Analytical chemistry 2012: 25–33.
- Belgiu M & Drăguț L 2014. Comparing supervised and unsupervised multiresolution segmentation approaches for extracting buildings from very high resolution imagery. *ISPRS Journal of Photogrammetry and Remote Sensing* 96: 67–75.
- Beven K & Kirkby M 1979. A physically based, variable contributing area model of basin hydrology. *Hydrological Sciences Bulletin* 24, 1: 43–69.
- Bhattacharyya A 1943. On a measure of divergence between two statistical populations defined by their probability distributions. *Bulletin of the Calcutta Mathematical Society* 35: 239–258. Available from: <http://www.ams.org/mathscinet-getitem?mr=0010358>.
- Bishop T & McBratney A 2001. A comparison of prediction methods for the creation of field-extent soil property maps. *Geoderma* 103, 1: 149–160.
- Böhner J, Blaschke T & Montanarella L 2008. *SAGA – Seconds Out. Hamburger Beiträge zur*

Physischen Geographie und Landschaftsökologie 19

- Böhner J, Köthe R, Conrad O, Gross J, Ringeler a & Selige T 2002. Soil regionalisation by means of terrain analysis and process parameterisation. In E Micheli, F Nachtergaele, & L Montanarella, eds. European Soil Bureau. The European Soil Bureau, Joint Research Centre, EUR 20398 EN, Ispra, pp. 213–222. Available from: <http://www.scilands.de/referenzen/veroeffentlichung/601Bohner.pdf>.
- Böhner J, McCloy K & Strobl J 2006. *SAGA: Analysis and Modelling Applications*. 115th ed. J Böhner, K McCloy, & J Strobl, eds. Göttinger. Available from: <http://books.google.fr/books/about/SAGA.html?id=1zOAAAAAMAAJ&pgis=1>.
- Böhner J & Selige T 2006. Spatial prediction of soil attributes using terrain analysis and climate regionalisation. *Göttinger Geographische Abhandlungen* 115: 13–28.
- Bosch A, Zisserman A & Muoz X 2007. *Image Classification using Random Forests and Ferns*. In 2007 IEEE 11th International Conference on Computer Vision. Miami, pp. 1–8. Available from: http://ieeexplore.ieee.org/xpls/abs_all.jsp?arnumber=4409066.
- Bradski G 2000. The OpenCV library. *Dr. Dobb's Journal of Software Tools for the Professional Programmer* 25, 11: 122–125.
- Breiman L 1996. Bagging predictors. *Machine Learning* 24, 2: 123–140.
- Breiman L 2001. Random Forests. *Machine Learning* 45: 5–32.
- Breiman L 2001. Random Forests. *Machine Learning* 45: 12–20.
- Bui E & Moran C 2001. Disaggregation of polygons of surficial geology and soil maps using spatial modelling and legacy data. *Geoderma* 103, 1: 79–94.
- Cai S, Zhang R, Liu L & Zhou D 2010. A method of salt-affected soil information extraction based on a support vector machine with texture features. *Mathematical and Computer Modelling* 51, 11–12: 1319–1325.
- Campbell J 2006. *Introduction to remote sensing*. London: Taylor & Francis.
- Chan JCW & Paelinckx D 2008. Evaluation of Random Forest and Adaboost tree-based ensemble classification and spectral band selection for ecotope mapping using airborne hyperspectral imagery. *Remote Sensing of Environment* 112, 6: 2999–3011.
- Cho MA, Skidmore A, Corsi F, van Wieren SE & Sobhan I 2007. Estimation of green grass/herb biomass from airborne hyperspectral imagery using spectral indices and partial least squares regression. *International Journal of Applied Earth Observation and Geoinformation* 9, 4:

414–424.

- Chuvieco E & Huete A 2010. *Fundamentals of satellite remote sensing*. Boca Raton: Taylor & Francis.
- Clark R & Kokaly R 1999. Spectroscopic determination of leaf biochemistry using band-depth analysis of absorption features and stepwise multiple linear regression. *Remote Sensing of the Environment* 67, 3: 267–287.
- Clausi D 2002. An analysis of co-occurrence texture statistics as a function of grey level quantization. *Canadian Journal of Remote Sensing* 28, 1: 45–62.
- Cleve C, Kelly M, Kearns FR & Moritz M 2008. Classification of the wildland-urban interface: A comparison of pixel- and object-based classifications using high-resolution aerial photography. *Computers, Environment and Urban Systems* 32, 4: 317–326.
- Comer M & Delp E 1995. *Multiresolution image segmentation*. In IEEE International Conference on Acoustics, Speech, and Signal Processing. Detroit, pp. 2415–2418.
- Comer ML & Delp EJ 1999. Segmentation of textured images using a multiresolution Gaussian autoregressive model. *IEEE Transactions on Image Processing* 8, 3: 408–420.
- Commission WR 2011. *WRC Knowledge Review 2009/10 (ISBN 978-1-4312-0004-7)*. Available from: www.wrc.org.za.
- Committee N-A soil analysis work 1991. *Methods of soil analysis*. Pretoria, South Africa: SSSSA.
- Congalton R 1991. A review of assessing the accuracy of classifications of remotely sensed data. *Remote Sensing of Environment* 37, 1: 35–46.
- Congalton RG & Green K 2009. *Assessing the accuracy of remotely sensed data: Principles and practices*. London, England: Taylor & Francis.
- Conrad O, Bechtel B, Bock M, Dietrich H, Fischer E, Gerlitz L, Wehberg J, Wichmann V & Böhner J 2015. System for Automated Geoscientific Analyses (SAGA) v . 2 . 1 . 4. *Geoscientific Model Development* 8, 1: 1991–2007.
- Cooley T, Anderson G, Felde G, Hoke M, Ratkowski A, Chetwynd J, Gardner J, Adler-Golden S, Matthew M, Berk A, Bernstein L, Acharya P, Miller D & Lewis P 2002. FLAASH, a MODTRAN4-based atmospheric correction algorithm, its application and validation. *Geoscience and Remote Sensing Symposium*: 1414–1418. Available from: http://ieeexplore.ieee.org/xpls/abs_all.jsp?arnumber=1026134.

- Coopersmith E, Minsker B, Wenzel C & Gilmore B 2014. Machine learning assessments of soil drying for agricultural planning. *Computers and Electronics in Agriculture* 104, 1: 93–104.
- Cover T & Hart P 1967. Nearest neighbour classification. *IEEE Transactions on Information Theory* 13, 1: 21–27.
- Cuartas LA, Tomasella J, Nobre AD, Nobre CA, Hodnett MG, Waterloo MJ, Oliveira SM De, Randow RDC Von, Trancoso R & Ferreira M 2012. Distributed hydrological modeling of a micro-scale rainforest watershed in Amazonia: Model evaluation and advances in calibration using the new HAND terrain model. *Journal of Hydrology* 462–463: 15–27. Available from: <http://dx.doi.org/10.1016/j.jhydrol.2011.12.047>.
- Cunningham P & Delany SJ 2007. *K -Nearest Neighbour Classifiers. Technical Report UCD-CSI-2007-4*
- Deilami K & Hashim M 2011. Very high resolution optical satellites for DEM generation: A review. *European Journal of Scientific Research* 49, 4: 542–554.
- DeMers M 2005. *Fundamentals of geographic information systems*. 3rd ed. Hoboken, New Jersey: John Wiley & Sons, Inc.
- Department 2013. Abstract of agricultural statistics. Available from: <http://www.nda.agric.za/docs/statsinfo/Abstact2013.pdf> [Accessed 23 May 2015].
- Dietrich H & Böhner J 2008. Cold air production and flow in a low mountain range landscape in Hessa. *Hamburger Beiträge zur Physischen Geographie und Landschaftsökologie* 19, 1: 37–48.
- DigitalGlobe 2015. WorldView-2. Available from: https://www.digitalglobe.com/sites/default/files/DG_WorldView2_DS_PROD.pdf [Accessed 21 May 2015].
- Dormann CF, Mcpherson JM, Arau MB, Bivand R, Bolliger J, Carl G, Davies RG, Hirzel A, Jetz W, Kissling WD, Ohlemu R, Peres-neto PR, Schurr FM & Wilson R 2007. Methods to account for spatial autocorrelation in the analysis of species distributional data: a review. *Ecography* 30, 1: 609–628.
- Douaoui A & El Ghadiri I 2015. Combination of remote sensing and kriging to improve soil salinity in the Hmadna plain (Algeria). *Soil-Water Journal*: 1–5.
- Douaoui A, Nicolas H & Walter C 2006. Detecting salinity hazards within a semiarid context by means of combining soil and remote-sensing data. *Geoderma* 134, 1: 217–230.
- Duro DC, Franklin SE & Dube M 2012. Multi-scale object-based image analysis and feature

- selection of multi-sensor earth observation imagery using random forests. *International Journal of Remote Sensing* 33, 14: 4502–4526.
- Duro DC, Franklin SE & Dubé MG 2012. A comparison of pixel-based and object-based image analysis with selected machine learning algorithms for the classification of agricultural landscapes using SPOT-5 HRG imagery. *Remote Sensing of Environment* 118, 1: 259–272. Available from: <http://linkinghub.elsevier.com/retrieve/pii/S0034425711004172> [Accessed 21 July 2014].
- Dwivedi R, Ramana K, Thammappa S & Singh A 2001. The utility of IRS-1C LISS-III and PAN-merged data for mapping salt-affected soils. *Photogrammetric Engineering and Remote Sensing* 67, 10: 1167–1175.
- Dwivedi R & Sreenivas K 1998. Delineation of salt-affected soils and waterlogged areas in the Indo-Gangetic plains using IRS-1C LISS-III data. *International Journal of Remote Sensing* 19, 14: 2739–2751.
- Dwivedi RS 1997. Mapping waterlogged areas in part of the Indo-Gangetic plains using remote sensing. *Geocarto International* 12, June 2012: 65–70.
- Dwivedi RS, Sreenivas K & Ramana K V. 1999. Inventory of salt-affected soils and waterlogged areas: A remote sensing approach. *International Journal of Remote Sensing* 20, 8: 1589–1599.
- Eldeiry A & Garcia L 2009. Comparison of Regression Kriging and Cokriging Techniques to Estimate Soil Salinity Using Landsat Images. *Hydrology Days*: 27–38.
- Eldeiry A & Garcia L 2008. Detecting Soil Salinity in Alfalfa Fields using Spatial Modeling and Remote Sensing. *Soil Science Society of America* 72, 1: 201–211.
- Elnaggar AA & Noller JS 2010. Application of Remote-sensing Data and Decision-Tree Analysis to Mapping Salt-Affected Soils over Large Areas. *Remote Sensing* 2, 1: 151–165. Available from: <http://www.mdpi.com/2072-4292/2/1/151/>.
- Evangelista P 2006. The unbalanced classification problem: Detecting breaches in security. Rensselaer Polytechnic Institute.
- Evans F, Caccetta P & Ferdowsian R 1996. *Integrating remotely sensed data with other spatial data sets to predict areas at risk from salinity*.
- Evans FH, Ferdowsian R & Campbell NA 1996. *Predicting Salinity in the Wadjekanup and Byenup Hill Catchments*.
- Fabris M & Pesci A 2005. Automated DEM extraction in digital aerial photogrammetry:

- Precisions and validation for mass movement monitoring. *Annals of Geophysics* 48, 6: 973–988.
- Falkowski MJ, Hudak AT, Crookston NL, Gessler PE, Uebler EH & Smith AMS 2010. Landscape-scale parameterization of a tree-level forest growth model: a k -nearest neighbor imputation approach incorporating LiDAR data. *Canadian Journal of Forest Research* 40, 2: 184–199. Available from: <http://www.nrcresearchpress.com/doi/abs/10.1139/X09-183>.
- Farifteh J, Farshad a. & George RJ 2006. Assessing salt-affected soils using remote sensing, solute modelling, and geophysics. *Geoderma* 130, 3–4: 191–206.
- Fernandez-Buces N, Siebe C, Cram S & Palacio JL 2006. Mapping soil salinity using a combined spectral response index for bare soil and vegetation: A case study in the former lake Texcoco, Mexico. *Journal of Arid Environments* 65, 4: 644–667.
- Fitzpatrick R 2002. Land degradation processes. In *Regional Water and Soil Assessment for Managing Sustainable Agriculture in China and Australia*, ACIAR Monograph. pp. 119–129. Available from: <http://aciarc.gov.au/system/files/node/468/mn84section2soil-environmentimpacts-part1chapters8-9.pdf>.
- Franco-Lopez H, Ek AR & Bauer ME 2001. Estimation and mapping of forest stand density, volume, and cover type using the k -nearest neighbors method. *Remote Sensing of Environment* 77, 3: 251–274.
- Furby S, JF W, P C & Wheaton G 1995. *Detecting and monitoring salt-affected land*.
- Gallichand J, Buckland G, Marcotte D & Hendry M 1992. Spatial interpolation of soil salinity and sodicity for a saline soil in Southern Alberta. *Canadian Journal of Soil Science* 72, 1: 503–516.
- Gao J & Liu Y 2008. Mapping of land degradation from space : a comparative study of Landsat ETM+ and ASTER data. *International Journal of Remote Sensing* 29, 14: 4029–4043.
- Gao Y, Marpu P, Niemeier I, Runfola DM, Giner NM, Hamill T & Pontius RG 2011. Object-based classification with features extracted by a semi-automatic feature extraction algorithm – SEaTH. *Geocarto International* 26, 5: 413–413.
- Garrett J & Viera A 2005. Understanding interobserver agreement: The kappa statistic. *Family Medicine* 37, 5: 360–363.
- Ghassemi F, Jakeman A & Nix H 1995. *Salinization of land and water resources: Human causes, extent, management and case studies*. Sydney: University of New South Wales Press.

- Gibson P & Power C 2000. *Introductory remote sensing: Digital image processing and applications*. New York: Routledge.
- Gislason PO, Benediktsson JA & Sveinsson JR 2006. Random forests for land cover classification. *Pattern Recognition Letters* 27, 4: 294–300. Available from: <http://linkinghub.elsevier.com/retrieve/pii/S0167865505002242> [Accessed 26 May 2014].
- Gombar O & Erasmus C 1976. *Vaalharts ontwaterings projek*.
- Gómez C, Wulder MA, Montes F & Delgado JA 2012. Modeling forest structural parameters in the mediterranean pines of central Spain using QuickBird-2 imagery and classification and regression tree analysis (CART). *Remote Sensing* 4, 1: 135–159.
- Goovaerts P 1999. Geostatistics in soil science: State-of-the-art and perspectives. *Geoderma* 89, 1: 1–45.
- Gundogdu K & Guney I 2007. Spatial analyses of groundwater levels using universal kriging. *Journal of Earth System Science* 116, 1: 49–55.
- Guth P 2006. Geomorphometry from SRTM. *Photogrammetric Engineering & Remote Sensing* 72, 3: 269–277.
- Hansen PM & Schjoerring JK 2003. Reflectance measurement of canopy biomass and nitrogen status in wheat crops using normalized difference vegetation indices and partial least squares regression. *Remote Sensing of Environment* 86, 4: 542–553.
- Haralick RM, Shanmugam K & Dinstein I 1973. Textural features for image classification. *IEEE Transactions on Systems, Man and Cybernetics* 3, 6: 610–621.
- Harris R 1987. *Satellite remote sensing: An introduction*. New York: Routledge & Kegan Paul.
- Hayakawa Y, Oguchi T & Lin Z 2008. Comparison of new and existing global digital elevation models: ASTER G-DEM and SRTM-3. *Geophysical Research Letters* 35, 17: 1–5.
- Hengl T, Gruber S & Shrestha D 2003. T. Hengl, S. Gruber and D.P. Shrestha August 2003. , August. Available from: http://cnrfiles.uwsp.edu/turyk/Database/Development/MJB/private/Thesis/JournalArticles/hengl_digital_demtalk.pdf [Accessed 28 May 2016].
- Hengl T, Heuvelink G & Rossiter D 2007. About regression-kriging: From equations to case studies. *Computers and Geosciences* 33, 10: 1301–1315.
- Hengl T, Heuvelink G & Stein A 2003. Comparison of kriging with external drift and regression-kriging. *ITC, technical note*. Available from: http://www.itc.nl/library/Academic_output/

[Accessed 10 July 2016].

- Hensley S, Rosen P & Gurrola E 2000. The SRTM topographic mapping processor. *Geoscience and Remote Sensing Symposium, 2000. Proceedings. IGARSS 2000. IEEE 2000 International 3*: 1168–1170.
- Hesse R 2010. LiDAR-derived local relief models: A new tool for archaeological prospection. *Archaeological Prospection 17*, 17: 67–72.
- Heumann B 2011. An object-based classification of mangroves using a hybrid decision tree-support vector machine approach. *Remote Sensing 3*, 11: 2440–2460.
- Heung B, Bulmer CE & Schmidt MG 2014. Predictive soil parent material mapping at a regional-scale: A Random Forest approach. *Geoderma 214–215*, 1: 141–154.
- Hjerdt K, McDonnell J, Seibert J & Rodhe A 2004. A new topographic index to quantify downslope controls on local drainage. *Water Resources Research 40*, May: 1–6.
- Hladik C & Alber M 2014. Classification of salt marsh vegetation using edaphic and remote sensing-derived variables. *Estuarine, Coastal and Shelf Science 141*: 47–57. Available from: <http://dx.doi.org/10.1016/j.ecss.2014.01.011>.
- Hsu C-W, Chang C-C & Lin C-J 2010. A Practical Guide to Support Vector Classification. Available from: <http://www.csie.ntu.edu.tw/~cjlin/papers/guide/guide.pdf> [Accessed 23 May 2015].
- Huang C, Davis LS & Townshend JRG 2002. An assessment of support vector machines for land cover classification. *International Journal of Remote Sensing 23*, 4: 725–749.
- Hubert-Moy L, Cotonnec A, Le Du L, Chardin A & Perez P 2001. A Comparison of Parametric Classification Procedures of Remotely Sensed Data Applied on Different Landscape Units. *Remote Sensing of Environment 75*, 2: 174–187. Available from: <http://linkinghub.elsevier.com/retrieve/pii/S0034425700001656>.
- Huggel C, Schneider D, Miranda P, Delgado Granados H & Käab A 2008. Evaluation of ASTER and SRTM DEM data for lahar modeling: A case study on lahars from Popocatepetl Volcano, Mexico. *Journal of Volcanology and Geothermal Research 170*, 1–2: 99–110.
- Hussain M, Chen D, Cheng A, Wei H & Stanley D 2013. Change detection from remotely sensed images: From pixel-based to object-based approaches. *ISPRS Journal of Photogrammetry and Remote Sensing 80*, 1: 91–106. Available from: <http://dx.doi.org/10.1016/j.isprsjprs.2013.03.006>.
- Immitzer M, Atzberger C & Koukal T 2012. Tree species classification with Random forest

- using very high spatial resolution 8-band WorldView-2 satellite data. *Remote Sensing* 4, 9: 2661–2693.
- Iqbal F 2011. Detection of salt affected soil in rice-wheat area using satellite image. *African Journal of Agriculture Research* 6, 21: 4973–4982.
- Iqbal F & Mehdi M 2008. *Detection of Suitable Soils for Zero-Till Wheat Cultivation in Pakistan using GIs*. In 2008 International Workshop on Earth Observation and Remote Sensing Applications.
- Irons JR & Petersen G 1981. Texture transforms of remote sensing data. *Remote Sensing of Environment* 11, 1981: 359–370.
- Jafari A, Khademi H, Finke PA, Wauw J Van De & Ayoubi S 2014. Spatial prediction of soil great groups by boosted regression trees using a limited point dataset in an arid region, southeastern Iran. *Geoderma* 232–234, 1: 148–163.
- Jain AK, Duin RPW & Mao J 2000. Statistical pattern recognition: a review. *IEEE Transactions on Pattern Analysis and Machine Intelligence* 22, 1: 4–37. Available from: http://ieeexplore.ieee.org/ielx5/34/17859/00824819.pdf?tp=&arnumber=824819&isnumber=17859%5Cnhttp://ieeexplore.ieee.org/xpls/abs_all.jsp?arnumber=824819.
- Johnson R, Chawla N & Hellmann J 2012. *Species distribution modelling and prediction: A class imbalance problem*. In Proceedings of the conference on intelligent data understanding (CIDU). pp. 9–16.
- Juan P, Mateu J, Jordan M, Mataix-Solera J, Meléndez-Pastor I & Navarro-Pedreño J 2011. Geostatistical methods to identify and map spatial variations of soil salinity. *Journal of Geochemical Exploration* 108, 1: 62–72. Available from: <http://dx.doi.org/10.1016/j.gexplo.2010.10.003>.
- Khan N, Rastoskuev V, Sato Y & Shiozawa S 2005. Assessment of hydrosaline land degradation by using a simple approach of remote sensing indicators. *Agricultural Water Management* 77, 1: 96–109.
- Khan NM, Rastoskuev V V., Sato Y & Shiozawa S 2005. Assessment of hydrosaline land degradation by using a simple approach of remote sensing indicators. *Agricultural Water Management* 77, 1–3: 96–109.
- Kirchner J 1995. *Investigation into the contribution of ground water to the salt load of the Breede River, using natural isotopes and chemical tracers*.
- Kovacevic M, Bajat B & Gajic B 2010. Soil type classification and estimation of soil properties

- using support vector machines. *Geoderma* 154, 1: 340–347.
- Kruger M, Van Rensburg J & van den Bergh F 2009. Perspectives on the development of stem borer resistance to Bt maize and refuge compliance at the Vaalharts irrigation scheme in South Africa. *Crop Protection* 28, 8: 684–689.
- Kruger M, Van Rensburg JBJ & Van den Berg J 2009. Perspective on the development of stem borer resistance to Bt maize and refuge compliance at the Vaalharts irrigation scheme in South Africa. *Crop Protection* 28, 8: 684–689.
- Laliberte A, Browning D & Rango A 2012. A comparison of three feature selection methods for object-based classification of sub-decimeter resolution UltraCam-L imagery. *International Journal of Applied Earth Observation and Geoinformation* 15, 1.
- Lambrechts J 1979. Fynbos ecology: A preliminary synthesis. In J Day, W Siegfried, G Louw, & M Jarman, eds. *Geology, geomorphology and soils*. South Africa, Pretoria, pp. 16–26.
- Landis J & Koch G 1977. The measurement of observer agreement for categorical data. *Biometrics* 33, 1: 159–174.
- Lawrence RL, Wood SD & Sheley RL 2006. Mapping invasive plants using hyperspectral imagery and Breiman Cutler classifications (RandomForest). *Remote Sensing of Environment* 100, 3: 356–362.
- Lawrence RL & Wright A 2001. Rule-based classification systems using classification and regression tree (CART) analysis. *Photogrammetric Engineering and Remote Sensing* 67, 10: 1137–1142.
- Lenney MP, Woodcock CE, Collins JB & Hamdi H 1996. The Status of Agricultural Lands in Egypt: The Use of Multitemporal NDVI Features Derived from Landsat TM. *Remote Sensing of Environment* 56, 1: 8–20. Available from: <http://www.sciencedirect.com/science/article/pii/0034425795001522>.
- Li H, Gu H, Han Y & Yang J 2010. Object-oriented classification of high-resolution remote sensing imagery based on an improved colour structure code and a support vector machine. *International Journal of Remote Sensing* 31, 6: 1453–1470.
- Li M, Im J & Beier C 2013. Machine learning approaches for forest classification and change analysis using multi-temporal Landsat TM images over Huntington Wildlife Forest. *GIScience & Remote Sensing* 50, 4: 361–384.
- Li Y, Shi Z, Wu C fang, Li H yi & Li F 2007. Improved prediction and reduction of sampling density for soil salinity by different geostatistical methods. *Agricultural Sciences in China*

6, 7: 832–841.

Li Z, Zhu Q & Gold C 2004. *Digital terrain modeling: Principles and methodology*. CRC Press.

Liebenberg L 1977. *Die geologie van die gebied 2724D (Andalusia)*.

Lillesand T, Chipman J & Kiefer R 2008. *Remote sensing and image interpretation*. 6th ed. New York: John Wiley & Sons.

Liu D & Xia F 2010. Assessing object-based classification: advantages and limitations. *Remote Sensing Letters* 1, 4: 187–194. Available from:
<http://www.tandfonline.com/doi/abs/10.1080/01431161003743173>.

Liu J & Mason P 2009. *Image processing and GIS for remote sensing*. Oxford: John Wiley & Sons.

Lizarazo I 2008. SVM-based segmentation and classification of remotely sensed data. *International Journal of Remote Sensing* 29, 24: 7277–7283.

Lu D & Weng Q 2007. A survey of image classification methods and techniques for improving classification performance. *International Journal of Remote Sensing* 28, 5: 823–870.

Maas E & Hoffman G 1977. Crop salt tolerance - Current assessment. *Journal of the irrigation and drainage division* 103, 2: 115–134.

Maisela J 2007. Realizing agricultural potential in land reform: The case of Vaalharts irrigation scheme in the Northern Cape Province. University of the Western Cape.

Mashimbye Z 2005. Remote sensing based identification and mapping of salinised irrigated land between Upington and Keimoes along the Lower Orange river, South Africa. Stellenbosch University, South Africa.

Mashimbye ZE, Cho MA, Nell JP, De Clercq WP, van Niekerk A & Turner DP 2012. Model-Based Integrated Methods for Quantitative Estimation of Soil Salinity from Hyperspectral Remote Sensing Data: A Case Study of Selected South African Soils. *Pedosphere* 22, 5: 640–649. Available from:
<http://www.sciencedirect.com/science/article/pii/S1002016012600496>.

Mather P & Koch M 2011. *Computer Processing of Remotely-Sensed Images*. 4th ed. Chichester: John Wiley & Sons, Ltd.

McFarlane D, George R & Caccetta P 2004. *The extent and potential area of salt-affected land in Western Australia estimated using remote sensing and digital terrain models*. In 1st National Salinity Engineering Conference. Perth, Australia.

- Mcghie S 2005. *Salinity Indicator Plants*. Sydney, Australia: Department of Infrastructure, Planning and Natural Resources.
- McKillup S 2006. *Statistics explained: An introductory guide for life sciences*. Cape Town, South Africa: Cambridge University Press.
- Metternicht G & Zinck J 2003. Remote sensing of soil salinity: Potentials and constraints. *Remote Sensing of Environment* 85, 1: 1–20. Available from: <http://www.sciencedirect.com/science/article/pii/S0034425702001888>.
- Metternicht G & Zinck J 2008. *Remote sensing of soil salinization: Impact and land management*. G Metternicht & J Zinck, eds. London: Taylor & Francis.
- Mohamed E, Morgun E & Goma Bothina S 2010. Assessment of soil salinity in the Eastern Nile Delta (Egypt) using geoinformation. *Moscow University Soil Science Bulletin* 66, 1: 11.
- Motaghian H & Mohammadi J 2011. Spatial estimation of saturated hydraulic conductivity from terrain attributes using regression, kriging, and artificial neural networks. *Pedosphere* 21, 2: 170–177. Available from: [http://dx.doi.org/10.1016/S1002-0160\(11\)60115-X](http://dx.doi.org/10.1016/S1002-0160(11)60115-X).
- Muller S & Van Niekerk A 2016a. An evaluation of supervised classifiers for indirectly detecting salt-affected areas at irrigation scheme level. *International Journal of Applied Earth Observations and Geoinformation* 49: 138–150. Available from: <http://dx.doi.org/10.1016/j.jag.2016.02.005>.
- Muller S & Van Niekerk A 2016b. Identification of WorldView-2 spectral and spatial factors in detecting salt accumulation in cultivated fields. *Geoderma* 273: 1–11.
- Myburgh G & Van Niekerk A 2013. Effect of Feature Dimensionality on Object-based Land Cover Classification : A Comparison of Three Classifiers. *South African Journal of Geomatics* 2, 1: 13–27. Available from: <http://www.sajg.org.za/index.php/sajg/article/view/64>.
- Myburgh G & Van Niekerk A 2014. Impact of training set size on object-based land cover classification: A comparison of three classifiers. *International Journal of Applied Geospatial Research* 5, 3: 49–67.
- Myint SW, Gober P, Brazel A, Grossman-Clarke S & Weng Q 2011. Per-pixel vs. object-based classification of urban land cover extraction using high spatial resolution imagery. *Remote Sensing of Environment* 115, 5: 1145–1161. Available from: <http://linkinghub.elsevier.com/retrieve/pii/S0034425711000034> [Accessed 30 May 2014].
- Nell J & Van Niekerk A 2014. *Appropriate methods for monitoring salt accumulation and water*

- logging on south African irrigation schemes*. In Third International Salinity Forum, Riverside, California.
- Nell J, Van Niekerk A, Muller S, Vermeulen D, Pauw T, Stephenson G & Kemp J 2015. *Methodology for monitoring waterlogging and salt accumulation on selected irrigation schemes in South Africa*.
- Nemes A, Lilly A, Oude Voshaar J & Otto H 1999. Evaluation of different procedures to interpolate particle-size distributions to achieve compatibility within soil databases. *Geoderma* 90, 1: 187–202.
- Nemes A, Rawls W & Pachepsky Y 2006. Use of the Nonparametric Nearest Neighbor Approach to Estimate Soil Hydraulic Properties. *Soil Science Society of America Journal* 70, 1: 327–336.
- Van Niekerk A 2012. Developing a very high resolution DEM of South Africa. *Position IT* November: 55–60.
- Nobre a. D, Cuartas L a., Hodnett M, Rennó CD, Rodrigues G, Silveira a., Waterloo M & Saleska S 2011. Height Above the Nearest Drainage - a hydrologically relevant new terrain model. *Journal of Hydrology* 404, 1–2: 13–29. Available from: <http://dx.doi.org/10.1016/j.jhydrol.2011.03.051>.
- Novack T, Esch T, Kux H & Stilla U 2011. Machine learning comparison between WorldView-2 and QuickBird-2-simulated imagery regarding object-based urban land cover classification. *Remote Sensing* 3, 10: 2263–2282.
- Nussbaum S, Niemeyer I & Canty MJ 2006. *Seath - a New Tool for Automated Feature Extraction in the Context of Object-Based Image Analysis*. In Proceedings of the 1st International Conference on Object-based Image Analysis. Available from: http://link.periodicos.capes.gov.br/sfxlcl41?url_ver=Z39.88-2004&rft_id=info:sid/IEEE.org:XPLORE&url_ctx_fmt=info:ofi/fmt:kev:mtx:ctx&rft_val_fmt=info:ofi/fmt:kev:mtx:journal.
- O’Sullivan D & Unwin D 2003. *Geographic information analysis*. Hoboken, New Jersey: John Wiley & Sons, Inc.
- Odindi J & Mhangara P 2013. Potential of texture-based classification in urban landscapes using multispectral aerial photos. *South African Journal of Science* 109, 3: 1–9. Available from: http://www.scielo.org.za/scielo.php?pid=S0038-23532013000200009&script=sci_arttext&tlng=pt.

- Olaya V 2004. *A gentle introduction to SAGA GIS*.
- Oommen T, Misra D, Twarakavi N, Prakash A, Sahoo B & Bansopashyay S 2008. An objective analysis of support vector machine based classification for remote sensing. *Mathematical Geosciences* 40, 2008: 409–424.
- Overmars K, de Koning G & Veldkamp A 2003. Spatial autocorrelation in multi-scale land use models. *Ecological Modelling* 164, 1: 257–270.
- Pal M 2005. Random forest classifier for remote sensing classification. *International Journal of Remote Sensing* 26, 1: 217–222.
- Pal M & Mather P 2003. An assessment of the effectiveness of decision tree methods for land cover classification. *Remote Sensing of Environment* 86, 4: 554–565.
- Pal M & Mather P 2005. Support vector machine for classification in remote sensing. *International Journal of Remote Sensing* 26, 5: 1007–1011.
- Pebesma E 2006. The role of external variables and GIS databases in geostatistical analysis. *Transactions in GIS* 10, 4: 615–632.
- Petropoulos GP, Kalaitzidis C & Prasad Vadrevu K 2012. Support vector machines and object-based classification for obtaining land-use/cover cartography from Hyperion hyperspectral imagery. *Computers and Geosciences* 41: 99–107. Available from: <http://dx.doi.org/10.1016/j.cageo.2011.08.019>.
- Pike RJ 2000. Geomorphometry -diversity in quantitative surface analysis. *Progress in Physical Geography* 24, 1: 1–20. Available from: <http://ppg.sagepub.com/content/24/1/1.short> [Accessed 27 September 2015].
- Puissant A, Hirsch J & Weber C 2005. The utility of texture analysis to improve per-pixel classification for high to very high spatial resolution imagery. *International Journal of Remote Sensing* 26, 4: 733–745.
- Punia M, Joshi P & Porwal M 2011. Decision tree classification of land use cover for Delhi, India using IRS-P6 AWiFS data. *Expert Systems with Applications* 38, 2011: 5577–5583.
- Rabus B, Eineder M, Roth A & Bamler R 2003. The shuttle radar topography mission: A new class of digital elevation models acquired by spaceborne radar. *ISPRS Journal of Photogrammetry and Remote Sensing* 57, 4: 241–262.
- Rao BRM, Dwivedi RS, Sreenivas K, Khan QI, Ramana K V, Thammappa SS & Fyzee MA 1998. An inventory of salt-affected soils and waterlogged areas in the Nagarjunsagar canal command area of Southern India, using space-borne multispectral data. *Land degradation*

Development 9: 357–367.

- Rao BRM, Sankar T, Dwivedi R, Thammappa S, Venkataratnam L, Sharma R & Das S 1995. Spectral behaviour of salt-affected soils. *International Journal of Remote Sensing* 16, 12: 2125–2136.
- Rees W 2001. *Physical principles of remote sensing*. New York: Cambridge University Press.
- Rennó CD, Nobre AD, Cuartas LA, Soares JV, Hodnett MG, Tomasella J & Waterloo MJ 2008. HAND, a new terrain descriptor using SRTM-DEM: Mapping terra-firme rainforest environments in Amazonia. *Remote Sensing of Environment* 112, 9: 3469–3481.
- Richter R 2004. *ATCOR: Atmospheric and topographic correction. DLR Report* 565-01
- Richter R 2014. Atmospheric / Topographic Correction for Satellite Imagery. , March. Available from: http://www.rese.ch/pdf/atcor3_manual.pdf [Accessed 23 May 2015].
- Rodríguez P, González M & Zaballos A 2007. Mapping of salt - affected soils using TM images. *International Journal of Remote Sensing* 28, 12: 2713–2722.
- Rodriquez-Galiano VF, Chica-Olmo M, Abarca-Hernandez F, Atkinson PM & Jeganathan C 2012. Random Forest classification of Mediterranean land cover using multi-seasonal imagery and multi-seasonal texture. *Remote Sensing of Environment* 121: 93–107. Available from: <http://linkinghub.elsevier.com/retrieve/pii/S0034425711004408> [Accessed 28 June 2014].
- Rodriquez-Galiano VF, Ghimire B, Rogan J, Chica-Olmo M & Rigol-Sanchez JP 2012. An assessment of the effectiveness of a random forest classifier for land-cover classification. *ISPRS Journal of Photogrammetry and Remote Sensing* 67, 1: 93–104. Available from: <http://linkinghub.elsevier.com/retrieve/pii/S0924271611001304> [Accessed 23 May 2014].
- Schulze R, Lynch S & Maharaj M 2006. *Monthly rainfall and its inter-annual variability*.
- Schulze R & Maharaj M 2006. *Daily mean temperatures*.
- Schutte I 1994. *Die geologie van die gebied Christiana: Toeligting tot blad 2724 Christiana van die Geologiese opname van Suid-Afrika*.
- Setia R, Lewis M, Marschner P, Raja Segaran R, Summers D & Chittleborough D 2013. Severity of salinity accurately detected and classified on a paddock scale with high resolution multispectral satellite imagery. *Land Degradation and Development* 24, 4: 375–384.
- Shainberg I & Shalhevet J 1984. *Soil salinity under irrigation: Processes and management*. Berlin: Springer Verlag.

- Sidike A, Zhao S & Wen Y 2014. Estimating soil salinity in Pingluo County of China using QuickBird data and soil reflectance spectra. *International Journal of Applied Earth Observation and Geoinformation* 26: 156–175. Available from: <http://linkinghub.elsevier.com/retrieve/pii/S0303243413000743>.
- Smith B & Sandwell D 2003. Accuracy and resolution of shuttle radar topography mission data. *Geophysical Research Letters* 30, 9: 1467–1470. Available from: <http://doi.wiley.com/10.1029/2002GL016643>.
- Sørensen R & Seibert J 2007. Effects of DEM resolution on the calculation of topographical indices: TWI and its components. *Journal of Hydrology* 347, 1–2: 79–89. Available from: <http://www.sciencedirect.com/science/article/pii/S0022169407004830>.
- Stal C, Tack F, De Maeyer P, De Wulf A & Goossens R 2013. Airborne photogrammetry and lidar for DSM extraction and 3D change detection over an urban area – a comparative study. *International Journal of Remote Sensing* 34, 4: 1087–1110.
- Stals J 2007. Mapping potential soil salinization using rule based object-orientated image analysis. Stellenbosch University, South Africa.
- Streutker A 1977. The dependence of permanent crop production on efficient irrigation and drainage at the Vaalharts government water scheme. *Water SA* 3, 2: 90–102.
- Sulebak J, Tallaksen L & Erichsen B 2000. Estimation of areal soil moisture by use of terrain data. *Geografiska Annaler* 82, 1: 89–105. Available from: <http://onlinelibrary.wiley.com/doi/10.1111/j.0435-3676.2000.00009.x/abstract>.
- Taghizadeh-Mehrjardi R, Ayoubi S, Namazi Z, Zolfaghari AA & Sadrabadi FR 2016. Prediction of soil surface salinity in arid region of central Iran using auxiliary variables and genetic programming. *Arid Land Research and Management* 30, 1: 49–64.
- Taghizadeh-Mehrjardi R, Minasny B, Sarmadian F & Malone B 2014. Digital mapping of soil salinity in Ardakan region, central Iran. *Geoderma* 213, 2014: 15–28. Available from: <http://www.sciencedirect.com/science/article/pii/S0016706113002565>.
- Thompson JA, Bell JC & Butler CA 2001. Digital elevation model resolution: Effects on terrain attribute calculation and quantitative soil-landscape modeling. *Geoderma* 100: 67–89.
- Townshend J, Cook A, Hancock P, Hardy J, Justice C, Mitchell C & Williams D 1981. *Terrain analysis and remote sensing*. J Townshend, ed. Boston: George Allen & Unwin.
- Tzotsos A & Argialas D 2006. Support vector machine classification for object-based image analysis. In T Blaschke, S Lang, & G Hay, eds. *Object-based image analysis: Lecture notes*

- in geoinformation and cartography. Berlin: Springer, pp. 663–677.
- Utset A, Ruiz M, Herrera J & Ponce de Leon D 1998. A geostatistical method for soil salinity sample site spacing. *Geoderma* 86, 1: 143–151.
- Vapnik V 2000. *The nature of statistical learning theory*. New York: Springer-Verlag.
- Vermeulen D & Van Niekerk A 2016. Evaluation of a WorldView-2 image for soil salinity monitoring in a moderately affected irrigated area. *Journal of Applied Remote Sensing* 10, 2.
- Vermeulen D & Van Niekerk A 2017. Machine learning performance for predicting soil salinity using different combinations of geomorphometric covariates. *Geoderma* 299: 1–12. Available from: <http://www.sciencedirect.com/science/article/pii/S001670611730397X>.
- Viscarra Rossel R, Adamchuk V, Sudduth K, McKenzie N & Lobsey C 2011. Proximal Soil Sensing: An Effective Approach for Soil Measurements in Space and Time. In *Advances in Agronomy*. pp. 237–282.
- Wackernagel H 2010. *Multivariate geostatistics: An introduction with applications*. 3rd ed. Berlin, Germany: Springer Verlag.
- Wang F, Chen X, Luo G, Ding J & Chen X 2013. Detecting soil salinity with arid fraction integrated index and salinity index in feature space using Landsat TM imagery. *Journal of Arid Land* 5, 3: 340–353. Available from: <http://link.springer.com/10.1007/s40333-013-0183-x>.
- Wood J 1996. *The geomorphological characterisation of digital elevation models*. University of Leicester, United Kingdom.
- Yan G, Mas J, Maathuis BHP, Xiangmin Z & Van Dijk PM 2006. Comparison of pixel-based and object-oriented image classification approaches—a case study in a coal fire area, Wuda, Inner Mongolia, China. *International Journal of Remote Sensing* 27, 18: 4039–4055.
- Ying Li & Bo Cheng 2009. An improved k-nearest neighbor algorithm and its application to high resolution remote sensing image classification. *17th International Conference on Geoinformatics*. Available from: <http://ieeexplore.ieee.org/lpdocs/epic03/wrapper.htm?arnumber=5293389>.
- Zhang C & Fraser C 2008. Generation of digital surface model from high resolution satellite imagery. *The International Archives of the Photogrammetry, Remote Sensing and Spatial Information Sciences* 37, B1: 785–790.
- Zhou Q & Liu J 2002. Error assessment of grid-based flow routing algorithms used in

hydrological models. *International Journal of Geographical Information Science* 16, 8: 819–842.

Zomer R, Ustin S & Ives J 2002. Using satellite remote sensing for DEM extraction in complex mountainous terrain: Landscape analysis of the Makalu Barun National Park of eastern Nepal. *International Journal of Remote Sensing* 23, 1: 125–143.